COMBUSTION MODELING OF SPARK ASSISTED COMPRESSION IGNITION FOR EXPERIMENTAL ANALYSIS AND ENGINE SYSTEM SIMULATIONS

by

Elliott Alexander Ortiz-Soto

A dissertation submitted in partial fulfillment
of the requirements for the degree of
Doctor of Philosophy
(Mechanical Engineering)
in the University of Michigan
2013

Doctoral Committee:

Adjunct Professor Dionissios N. Assanis, Co-Chair
Professor Margaret Wooldridge, Co-Chair
Associate Professor Claus Borgnakke
Assistant Professor Krzysztof Fidkowski
Research Scientist George Lavoie
Assistant Research Scientist Jason Martz
Aristotelis Babajimopoulos, Volvo Group

To my Parents,
Luis Javier and Maritza

ACKNOWLEDGMENTS

These past few years of graduate studies have presented many challenges, but none that was not accompanied by great learning. Luckily, I have always counted with the presence of many people around me: family, friends and faculty. Through their guidance, support and encouragement, they have played a key role in my academic success at the University of Michigan.

My research at U-M would certainly not have been possible without the support of my advisor Prof. Dennis Assanis. He has always been a source of great motivation and expertise in the field of internal combustion engines. I am deeply grateful for the opportunity he has given me to pursue my academic goals in a field I am very passionate about.

The last two years presented a great transition in the lab. I am very grateful to Prof. Margaret Wooldridge for having adopted us as one of her own. She provided great guidance and support in a very important period of my career at the University.

I would like to thank Dr. George Lavoie, who not only challenged me to advance my understanding of internal combustion engine fundamentals, but also provided insightful discussions and served as a genuine mentor.

My research accomplishments as part of the Auto Lab would have proven much more difficult without the assistance of Dr. Aristotelis Babajimopoulos, whose knowledge and constant willingness to help were instrumental.

I would also like to express my gratitude to Dr. Jason Martz, for always providing valuable input.

I would like to thank Prof. Claus Borgnakke and Prof. Krzysztof Fidkowski for becoming part of my doctoral committee. I am grateful in advance for the important contributions they will certainly offer to my research work.

I would like to thank the National GEM Consortium and Dr. Robert Wagner at Oak Ridge National Lab for the financial support I have received over the past few years, which has allowed me to focus on striving for academic and research excellence.

I would like to acknowledge my friends and colleagues at the Auto Lab for generously sharing their time, knowledge and support whenever I needed it.

I would finally like to thank my parents, Luis Javier and Maritza, whom I greatly admire and whom I dedicate this thesis to, for always being there and providing me the confidence I sometimes needed to continue pursuing my goals; they have been a source of inspiration for all my achievements. I am also thankful to my two younger brothers, Bryan and Fernando Andre, for always looking up to and believing in me. And I thank Andrea, whose love and support, especially this past year, I will always treasure very dearly.

TABLE OF CONTENTS

LIST OF FIGURES

LIST OF TABLES

ABSTRACT

Advanced combustion strategies provide significant efficiency and emissions benefits compared to conventional spark ignited (SI) combustion, but challenges related to combustion control and load limits have made these technologies difficult to implement in practical systems. Until now, low cost reduced order models necessary for large parametric and multi-cycle studies capable of accurately capturing the full range of combustion modes from homogeneous charge compression ignition (HCCI) and spark-assisted compression ignition (SACI) to SI have not been available. This important computational gap for advanced combustion engine research was the primary motivation for this doctoral work. The outcomes of this study include powerful new tools to evaluate advanced combustion strategies as well as novel methods to incorporate important advanced combustion characteristics into reduced order models.

A reduced order thermodynamic model of advanced SACI combustion was first proposed. The model was used with available experimental data and previous high fidelity simulation results to develop a new empirical auto-ignition burn rate model that captures the effects of ignition timing, composition, temperature, pressure, engine speed, stratification and flame propagation.

A complete engine model was then developed and incorporated into the commercial simulation software GT-Power. The model included chemical kinetics for low temperature heat release and auto-ignition detection and the empirical burn rate model for post-ignition heat release, as well as a new flame propagation model with improved physical groundings. The calibrated engine model showed good agreement with experimental trends of HCCI, SACI and SI combustion modes.

The engine model was then used to assess practical strategies for accessing the advanced combustion regime and improving engine efficiency. The results showed HCCI and SACI provide a pathway for significant efficiency benefits compared to throttled SI, with efficiency improvements between 15-25% across a range of loads from 1-7 bar BMEP. Further efficiency gains appear possible beyond the experimentally observed SACI limit.

As a further exercise, the load extension potential of boosted SACI combustion was conceptually investigated using a simple thermodynamic framework incorporating the empirical burn rate model and practical operating constraints. The results indicate boosted SACI can nearly double the maximum engine load compared to naturally aspirated operation.

CHAPTER 1

INTRODUCTION

Improving the efficiency and emissions of internal combustion engines, which currently power more than 250 million cars in the US alone, is a key approach for curbing climate change and ensuring energy security in the future. In recent years, significant progress in conventional gasoline spark-ignition (SI) and diesel engines has been made possible in part by the steady improvements in computational capabilities, which have facilitated better engine controls, as well as large-scale, high-fidelity engine simulations. These advances have allowed widespread use of technologies such as variable valve actuation and direct fuel injection. Moreover, improved turbocharger systems have enabled engine downsizing, providing notable fuel economy gains while maintaining and increasing engine torque levels comparable to larger naturally aspirated engines. Biofuels and powertrain electrification (i.e. electric and hybrid-electric vehicles) are also becoming more feasible, offering the potential for optimizing engine operation and diversifying the future energy mix in the transportation sector. Despite these remarkable advances, factors such as increasingly stringent federal standards for emissions and fuel economy, growing global energy demand, and the threat of global warming are already imposing the need for even more dramatic improvements that can only be achieved cost-effectively in the near term by means of advanced engine combustion technologies.

1.1 Spark-Ignition Engines

Spark-ignition (SI) engines currently dominate the U.S. transportation market for passenger vehicles, as well as most international markets, with the exception of Europe where diesel engines maintain a large share. Gasoline spark-ignition engines conventionally employ a premixed fuel and air mixture with a minimal fraction of burned residuals, generally referred to as exhaust gas recirculation (EGR). The mixture is compressed and directly ignited by a spark-discharge before the piston reaches top dead center (TDC). A laminar flame kernel initially develops around the electrode, but as the kernel grows it gets quickly distorted by the highly turbulent field in the combustion chamber. The fully turbulent flame then propagates through the unburned mixture until it extinguishes near the cylinder walls. Experimental observations have shown SI combustion as a continuous laminar reaction front, wrinkled and convoluted by the turbulent flow [1].

The load range and efficiency of spark-ignition engines is typically constrained by emissions regulations and knock. The high burned gas temperatures resulting from combustion lead to the production of large amounts of engine-out nitric oxides (NO_x), even under lean conditions. Therefore, SI engines are operated mostly with a stoichiometric mixture to maintain high efficiency operation of the three-way catalytic converter in the after-treatment system, usually seen as the most cost-effective emissions control solution. This precludes the potential efficiency benefits of lean operation resulting from a higher mixture specific heat ratio. Moreover, fully stoichiometric operation requires some form of airflow throttling to control load, further reducing the overall engine efficiency as a result of pumping losses. Knock, on the other hand, limits the engine compression ratio and directly limits the achievable thermodynamic cycle efficiency. SI knock is generally associated with uncontrolled auto-ignition of the end-gas due to flame front compression and localized hot spots. Higher compression ratios yield higher in-cylinder temperatures at the time of spark, subsequently facilitating auto-ignition in the unburned mixture and increasing the occurrence and intensity of knock.

Despite these constraints, the spark-ignition engine benefits from a wide load and speed operating range, making it a practical option for many transportation applications. Notable improvements in SI engine efficiency and emissions have been recently enabled by technologies such as variable valve actuation (VVA), direct fuel injection (DI), EGR, and turbo-/super-charging.

A number of VVA strategies for lift, duration and timing have been implemented in production vehicles. Some VVA approaches are aimed at optimizing airflow to provide better torque characteristics throughout the speed range. Others are used to enable unthrottled operation for reduced pumping losses and to prevent flow short-circuiting [2]-[6]. Early/late intake valve closing (EIVC/LIVC) has also been used to achieve higher efficiency overexpanded Atkinson or Miller cycles without the need for sophisticated mechanical linkage-based configurations [7], [8].

DI offers more precise control over the fuel injection event and helps minimize the loss of fuel into the exhaust stream. It also presents the opportunity for stratified-charge approaches that allow for globally lean mixtures with the potential for 20-30% fuel economy improvements [9]. It has also been shown that fuel consumption can be further reduced on the order of 10% by using EGR. The reduced flame temperature resulting from increased mixture dilution can suppress knock at the higher loads and allows the engine to operate more efficiently [10]-[12]

Turbo-/super-charging has become increasingly popular in spark-ignition engines due to the potential fuel economy benefits through engine downsizing [13], [14]. For a given power output, a smaller boosted engine typically operates at a higher specific load and efficiency compared with its naturally aspirated counterpart [15]. Overall friction reductions and vehicle weight savings can also be achieved due to lower component masses. Furthermore, the synergies found between turbocharging and other advanced engine technologies, such as VVA, DI [16] and cooled EGR [17], [18], makes it an attractive choice for developing highly efficient engines with ultra-low emissions. Configurations with multiple turbo-/super-chargers, as well as variable geometry turbines, have also been shown to provide better dynamic behavior and further efficiency gains [16].

1.2 Low Temperature Combustion

Low temperature combustion (LTC), where the burned gas temperature is low compared to conventional devices, is one of the most promising concepts in the internal combustion engine field for achieving substantial efficiency improvements and reducing harmful emissions without the need for complex and expensive exhaust after-treatment systems. LTC is most commonly operated in the form of homogeneous-charge compression ignition (HCCI). During HCCI combustion, a premixed or homogeneous fuel-air mixture is compressed to the point of auto-ignition in a process predominantly controlled by chemical kinetics [19]-[22]. Compared to spark-ignition, HCCI combustion is faster, and can be operated with a much leaner mixture, higher compression ratios and un-throttled, considerably boosting thermodynamic efficiency. Homogeneous mixtures and low combustion temperatures also reduce nitrogen oxide (NO_x) and carbonaceous soot emissions, simplifying exhaust gas after-treatment systems compared with modern diesel engines. HCCI combustion has also been shown to work well for a large range of fuels, promising a high degree of flexibility that can be harnessed for using alternative fuels, such as ethanol, natural gas, biofuels and hydrogen.

But practical implementation of HCCI combustion faces important challenges. Contrary to conventional SI and diesel engines, HCCI lacks a direct ignition trigger, making it difficult to optimize combustion and ensure stability over a wide range of conditions. Moreover, due to the kinetics-controlled nature of HCCI, ignition has a strong dependence on the pre-compression temperature and composition, along with the thermal behavior of the engine structure [23], [24].

A number of strategies to achieve HCCI combustion control have been proposed. Intake air heating has often been used in fundamental HCCI studies and demonstrated to provide the desired combustion phasing under steady-state conditions. However, the slow system response time would likely become problematic for transient control of real-world automotive applications. More practical approaches involve the use of unconventional VVA strategies to trap larger amounts of hot internal residuals, substituting the pre-heated air with internal EGR as diluent and controlling the thermal conditions at the start of compression [25]-[31]. The recompression valve strategy makes use of negative valve overlap (NVO) to control the residual gas content [25]-[29]. It has been shown to be a reasonably effective approach for HCCI combustion phasing and has since been widely adopted within the HCCI research community. Introducing cooler external EGR can also further enhance ignition control and enable higher loads [32].

The rapid HCCI combustion event, which is a key contributor to better thermodynamic efficiency, also results in increased pressure-rise rates that can become damaging at high engine loads, and cause a phenomenon similar to engine knock referred to as “ringing”. High dilution levels can be used to retard combustion phasing, but this eventually leads to combustion instabilities and possible misfire. At lower loads, the mixture is too cold and bulk quenching leads to incomplete combustion and, again, possible misfire. Finally, the poor efficiency of three-way catalytic converters under lean conditions requires engine-out NO_x emissions to be below the stipulated tailpipe regulations in order to avoid expensive after-treatment systems. This constraint may be the most flexible, since stoichiometric operation can also be achieved by employing high amounts of residual dilution and external EGR.

Manofsky et al. [33] mapped the usable naturally aspirated HCCI operating range for a single-cylinder experimental engine with fully-flexible valve actuation (FFVA) as a function of net load and combustion phasing at 2000 rpm, as shown in Figure 1.1. Engine load is given the net indicated mean effective pressure ($IMEP_{net}$ or NMEP) metric, which is the integrated cycle work based on the cylinder pressure, normalized by the displaced volume. The standard combustion phasing metric is CA50, which is the time (crank-angle) at 50% burned fraction. The maximum load achieved within the constraints of ringing intensity [34] and stability was approximately 3.7 bar NMEP. Stability was assessed based on the coefficient of variation (COV) of IMEP and ringing intensity is a metric related to maximum pressure and maximum pressure-rise rate.

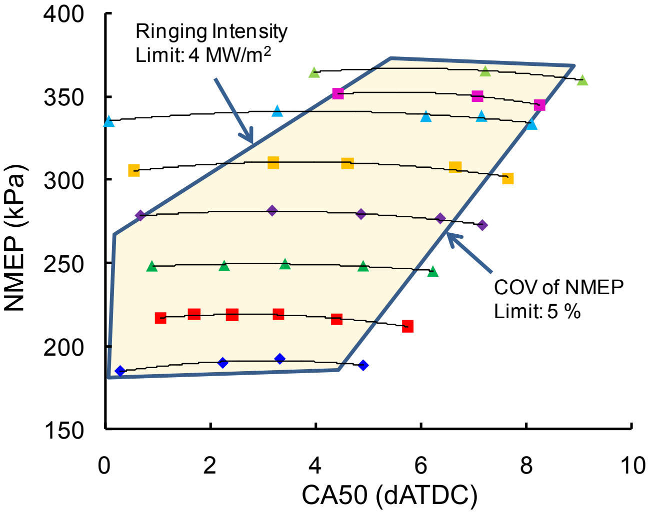

Figure 1.1 – Naturally aspirated HCCI operating range for single-cylinder experimental engine with fully-flexible valve actuation at 2000 rpm [33].

In earlier work by the author, system-level engine cycle simulations employing predictive combustion models [35] were used to compare the HCCI operating regime to the operating regime of conventional SI in Figure 1.2, showing that HCCI results in a significantly narrower speed and load range. The BMEP load metric is the brake torque (at the flywheel) normalized by the displaced volume. The contours in Figure 1.2 are for brake specific fuel consumption (BSFC), a normalized metric for fuel consumption. The BSFC results show up to 25% improvement potential for HCCI over SI operation. Other experimental and model-based SI and HCCI maps in the literature show similar trends [32], [36], [37]. Despite this limitation, HCCI combustion can still cover a significant portion of the high frequency operating points in Federal Test Procedure (FTP) drive-cycles for light-duty passenger cars [38]. Drive-cycle simulation studies have quantified the potential fuel economy improvements in the range of 10% to 20% [32], [35], [37]. Even so, the full power demand of a vehicle under realistic driving conditions is still beyond the capability of naturally aspirated HCCI operation. Hence, a significant research effort is dedicated to expanding the HCCI load range to the spark-ignited range.

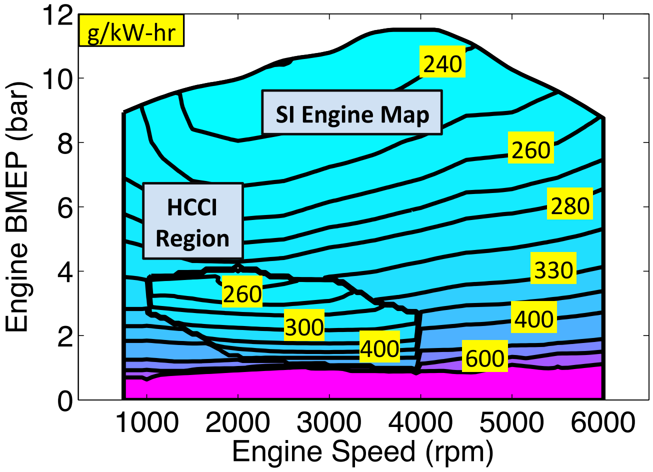

Figure 1.2 – Dual mode SI-HCCI engine fuel consumption map based on engine cycle simulations with predictive combustion models [35].

The widespread use of turbo-/super-charging technologies in SI engines has made them an attractive option for HCCI load expansion. Boosting the intake pressure can compensate for losses associated with the high dilution levels necessary for HCCI combustion. Christensen et al. [39] were able to increase the maximum net IMEP from 5 bar at naturally aspirated conditions to 14 bar with 300 kPa absolute of supercharging on a single-cylinder test engine using fuels such as iso-octane, ethanol and natural gas. Olsson et al. [40] achieved 16 bar BMEP at equivalence ratios on the order of 0.5 and 300 kPa absolute intake pressure with a multi-cylinder, turbocharged HCCI engine using n-heptane and ethanol mixtures. At high loads, the brake thermal efficiency of the HCCI engine ranged between 35% and 40% compared to 45% for the diesel. Dec and Yang [41] reported loads of 16 bar gross IMEP at boosted HCCI conditions up to 325 kPa absolute with conventional gasoline using intake air heating and cooled EGR. They showed that much later combustion phasing was possible at high pressures, allowing them reduce pressure-rise rates while still maintaining good operational stability.

On the other hand, the reduced exhaust enthalpies resulting from low temperature combustion limits the available turbine shaft work used to compress the intake air with a turbocharger setup. Engine-driven superchargers do not suffer from this drawback, but they require a significant amount of output work from the engine. To address some of these issues, more complex configurations combining superchargers or multiple turbochargers with variable geometry have recently been investigated and shown to enable further HCCI load extension [42].

Despite all the recent progress on HCCI combustion, dual-mode SI-HCCI engines still present the most practical near-term solution to the commercial implementation of HCCI. These engines operate within two discrete regions, SI or HCCI. Engine cycle simulation studies of dual-mode SI-HCCI engines showed a large number of potential transitions, some of which would likely not be achievable in a real engine [35]. Experimental investigations have demonstrated some of the requirements for successful SI-HCCI transitions using the NVO valve strategy [43], [44]. It has been observed that it takes on the order of 10 cycles for the engine to settle into steady HCCI operation. Figure

1.3 shows a typical transition from SI to HCCI. From the pressure traces it can be seen that the first two cycles knock before HCCI combustion stabilizes. The non-optimal operation during the finite transition process in both combustion modes could result in diminished fuel economy gains if the transitions are not managed properly.

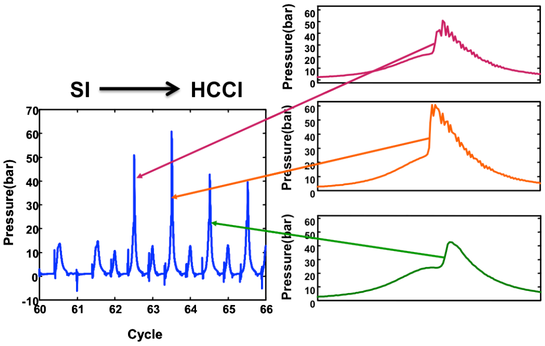

Figure 1.3 − Knocking SI-HCCI transition illustrating the finite mode transition process before HCCI combustion settles into steady operation [43].

1.3 Advanced Combustion: Spark-Assisted Compression Ignition

As a result of the upper load limit (typically determined by the ringing constraint), there exists a large efficiency gap between the ultra-dilute, unthrottled operation achievable with HCCI combustion, and stoichiometric, part-throttle SI operation. This region is commonly referred to as the ‘advanced combustion’ regime. Lavoie et al. [45] explored the fundamental thermodynamics of operating in these regimes to identify the potential engine efficiency benefits of advanced combustion, conceptually shown in Figure 1.4(a) for naturally aspirated conditions. These results reveal an optimum efficiency path throughout the full load range employing advanced combustion using air and EGR diluted strategies. Using a drive-cycle simulation, it was further demonstrated that sizable vehicle fuel economy gains could be achieved if advanced combustion modes were effectively utilized; up to 23% for naturally aspirated operation and 58% for a downsizing/boosting strategy. These operating modes could bring the goal of ultraefficient and clean internal combustion engines closer to reality. Consequently, a great deal of research has been dedicated to developing advanced combustion technologies.

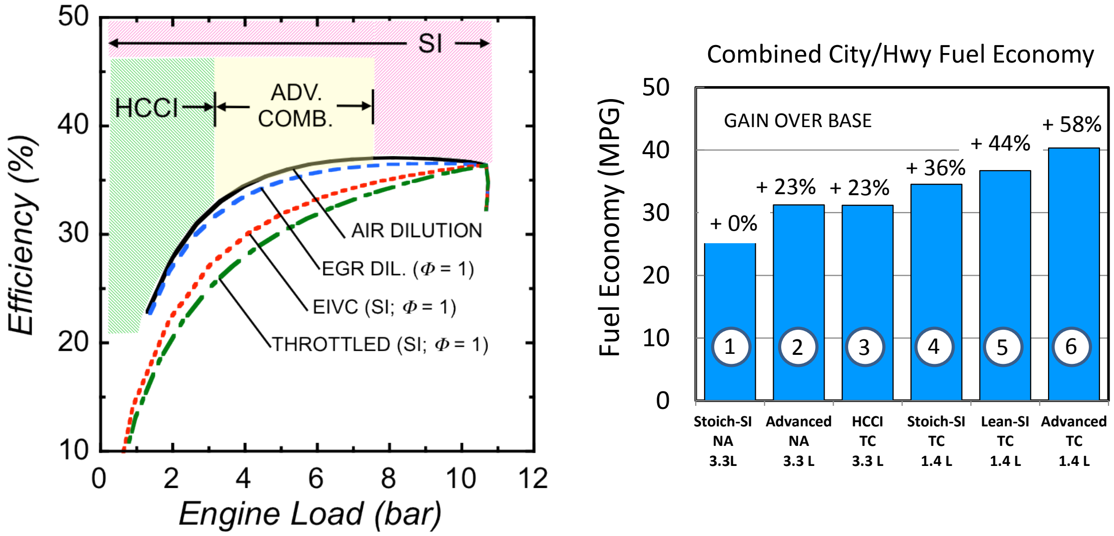

(a) (b)

Figure 1.4 – (a) Potential for brake efficiency gains for naturally aspirated engines, depending on combustion regime: HCCI, advanced combustion, and spark ignition. (b) Combined city/highway fuel economy of advanced combustion strategies (2-6) and percent gain over the baseline SI engine (1). [45]

Spark-assisted compression ignition (SACI or SA-HCCI) is a hybrid advanced combustion mode currently under investigation, which uses spark-ignition and flame propagation to directly initiate or stimulate auto-ignition and HCCI-like combustion [46]-[48]. This allows for combustion under conditions not possible when exclusively using SI or HCCI, particularly with respect to charge temperature and dilution [49]. It can be used for combustion phasing control [50] and has the potential for load expansion relative to HCCI operation by reducing peak heat release rates [33], [51], [52]. SACI has also been shown to improve the cyclic variability of combustion depending on the conditions [53].

Lavoie et al. [54] illustrated the SACI concept using a multi-mode combustion diagram, as shown in Figure 1.5. The SI, HCCI and SACI combustion regimes were defined based on theoretical knock, NO_x, flammability and combustion stability constraints given as a function of burned and unburned temperatures and dilution level. The diagram shows a large region for potential spark-assisted operation, where the efficiency benefits of advanced combustion could be realized in practice.

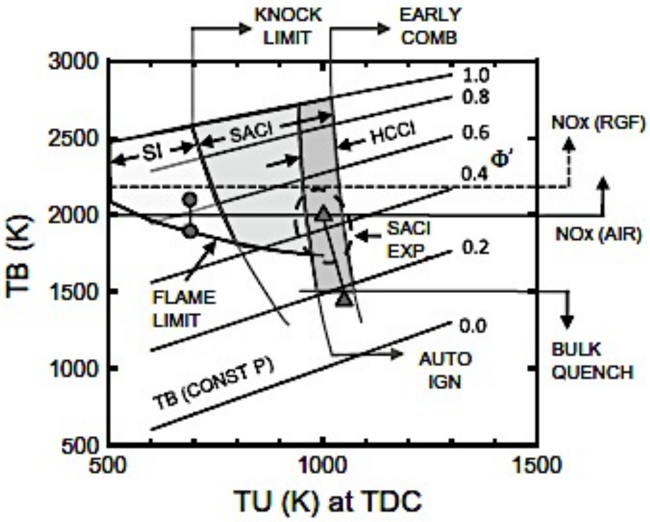

Figure 1.5 − Multi-mode combustion diagram showing the theoretical SI, SACI and HCCI regimes constrained by knock, NO_x and combustion stability [54].

The key to load expansion with SACI combustion is the slower heat release during the initial flame propagation phase. Figure 1.6 shows the measured cylinder pressure and estimated apparent heat release rate (AHRR) as load is increased for a fixed CA50 around 8-10 degrees after top dead center (ATDC). In HCCI engines, the load can be increased by higher fueling rates at a given pre-combustion temperature and dilution level. However, the faster pressure-rise rates constrain the viable range that can be reached. With SACI, the pre-combustion temperature can be reduced by substituting hot internal EGR by cooler external EGR, and then compensating using spark advance [50]. This combination provides a means to phase combustion and adjust the overall heat release profile, allowing higher loads not possible with HCCI.

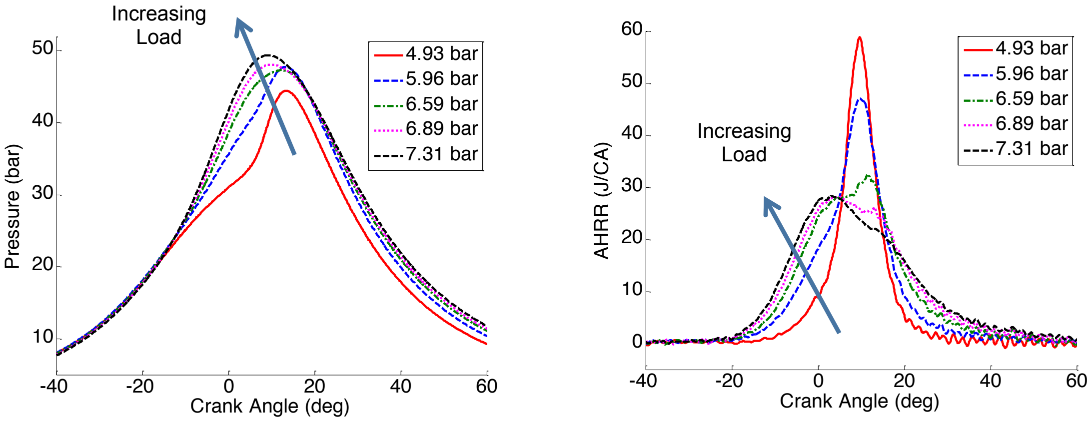

(a) (b)

Figure 1.6 – (a) Cylinder pressure and (b) rate of heat release for increasing engine load (IMEP) under SACI conditions [33].

Researchers at the University of Michigan (U-M) [33] and Oak Ridge National Laboratory (ORNL) [51] mapped the SACI load range relative to HCCI and SI in two research engines. In Figure 1.7(a), the regions of HCCI and SACI are plotted against load and combustion timing for the experiments conducted at U-M. Figure 1.7(b) shows the loads achieved using various combustion modes as a function of engine speed in the ORNL engine. Both experiments employed a combination of NVO, external EGR and spark timing to achieve optimal combustion while maintaining a stoichiometric equivalence ratio at SACI conditions. Results consistently show maximum loads around 7.5 bar NMEP in the SACI regime, a considerable increase from the typical HCCI load limit of approximately 4 bar under naturally aspirated conditions.

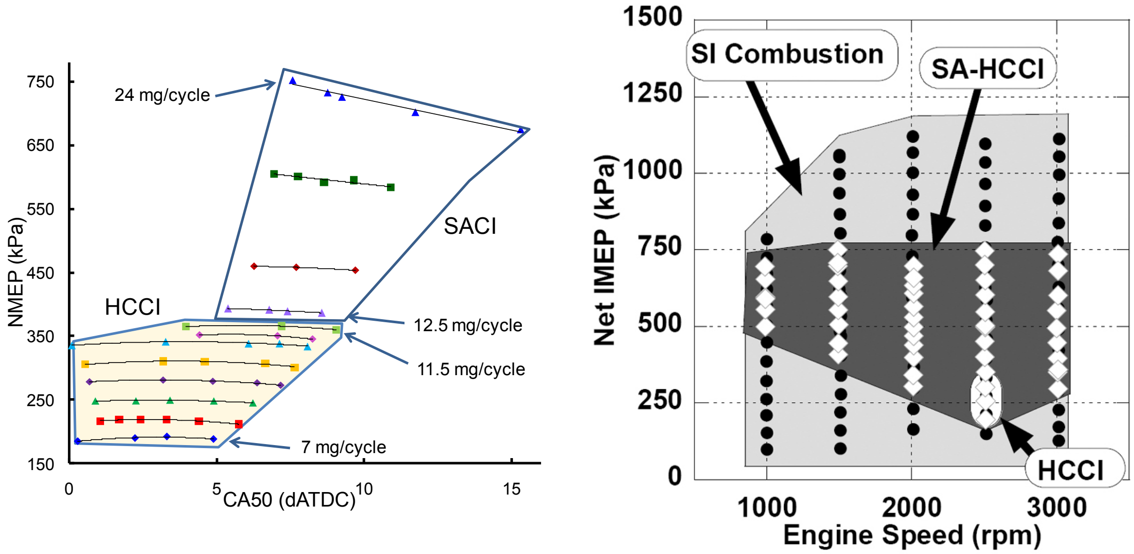

(a) (b)

Figure 1.7 – (a) Extended SACI operating range for single-cylinder experimental engine with fully-flexible valve actuation at 2000 rpm [33]. (b) Multi-mode combustion load and speed range under stoichiometric conditions employing spark-ignition, NVO and external EGR [51].

SACI also offers the potential for smooth or gradual combustion mode transitions during transient engine operation [55]. Even though spark-assist introduces an additional complexity to engine calibration, the hybrid nature of SACI could possibly eliminate discrete changes in valve actuation and dilution as engine operating points shift from flame propagation to pure auto-ignition. This will most likely result in more robust operation, improved transient behavior, simplified controls and better fuel economy.

1.4 Research Motivation, Objectives and Approach

HCCI combustion engines have been shown to provide significant benefits in efficiency and emissions over conventional stoichiometric spark-ignited engines. However, the constrained operating range and control challenges have generated interest in a multi-mode combustion approach, namely spark-assisted compression ignition. Even though experimental studies have confirmed the viability of SACI and have suggested potential operating strategies, the breadth and depth of these has been limited, leaving unanswered some major questions related to combustion mode stability and tradeoffs, engine operating limits and control strategies for optimum efficiency. Particularly, boosted SACI operation has yet to be demonstrated experimentally.

Multi-mode SACI combustion models have been developed within high-fidelity three-dimensional computational fluid dynamics (CFD) frameworks to address some of these questions [56]-[58]. These simulations can provide detailed predictions of the effects of in-cylinder turbulence and thermal/compositional gradients, known to be important for flame propagation and auto-ignition. However, the high fidelity CFD simulations are generally too computationally expensive for use in large parametric studies and are currently confined to studies aimed at fundamental understanding. At the level of a complete engine system, zero-dimensional (0-D) or quasi-dimensional (Q-D) phenomenological models are typically employed. These provide a platform for parametric simulations at a much larger scale, and, when properly developed and calibrated, can predict the important trends at a substantially reduced computational cost, on the order of 3000 to 6000 times faster per engine cycle. Currently, no 0-D or Q-D model for SACI combustion is available in the literature, and although independent flame propagation and HCCI models do exist, they have not been integrated to correctly simulate SACI combustion.

The main goal of this doctoral work is to develop a complete phenomenological and computationally inexpensive model of advanced SACI combustion that captures the most important physical behavior of flame propagation and auto-ignition under high pressures, temperatures and dilution levels. The new SACI combustion model will be used in engine system simulations of HCCI, SACI and SI combustion modes to explore the load extension and efficiency improvement potential of advanced combustion strategies considering practical operating constraints. The model will also provide a platform for studying cycle-to-cycle instabilities, cylinder-to-cylinder interactions, control strategies and vehicle fuel economy. The modeling tools developed in this work and subsequent model-based studies will address the current gap in computational capability for studying advanced combustion and will bring us closer to answering the question: Is the advanced multi-mode SACI combustion concept a viable and practical approach for achieving significant improvements in efficiency and emissions of internal combustion engines?

The research approach and general modeling framework is summarized visually in Figure 1.8. Specifically, this work will:

- Develop a reduced-order thermodynamic model of advanced SACI combustion that provides the basis for the representation of SACI combustion processes for use in experimental analysis and system-level engine simulations. (CHAPTER 2)
- Develop a comprehensive heat release analysis framework that addresses the special demands of experimental advanced combustion research, which includes unconventional valve strategies, elevated dilution levels, and multi-mode combustion regimes, together with extended capabilities for advanced combustion engine experiments based on the reduced order thermodynamic model to provide estimates of auto-ignition timing, flame vs. auto-ignition heat release fractions, auto-ignition heat release rate, and end-gas/post-flame states. The data analysis tool will be used to retrieve key combustion parameters from experimental results for the development and validation of SACI engine models. (CHAPTER 3)
- Develop a new semi-empirical auto-ignition burn rate model for engine system simulations and parametric studies of multi-mode combustion that captures effects of ignition timing, composition, boosting, chemistry, engine speed, EGR-based mixture stratification and SACI flame propagation. (CHAPTER 4)

- Integrate new turbulent flame propagation, auto-ignition and heat transfer models into a predictive engine simulation for multi-mode SACI combustion within a commercial system-level modeling framework with one-dimensional gas dynamics, and calibrate the complete engine model using experimental data for HCCI, SACI and SI combustion modes. (CHAPTER 5)
- Quantify the load extension and efficiency improvement potential of SACI combustion with respect to HCCI and throttled SI engines, and understand operating limits in relation to theoretical potential of advanced combustion. (CHAPTER 6)
- Conceptually explore the potential for boosted SACI operation using a simple thermodynamic modeling framework incorporating auto-ignition burn rate model and representative engine constraints. (CHAPTER 7)

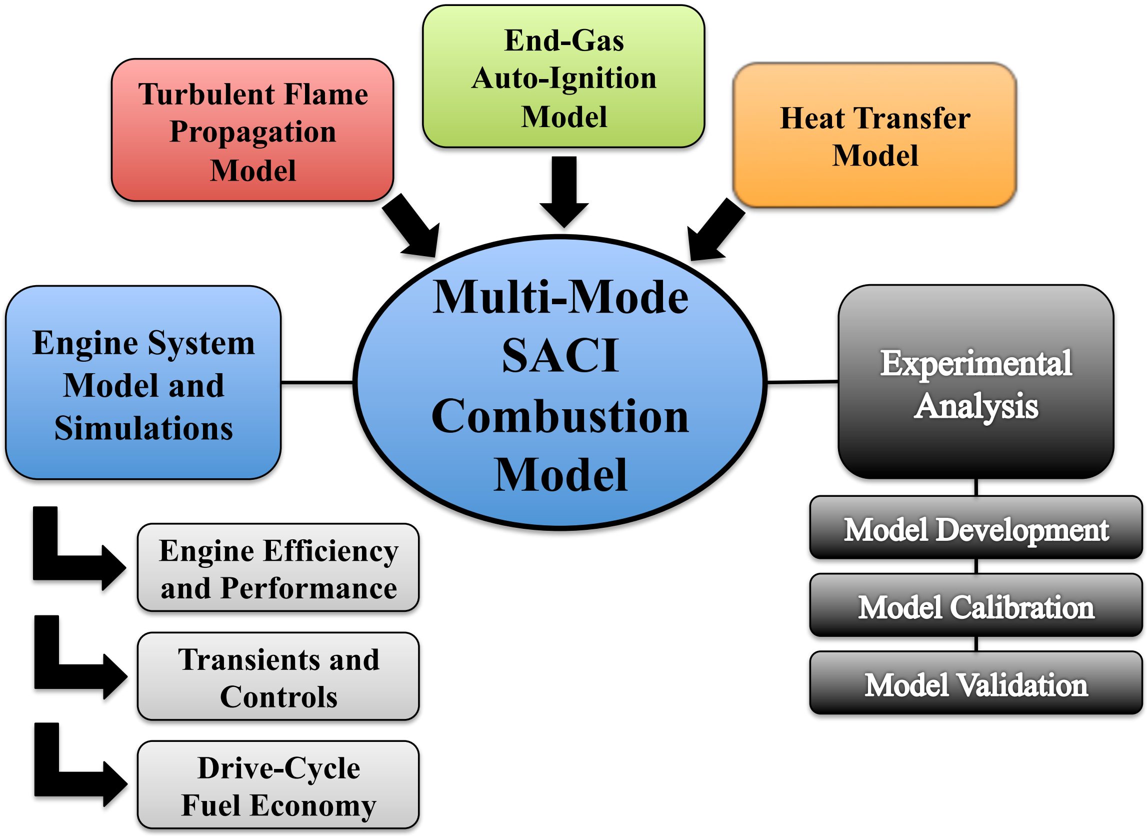

Figure 1.8 – General research framework for experimental analysis, model development and simulation of advanced SACI combustion engines.

1.5 References

[1] J. B. Heywood, *Internal Combustion Engine Fundamentals*. McGraw-Hill, Inc., 1988.

[2] T. W. Asmus, “Valve Events and Engine Operation,” *SAE 820749*, p. 820749, 1982.

[3] S. Nishimura, T. Fukuhara, and M. Teramoto, “Nissan V6 3.0 Litre, 4-cam 24-valve High Performance Engine,” *SAE Transactions*, vol. 96, no. 4, pp. 303–316, 1987.

[4] T. G. Leone, E. J. Christenson, and R. A. Stein, “Comparison of Variable Camshaft Timing Strategies at Part Load,” *SAE 960584*, 1984.

[5] R. Flierl and M. Kluting, “The Third Generation of Valvetrains - New Fully Variable Valvetrains for Throttle-Free Load Control,” *SAE 2000-01-1227*, 2000.

[6] D. Cleary and G. Silvas, “Unthrottled Engine Operation with Variable Intake Valve Lift, Duration, and Timing,” *SAE 2007-01-1282*, 2007.

[7] J. Tuttle, “Controlling Engine Load by Means of Early Intake-Valve Closing,” *SAE 820408*, 1982.

[8] J. Tuttle, “Controlling Engine Load by Means of Late-Intake Valve Closing,” *SAE 800794*, 1980.

[9] J. Harada, T. Tomita, H. Mizuno, Z. Mashiki, and Y. Ito, “Development of Direct Injection Gasoline Engine,” *SAE 970540*, 1997.

[10] E. Watanabe and I. Fukutani, “Knock Reduction of Spark-Ignition Engines by EGR,” *SAE 860034*, 1986.

[11] C. De Petris, S. Diana, V. Giglio, and G. Police, “High Efficiency Stoichiometric Spark Ignition Engines,” *SAE 941933*, 1994.

[12] T. Alger, J. Gingrich, R. H. Perry, and B. Mangold, “Cooled EGR for Fuel Economy and Emissions Improvement in Gasoline Engines,” *JSAE 20105013*, 2010.

[13] H. Hiereth and G. Withalm, “Some Special Features of the Turbocharged Gasoline Engine,” *SAE 790207*, 1979.

[14] T. Noyori, T. Ohira, T. Nakamura, and Y. Akamatsu, “Development of a 660cc Turbo-Charge Spark-Ignition Direct-Injection Engine,” *SAE 2003-32-0013*, 2003.

[15] P. Watts and J. B. Heywood, “Simulation Studies of the Effect of Turbocharging and Reduced Heat Transfer on Spark-Ignition Engine Operation,” *SAE 800289*, 1980.

[16] W. Bandel, G. K. Fraidl, P. E. Kapus, H. Sikinger, and C. N. Cowland, “The Turbocharged GDI Engine: Boosted Synergies for High Fuel Economy Plus Ultra-low Emission,” *SAE 2006-01-1266*, 2006.

[17] T. Alger, J. Gingrich, B. Mangold, and R. H. Perry, “A Continuous Discharge Ignition System for EGR Limit Extension in SI Engines,” *SAE 2001-01-0661*, 2011.

[18] T. Alger, B. Mangold, R. H. Perry, and J. Gingrich, “The Interaction of Fuel Anti-Knock Index and Cooled EGR on Engine Performance and Efficiency,” *SAE 2012-01-1149*, 2012.

[19] S. Onishi, S. H. Jo, K. Shoda, P. Do Jo, and S. Kato, "Active Thermo-Atmosphere Combustion (ATAC) - A New Combustion Process for Internal Combustion Engines," *SAE 790501*, 1979.

[20] P. M. Najt and D. E. Foster, "Compression-Ignited Homogeneous Charge Combustion," *SAE 830264*, 1983.

[21] J. Willand, R.-G. Nieberding, G. Vent, and C. Enderle, "The Knocking Syndrome - Its Cure and Its Potential," *SAE 982483*, 1998.

[22] R. H. Thring, "Homogeneous-Charge Compression-Ignition (HCCI) Engines," *SAE 892068*, 1989.

[23] K. Chang, A. Babajimopoulos, G. A. Lavoie, Z. S. Filipi, and D. N. Assanis, "Analysis of Load and Speed Transitions in an HCCI Engine Using 1-D Cycle Simulation and Thermal Networks," *SAE 2006-01-1087*, 2006.

[24] K. Chang, G. A. Lavoie, A. Babajimopoulos, Z. S. Filipi, and D. N. Assanis, "Control of a Multi-Cylinder HCCI Engine During Transient Operation by Modulating Residual Gas Fraction to Compensate for Wall Temperature Effects," *SAE 2007-01-0204*, 2007.

[25] H. Zhao, J. Li, T. Ma, and N. Ladommatos, "Performance and Analysis of a 4-Stroke Multi-Cylinder Gasoline Engine with CAI Combustion," *SAE 2002-01-0420*, 2002.

[26] H. Persson, M. Agrell, J.-O. Olsson, B. Johansson, and H. Ström, "The Effect of Intake Temperature on HCCI Operation Using Negative Valve Overlap," *SAE 2004-01-0944*, 2004.

[27] D. Law, D. Kemp, J. Allen, G. Kirkpatrick, and T. Copland, "Controlled Combustion in an IC-Engine with a Fully Variable Valve Train," *SAE 2001-01-0251*, 2001.

[28] P. Wolters, W. Salber, J. Geiger, M. Duesmann, and J. Dilthey, "Controlled Auto Ignition Combustion Process with an Electromechanical Valve Train," *SAE 2003-01-0032*, 2003.

[29] T.-W. Kuo, "Valve and Fueling Strategy for Operating a Controlled Auto-Ignition Combustion Engine," presented at the SAE 2006 HCCI Symposium, September 25-26, 2006, San Ramon, CA, 2006.

[30] P. A. Caton, H. H. Song, N. B. Kaahaaina, and C. F. Edwards, "Strategies for Achieving Residual-Effected Homogeneous Charge Compression Ignition Using Variable Valve Actuation," *SAE 2005-01-0165*, 2005.

[31] N. Milovanovic, J. Turner, S. Kenchington, G. Pitcher, and D. Blundell, "Active valvetrain for homogeneous charge compression ignition," *International Journal of Engine Research*, vol. 6, no. 4, pp. 377–397, 2005.

[32] A. Cairns and H. Blaxill, "The Effects of Combined Internal and External Exhaust Gas Recirculation on Gasoline Controlled Auto-Ignition," *SAE 2005-01-0133*, 2005.

[33] L. Manofsky, J. Vavra, D. Assanis, and A. Babajimopoulos, "Bridging the Gap between HCCI and SI: Spark-Assisted Compression Ignition," *SAE 2011-01-1179*, 2011.

[34] J. A. Eng, "Characterization of Pressure Waves in HCCI Combustion," *SAE 2002-01-2859*, 2002.

[35] E. Ortiz-Soto, D. Assanis, and A. Babajimopoulos, “A comprehensive engine to drive-cycle modelling framework for the fuel economy assessment of advanced engine and combustion technologies,” *International Journal of Engine Research*, vol. 13, no. 3, pp. 287–304, 2012.

[36] T. Tsuchiya, H. Hosoi, K. Hoshi, H. Shimamura, T. Hagiwara, Y. Ito, and F. Arai, “Newly Developed Inline 4 AR Series SI Engine,” *SAE 2009-01-1048*, 2009.

[37] A. Kulzer, D. Lejsek, and T. Nier, “A Thermodynamic Study on Boosted HCCI: Motivation, Analysis and Potential,” *SAE 2010-01-1082*, 2010.

[38] *U.S. Environmental Protection Agency, Dynamometer Driving Schedules*. [Online]. Available: http://www.epa.gov/nvfel/testing/dynamometer.htm. [Accessed: 21-Jul-2013].

[39] M. Christensen, B. Johansson, P. Amneus, and F. Mauss, “Supercharged Homogeneous Charge Compression Ignition,” *SAE 980787*, 1998.

[40] J.-O. Olsson, P. Tunestal, G. Haraldsson, and B. Johansson, “A Turbo Charged Dual Fuel HCCI Engine,” *SAE 2001-01-1896*, 2001.

[41] J. E. Dec and Y. Yang, “Boosted HCCI for High Power without Engine Knock and with Ultra-Low NOx Emissions - using Conventional Gasoline,” *SAE 2010-01-1086*, 2010.

[42] P. Shingne, D. Assanis, A. Babajimopoulos, A. Mond, and H. Yilmaz, “Application of a Supercharger in a Two-Stage Boosting System for a Gasoline HCCI Engine: A Simulation Study,” presented at the ASME 2011 Internal Combustion Engine Division Fall Technical Conference, ICEF2011-60220, 2011.

[43] H. Santoso, J. Matthews, and W. K. Cheng, “Managing SI/HCCI Dual-Mode Engine Operation,” *SAE 2005-01-0162*, 2005.

[44] N. Milovanovic, D. Blundell, S. Gedge, and J. Turner, “SI-HCCI-SI Mode Transition at Different Engine Operating Conditions,” *SAE 2005-01-0156*, 2005.

[45] G. Lavoie, E. Ortiz-Soto, A. Babajimopoulos, J. B. Martz, and D. N. Assanis, “Thermodynamic sweet spot for high-efficiency, dilute, boosted gasoline engines,” *International Journal of Engine Research*, 2012.

[46] M. Weinrotter, E. Wintner, K. Iskra, T. Neger, J. Olofsson, H. Seyfried, M. Aldén, M. Lackner, F. Winter, A. Vressner, A. Hultqvist, and B. Johansson, “Optical Diagnostics of Laser-Induced and Spark Plug-Assisted HCCI Combustion,” *SAE 2005-01-0129*, 2005.

[47] H. Persson, A. Hultqvist, and B. Johansson, “Investigation of the Early Flame Development in Spark Assisted HCCI Combustion Using High Speed Chemiluminescence Imaging,” *SAE 2007-01-0212*, 2007.

[48] B. T. Zigler, S. M. Walton, D. M. Karwat, D. Assanis, M. S. Woolridge, and S. T. Woolridge, “A Multi-Axis Imaging Study of Spark-Assisted Homogeneous Charge Compression Ignition Phenomena in a Single-Cylinder Research Engine,” *ASME Internal Combustion Engine Division 2007 Fall Technical Conference, ICEF2007-1701*, 2007.

[49] R. M. Wagner, K. D. Edwards, C. S. Daw, J. B. Green, and B. G. Bunting, “On the Nature of Cyclic Dispersion in Spark Assisted HCCI Combustion,” *SAE*

2006-01-0418, 2006.

[50] L. M. Olesky, J. B. Martz, G. A. Lavoie, J. Vavra, D. N. Assanis, and A. Babajimopoulos, "The effects of spark timing, unburned gas temperature, and negative valve overlap on the rates of stoichiometric spark assisted compression ignition combustion," *Applied Energy*, vol. 105, pp. 407–417, 2013.

[51] J. P. Szybist, E. Nafziger, and A. Weall, "Load Expansion of Stoichiometric HCCI Using Spark Assist and Hydraulic Valve Actuation," *SAE 2010-01-2172*, 2010.

[52] T. Urushihara, K. Yamaguchi, K. Yoshizawa, and T. Itoh, "A Study of a Gasoline-fueled Compression Ignition Engine ~ Expansion of HCCI Operation Range Using SI Combustion as a Trigger of Compression Ignition ~," *SAE 2005-01-0180*, 2005.

[53] Z. Wang, J.-X. Wang, S.-J. Shuai, G.-H. Tian, X. An, and Q.-J. Ma, "Study of the Effect of Spark Ignition on Gasoline HCCI Combustion," *Proceedings of the Institution of Mechanical Engineers, Part D: Journal of Automobile Engineering*, vol. 220, no. 6, pp. 817–825, 2006.

[54] G. A. Lavoie, J. Martz, M. Wooldridge, and D. Assanis, "A multi-mode combustion diagram for spark assisted compression ignition," *Combustion and Flame*, vol. 157, no. 6, pp. 1106–1110, 2010.

[55] J. Hyvonen, G. Haraldsson, and B. Johansson, "Operating Conditions Using Spark Assisted HCCI Combustion During Combustion Mode Transfer to SI in a Multi-Cylinder VCR-HCCI Engine," *SAE 2005-01-0109*, 2005.

[56] J. B. Martz, "SIMULATION AND MODEL DEVELOPMENT FOR AUTO-IGNITION AND REACTION FRONT PROPAGATION IN LOW-TEMPERATURE HIGH-PRESSURE LEAN-BURN ENGINES," Ph. D. Thesis, University of Michigan, 2010.

[57] R. Dahms, C. Felsch, O. Röhl, and N. Peters, "Detailed chemistry flamelet modeling of mixed-mode combustion in spark-assisted HCCI engines," *Proceedings of the Combustion Institute*, 2010.

[58] X. Wang, H. Xie, L. Xie, L. Zhang, L. Li, T. Chen, and H. Zhao, "Numerical simulation and validation of SI-CAI hybrid combustion in a CAI/HCCI gasoline engine," *Combustion Theory and Modelling*, vol. 17, no. 1, pp. 142–166, 2013.

CHAPTER 2

REDUCED ORDER THERMODYNAMIC MODEL FOR SACI COMBUSTION ENGINES

2.1 Advanced SACI Combustion Engine Modeling: Review

Combustion is a highly complex problem, merging thermodynamics, turbulent flow and chemistry. The transient nature and geometrical characteristics of reciprocating engines complicate the matter, and the recent interest in advanced combustion concepts has taken researchers into regimes never before contemplated. Increasing computational capabilities have made engine simulations powerful means to gain further insights, particularly when experimental capabilities are limited in scope or resources. High fidelity numerical models solving the Navier-Stokes equations in three dimensions have been used to investigate fundamental combustion problems, evaluate new combustion modes and design detailed combustion systems. Because the focus of this investigation is on engine efficiency and operating limits related to advanced combustion modes, large parametric studies are indispensable. Unfortunately, even relatively low-resolution three-dimensional models can result in prohibitive computational costs. Thus, we have turned to reduced order phenomenological models that can be applied to system-level and multi-cycle engine simulations, as well as experimental data analysis. This chapter briefly reviews existing state of the art models for advanced combustion engine simulation, followed by important zero- and quasi-dimensional models for SI and HCCI engines.

Finally, a reduced order thermodynamic model for multi-mode SACI combustion is presented, which is the core of the work presented in this thesis.

2.1.1 State of the Art Multi-Dimensional Models for SACI Combustion

Direct Numerical Simulation (DNS) provides the highest accuracy of any computational approach by resolving the full range of spatial and temporal turbulent scales directly from the Navier-Stokes equations [1]. However, due to its extreme computational cost, DNS has only been used as a fundamental turbulence and combustion research tool. Large-Eddy Simulation (LES) employs low-pass filtering of the Navier-Stokes equations to resolve the larger turbulent scales, but requires modeling of the smallest scales, which are also typically where combustion takes place [2]. Progresses in LES modeling has made it possible to obtain accurate solutions of problems involving complex geometries and significant turbulent flow/combustion interactions. Although much more practical for engineering applications than DNS, LES is still computationally expensive and cannot be used for routine combustion analysis and design. The most common approach for turbulence and combustion simulations uses the Reynolds-Averaged Navier-Stokes (RANS) equations, where the instantaneous quantities in the original formulation are decomposed into time-averaged and fluctuating quantities [3]. The RANS approach cannot solve the turbulent scales directly, so sub-grid models for turbulent viscous stresses and combustion are necessary.

Several RANS-based models have been developed for SACI combustion simulation. The KIVA-CFMZ model [4] assumes the flame propagation phase of combustion occurs locally within the flamelet regime, which means the reaction front is continuous and propagates at the laminar flame speed. Each computational cell is sub-divided into two regions, reactants and flame products. The reactants are subject to chemical kinetics for auto-ignition by way of a multi-zone mapping technique [5]. A series of sample results for SACI combustion based on the KIVA-CFMZ framework is shown in Figure 2.1. These results demonstrate the utility of these high fidelity simulations, which can not only provide representative predictions of multi-mode combustion heat release rates (Figure 2.1(a)), but can also be used to visualize the combustion event (Figure 2.1(b)) and to determine the effects of operating conditions and combustion strategy on in-cylinder mass distributions (Figure 2.1(c)). Other multi-mode combustion models for high fidelity simulation frameworks are also available. The model by Dahms et al. [6] is conceptually similar, but uses a different flame front tracking scheme and laminar flame structure calculations. On the other hand, the ECFM3Z model [7] utilizes a flame propagation model related to the one in KIVA-CFMZ; however, chemistry is handled using a tabulated approach. In general, these models have shown the capability for replicating experimental SACI results, implying that on a local scale a two-zone assumption with a thin flame interface and a reacting end-gas is sufficient to describe the most important SACI combustion phenomena.

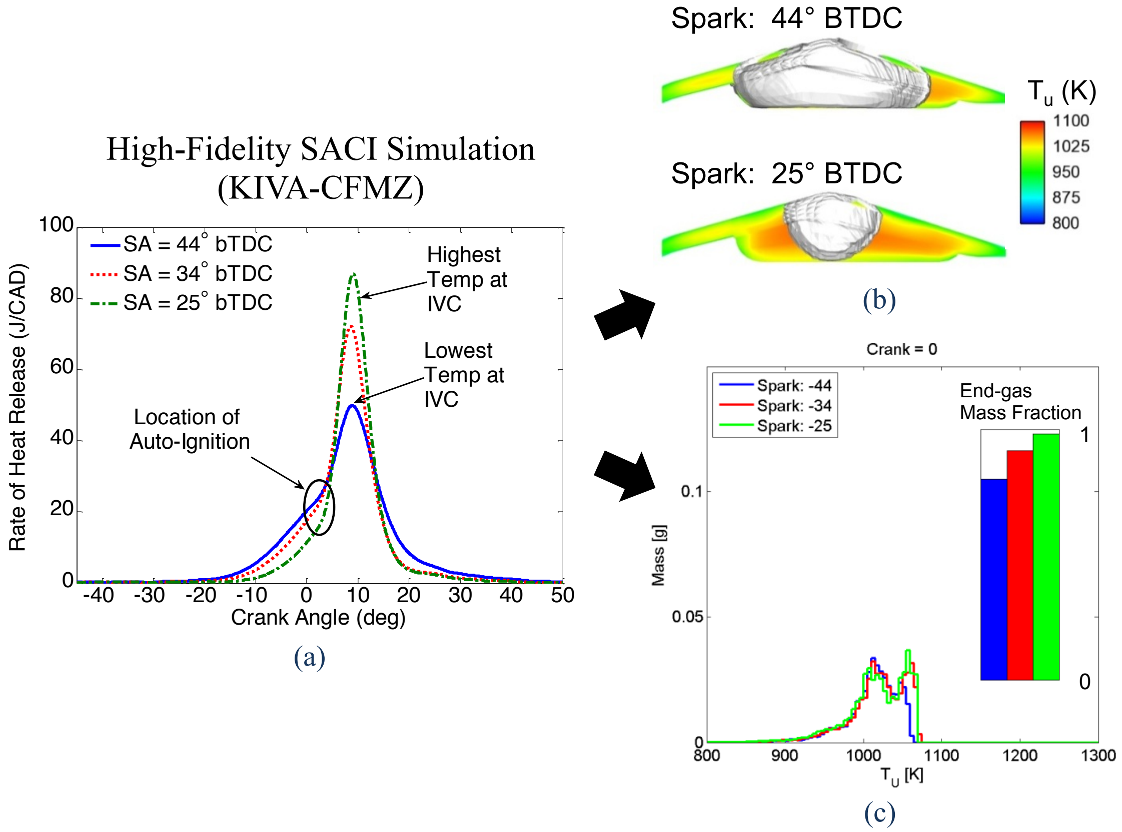

(a)

(b)

(c)

Figure 2.1 – (a) KIVA-CFMZ high fidelity SACI simulation results for a spark timing sweep at 2000 rev/min, Φ = 1.0, EGR ~ 41% and ~ 6.5 bar IMEP_{net}. (b) KIVA predictions of end-gas temperature (T_u) predictions at TDC, just prior to onset of auto-ignition. (c) KIVA end-gas temperature (T_u) distribution at TDC.

2.1.2 Zero-/Quasi-Dimensional Models for SI and HCCI Combustion

Reduced order zero- and quasi-dimensional thermodynamic models have great utility for experimental analysis and system-level engine simulations. When the global nature of the combustion event is of interest, the engine can be modeled as a single reacting zone, subject to piston movement and wall heat losses. This type of approach is generally used for extracting combustion characteristics from measured in-cylinder pressure time histories [8]-[10].

For spark-ignited engine simulations, multiple zones were quickly adopted in light of the significant temperature and compositional differences observed between the pre-flame end-gas and post-flame products during flame propagation [11], [12]. Similar models were also adopted by some authors to enhance their experimental analysis methodology [13], [14]. The typical global two-zone model divides the combustion chamber into an unburned end-gas zone consisting of fresh charge and residuals, and a post-flame burned zone in which only combustion products are present. As shown in Figure 2.2, the zones are separated by a negligibly thin flame front, which propagates into the end-gas mixture, and contains all the reaction layers within the flame.

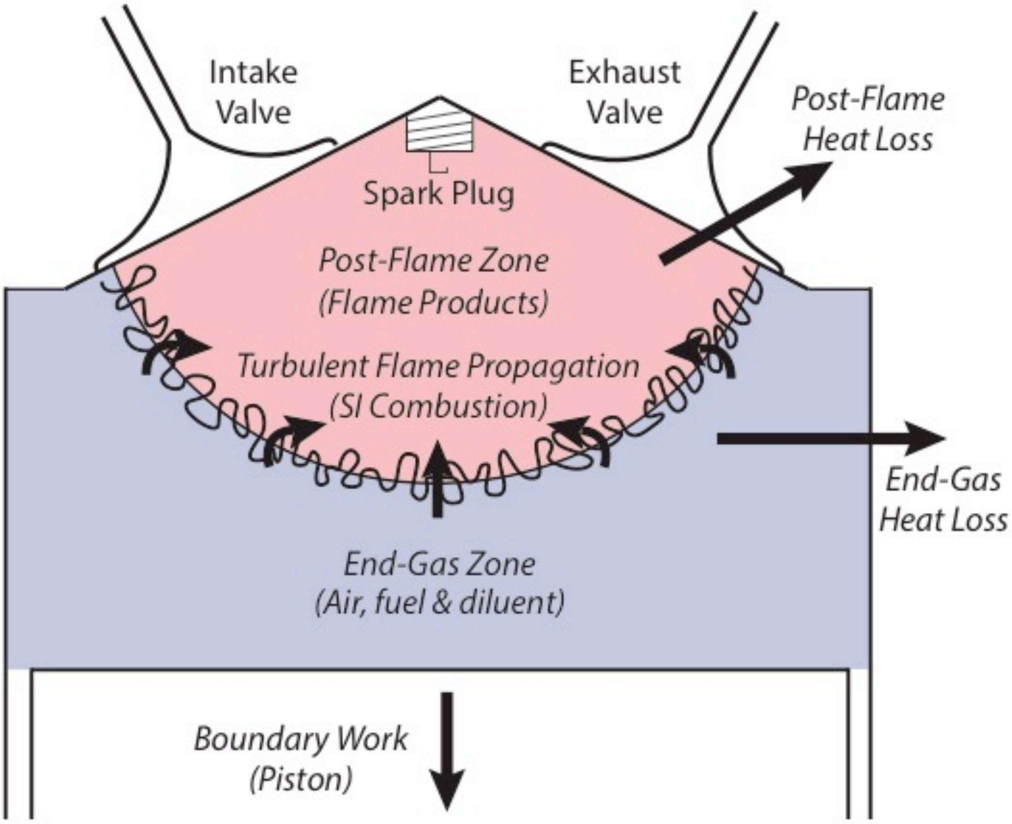

Figure 2.2 – Illustration of reduced order two-zone model for spark-ignited engines.

Reduced order models have also been applied to HCCI combustion simulations. Single-zone models with detailed chemical kinetics, such as the one in [15], have been used with good success to predict ignition delay times in engines. The burn rate, however, tends to be grossly overestimated as a result of having no spatial resolution of temperature and compositional gradients. Thus, these models resemble constant volume bombs once the ignition threshold is reached. Some researchers have addressed this shortcoming by incorporating multiple zones, which can provide approximate temperature distributions based on some assumed mechanism of heat or mass transfer [16], [17], as illustrated in Figure 2.3. Others have maintained the lower-zonal approach by resorting to empirical burn rate models [18]. These lump important chemical and transport effects into a single burn profile, thus avoiding the rapidly increasing computational overhead caused by the addition of predictive chemistry zones.

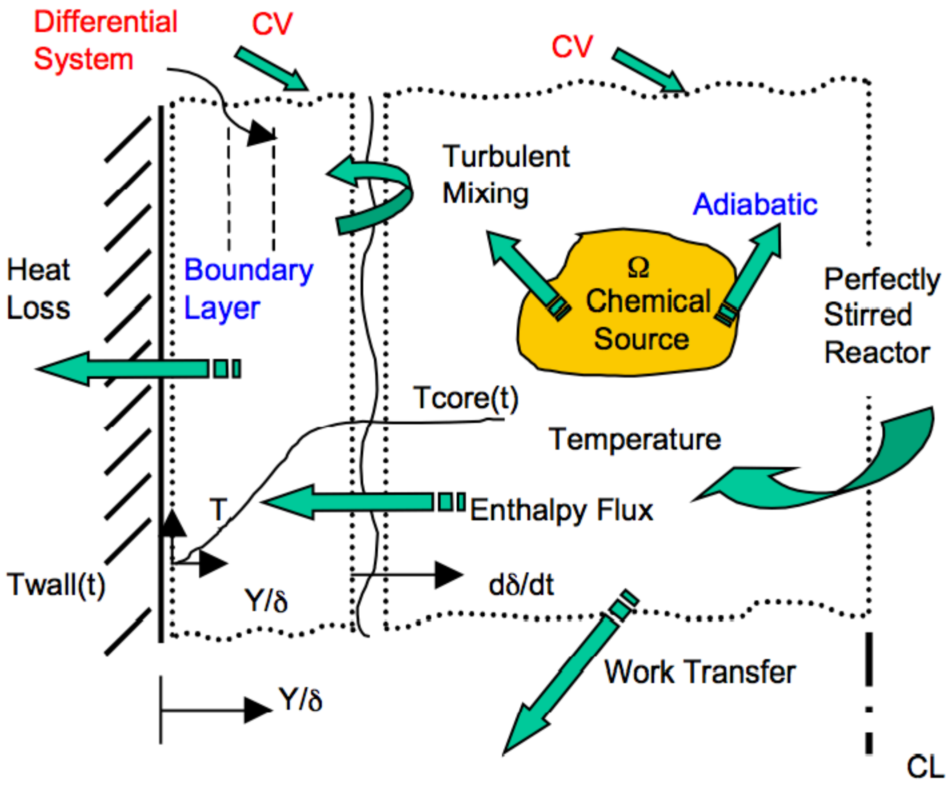

Figure 2.3 – Multi-zone HCCI model of Fiveland et al. [16] considering boundary layer regions for improved accuracy in burn rate predictions.

Currently, a reduced order model for advanced SACI combustion is not available in the literature. SI end-gas knock models based on ignition delay integrals or reduced chemistry have been extensively used [19]-[21], but these are primarily interested in predicting the occurrence of knock, so little attention was paid to accurate modeling of the subsequent burn rate. This gap in our computational capability for advanced combustion research provides the primary motivation for this work. The following section introduces our proposed conceptual model and presents the mathematical formulation that will be used within the experimental analysis and engine simulations subsequently developed.

2.2 Reduced Order Thermodynamic Model for SACI Combustion Engines

The fundamental representation of SACI combustion that will be used in all subsequent analytical and modeling tools developed for this work is presented in this section. Recalling the visual depiction of the general research and modeling framework in Figure 2.4, the reduced order model described in this chapter is the central component in the SACI combustion modeling process.

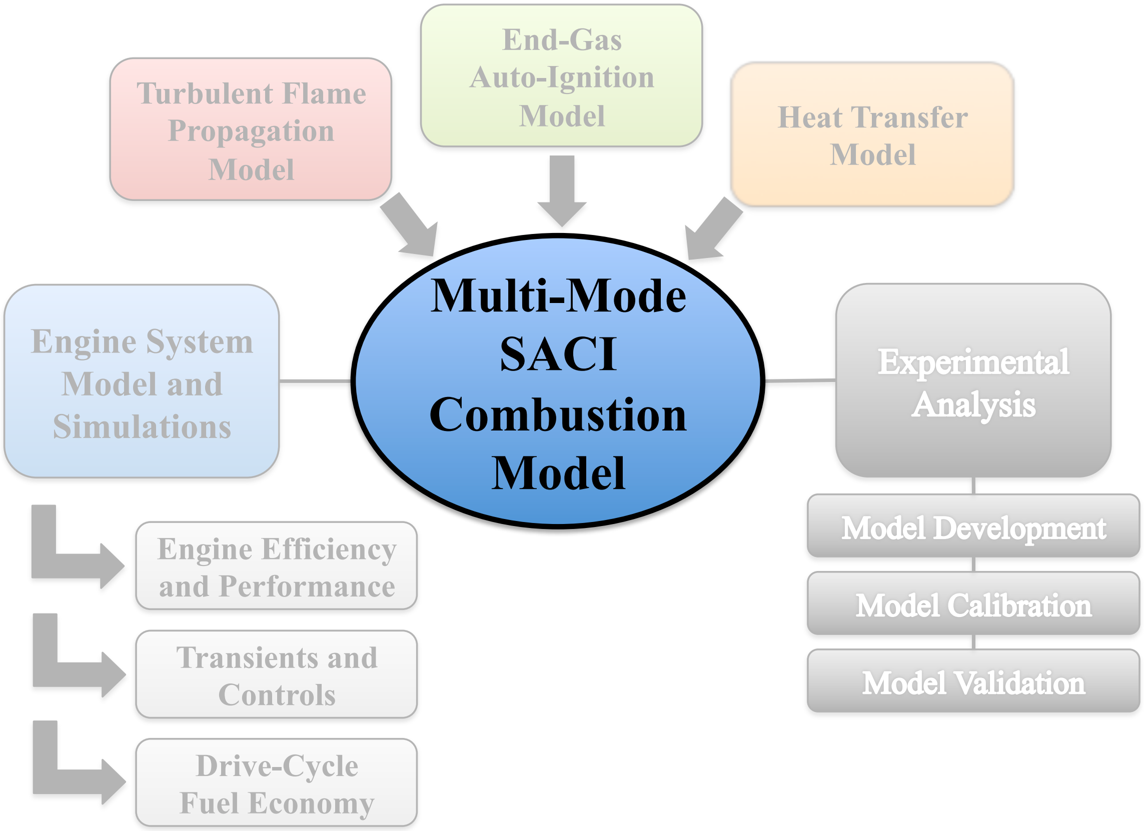

Figure 2.4 – General research framework for experimental analysis, model development and simulation of advanced SACI combustion engines. The central component of this work is the reduced order model for multi-mode SACI combustion described in this section.

2.2.1 Conceptual Model Description

Combining existing approaches for HCCI and SI combustion modeling within reduced order frameworks, we have devised a novel conceptual representation for SACI combustion, as shown in Figure 2.5. At the time of spark, the fuel-air-diluent charge in the cylinder is divided into two zones: the end-gas zone and the post-flame zone. The post-flame zone contains all the mass that has been consumed by the flame, transferred from the end-gas at a rate determined by flame propagation. The assumed constant pressure combustion process across the flame is constrained to the infinitely thin interface dividing the zones. The species in the post-flame zone are assumed to be at chemical equilibrium based on the current pressure and temperature. The end-gas is initially unreacted, but as the temperature increases during compression by the piston and the flame, auto-ignition chemistry drives the conversion of unburned species into combustion products. The next section translates this conceptual model into mathematical terms for use in quantitative analysis and computational studies.

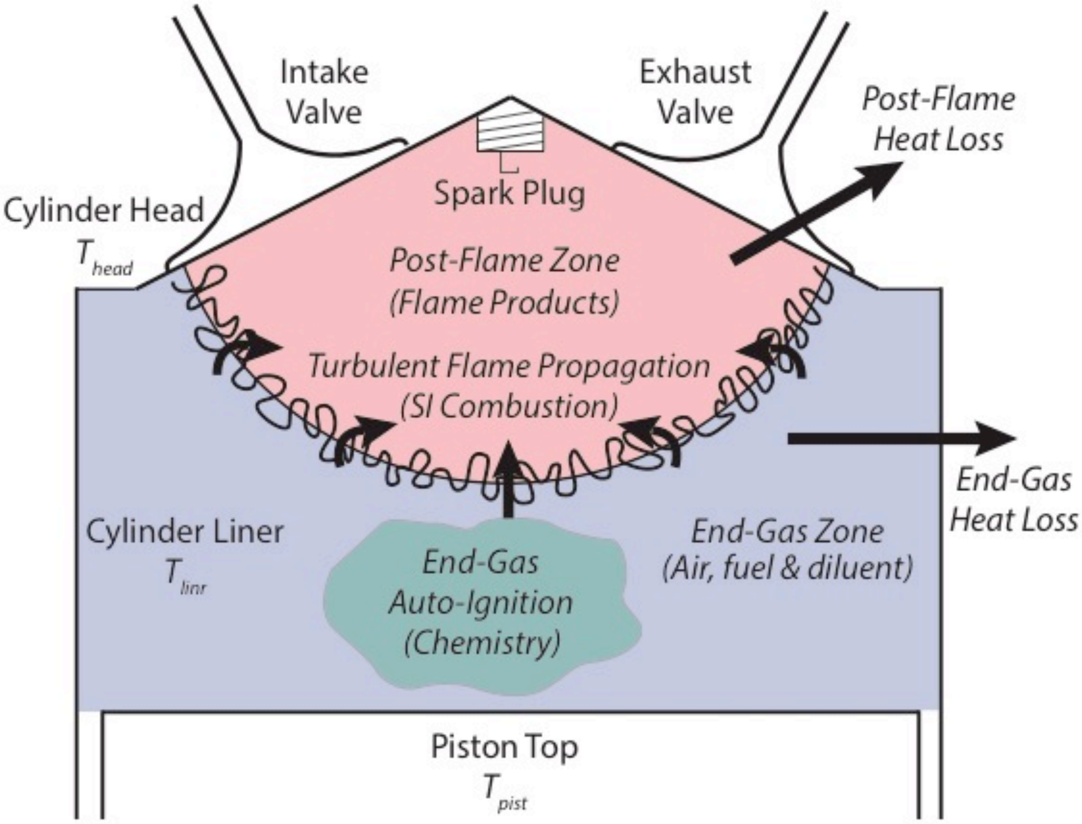

Figure 2.5 – Conceptual two-zone thermodynamic model for SACI combustion.

2.2.2 Mathematical Formulation

The following section presents a mathematical formulation for the conceptual two-zone model described in Section 2.2, to be used in thermodynamic analysis and simulations of SACI combustion engines. The approach presently adopted solves the global and end-gas state and composition using species and energy conservation equations. The post-flame zone state and composition is then determined algebraically by a simple mass and energy balance. The high-fidelity computational SACI model by Martz [4] employs a similar method, and has been used as a key guide for this work. In general, the variables directly related to the end-gas and post-flame zones are denoted by the subscripts u and b, respectively. It is worth stressing that this notation is historically consistent, but the subscripts do not necessarily signify unburned and burned quantities, since the SACI model presented here allows for auto-ignition chemistry in the end-gas. Also, the term 'global' will be used here to refer to the combined end-gas and post-flame system as a whole.

Combustion and Chemistry

The global rate of change for the k^{th} species is given by the individual contributions from end-gas auto-ignition $\left(\dot{m}_{AI}^{k}\right)$, flame propagation $\left(\dot{m}_{FL}^{k}\right)$, and evolution of post-flame zone equilibrium $\left(\dot{m}_{b}^{k}\right)$:

$$\frac{dm^k}{dt} = \dot{m}_b^k + \dot{m}_{FL}^k + \dot{m}_{AI}^k \tag{2.1}$$

The rate of change of the k^{th} species in the end-gas is computed in a similar fashion, considering only the contributions from auto-ignition $\left(\dot{m}_{u,AI}^{k}\right)$ and flame propagation $\left(\dot{m}_{u,FL}^{k}\right)$:

$$\frac{dm_u^k}{dt} = \dot{m}_{u,FL}^k + \dot{m}_{u,AI}^k \tag{2.2}$$

The evolution of post-flame zone composition is computed based on the equilibrium state for the current pressure and post-flame zone temperature $\left(Y_{b,EQ}^{k}\Big|^{P,T_b}\right)$:

$$\dot{m}_b^k = m_b \left(\frac{Y_{b,EQ}^{k}\Big|^{P,T_b} - Y_b^k}{\Delta t} \right) \tag{2.3}$$

where m_b and Y_b^k are the mass and composition of the post-flame zone at the previous time, and Δt is the time step.

Flame propagation is modeled as a constant pressure combustion process where the end-gas species (Y_u^k) are converted into constant pressure and enthalpy equilibrium products $\left(Y_{EQ}^k\big|^{P,h_u}\right)$ at the mass burning rate for flame propagation $\left(\dot{x}_{b,FL}\right)$. The rate equation for the global system is:

$$\dot{m}_{FL}^k = m\left(Y_{EQ}^k\big|^{P,h_u} - Y_u^k\right)\dot{x}_{b,FL} \tag{2.4}$$

where m is the total cylinder mass. In the end-gas, we only need to account for the consumption of species by the flame:

$$\dot{m}_{u,FL}^k = -mY_u^k\dot{x}_{b,FL} \tag{2.5}$$

The species rate of change due to auto-ignition is given by the approximate equation:

$$\dot{m}_{AI}^k = m_u\left(\frac{Y_u^k|^{AI} - Y_u^k}{\Delta t}\right) \tag{2.6}$$

where m_u and Y_u^k are the current end-gas mass and composition. $Y_u^k|^{AI}$ is obtained from the local end-gas reaction progress $x_{b,EG}$, where the unburned reactants ($Y_{u,reac}^k$), taken at some time before any combustion occurs, go to combustion products ($Y_{u,prod}^k$) assuming either complete combustion or equilibrium:

$$Y_u^k|^{AI} = \left(1 - x_{b,EG}\right)Y_{u,reac}^k + x_{b,EG}Y_{u,prod}^k \tag{2.7}$$

The difference between using a complete products assumption versus equilibrium depends on the temperatures encountered during auto-ignition. For very lean/dilute HCCI combustion temperatures are typically below 2000 K, so using complete products is likely sufficient without a notable sacrifice in accuracy, but with a significantly lower computational expense. However, for large parametric sweeps we cannot know *a priori* what the temperatures will be, so equilibrium is assumed for better accuracy.

Conservation of Energy

The total internal energy rate equation for a closed system may be written based on the First Law of Thermodynamics as:

$$\frac{dU}{dt} = -P\frac{dV}{dt} - \dot{Q}^{HT} \tag{2.8}$$

where the first term accounts for boundary work based on the cylinder pressure P and the rate of volume change computed using the standard geometric relations for a crank-slider mechanism. The second term accounts for heat transfer losses to the walls. Integrating Equation (2.8) gives the updated total energy of the global system, which can then be used with the volume to fully define the new state and obtain the pressure and temperature change. Crevice flows and blow-by, as well as direct fuel injection during the firing portion of the closed cycle, are currently not modeled.

For the end-gas, we use an open cycle version of the First Law of Thermodynamics, and recast it in terms of total enthalpy H_u:

$$\frac{dH_u}{dt} = V_u\frac{dP}{dt} - \dot{Q}_u^{HT} + \sum \dot{m}_{u,FL}^{k} h_u^k \tag{2.9}$$

V_u is the end-gas zone volume, $\dot{Q}_u^{HT}$ is the zone-specific heat transfer, and $\sum \dot{m}_{u,FL}^{k} h_u^k$ is the enthalpy out-flow due to flame consumption. The benefit of this formulation is that dP/dt can be readily obtained from the global solution. The updated end-gas state can then be set using the pressure and the integrated enthalpy value. The total energy and enthalpy formulations in Equations (2.8) and (2.9) account for changes in chemical and sensible energy without the need for an explicit combustion source term.

Post-Flame State and Composition

The post-flame state and composition is computed algebraically from the global and end-gas solution:

$$m_b^k = m^k - m_u^k \tag{2.10}$$

$$V_b = V - V_u \tag{2.11}$$

$$u_b = \frac{mu - m_u u_u}{m_b} \tag{2.12}$$

where the post-flame temperature is obtained by setting the state in the properties routines with the density $\left(\sum m_b^k / V_b\right)$ and specific internal energy (u_b). For numerical stability, the above equations are only used when the mass in the post-flame zone is above 1% of the total. During this initial period, the state is assumed to exist at the adiabatic flame temperature.

2.2.3 Model Summary and Computational Application

The reduced order model presented in this chapter provides the mathematical framework that will be used in experimental analysis, model development and simulation of advanced SACI combustion. To compute the time evolution of important quantities such as pressure, zonal temperatures and composition, the model requires knowledge of initial conditions, engine geometry, heat transfer and combustion heat release rates, the latter being the most important and difficult to obtain. The subsequent chapters will address individual sub-models and the integration of the thermodynamic SACI model into a complete advanced combustion engine simulation.

2.3 References

[1] T. Poinsot, S. Candel, and A. Trouve, “APPLICATIONS OF DIRECT NUMERICAL SIMULATION TO PREMIXED TURBULENT COMBUSTION,” *Progress in Energy and Combustion Science*, vol. 21, pp. 531–576, 1996.

[2] U. Piomelli, “Large-eddy simulation: achievements and challenges,” *Progress in Aerospace Sciences*, vol. 35, no. 4, pp. 335–362, 1999.

[3] C. K. Law, *Combustion Physics*, First Edition. Cambridge University Press, 2006.

[4] J. B. Martz, “SIMULATION AND MODEL DEVELOPMENT FOR AUTO-IGNITION AND REACTION FRONT PROPAGATION IN LOW-TEMPERATURE HIGH-PRESSURE LEAN-BURN ENGINES,” Ph. D. Thesis, University of Michigan, 2010.

[5] A. Babajimopoulos, D. N. Assanis, D. L. Flowers, S. M. Aceves, and R. P. Hessel, “A fully coupled computational fluid dynamics and multi-zone model with detailed chemical kinetics for the simulation of premixed charge compression ignition engines,” *International Journal of Engine Research*, vol. 6, no. 5, pp. 497–512, 2006.

[6] R. Dahms, C. Felsch, O. Röhl, and N. Peters, “Detailed chemistry flamelet modeling of mixed-mode combustion in spark-assisted HCCI engines,” *Proceedings of the Combustion Institute*, 2010.

[7] X. Wang, H. Xie, L. Xie, L. Zhang, L. Li, T. Chen, and H. Zhao, “Numerical simulation and validation of SI-CAI hybrid combustion in a CAI/HCCI gasoline engine,” *Combustion Theory and Modelling*, vol. 17, no. 1, pp. 142–166, 2013.

[8] J. A. Gatowski, E. N. Balles, K. M. Chun, F. E. Nelson, J. A. Ekchian, and J. B. Heywood, “Heat release analysis of engine pressure data,” *SAE 841359*, 1984.

[9] M. F. J. Brunt, H. Rai, and A. L. Emtage, “The Calculation of Heat Release Energy from Engine Cylinder Pressure Data,” *SAE 981052*, 1998.

[10] M. Fathi, R. K. Saray, and M. D. Checkel, “Detailed approach for apparent heat release analysis in HCCI engines,” *Fuel*, vol. 89, no. 9, pp. 2323–2330, 2010.

[11] R. J. Tabaczynski, C. R. Ferguson, and K. Radhakrishnan, “A Turbulent Entrainment Model for Spark-Ignition Engine Combustion,” *SAE 770647*, 1977.

[12] J. B. Heywood, J. M. Higgins, P. A. Watts, and R. J. Tabaczynski, “Development and Use of a Cycle Simulation to Predict SI Engine Efficiency and NOx Emissions,” *SAE 790291*, 1979.

[13] Y. G. Guezennec and W. Hamama, “Two-Zone Heat Release Analysis of Combustion Data and Calibration of Heat Transfer Correlation in an I. C. Engine,” *SAE 1999-01-0218*, 1999.

[14] A. E. Catania, D. Misul, A. Mittica, and E. Spessa, “A Refined Two-Zone Heat Release Model for Combustion Analysis in SI Engines,” *JSME International Journal*, vol. 46, no. 1, 2003.

[15] S. B. Fiveland and D. N. Assanis, “A Four-Stroke Homogeneous Charge Compression Ignition Engine Simulation for Combustion and Performance Studies,” *SAE 2000-01-0332*, 2000.

[16] S. B. Fiveland and D. N. Assanis, “DEVELOPMENT AND VALIDATION OF A QUASI-DIMENSIONAL MODEL FOR HCCI ENGINE PERFORMANCE AND EMISSIONS STUDIES UNDER TURBOCHARGED CONDITIONS,” *SAE 2002-01-1757*, 2002.

[17] N. P. Komninos, D. T. Hountalas, and D. A. Kouremenos, “Development of a New Multi-Zone Model for the Description of Physical Processes in HCCI Engines,” *SAE 2004-01-0562*, 2004.

[18] A. Babajimopoulos, P. Challa V S S, G. A. Lavoie, and D. N. Assanis, “MODEL-BASED ASSESSMENT OF TWO VARIABLE CAM TIMING STRATEGIES FOR HCCI ENGINES: RECOMPRESSION VS. REBREATHING,” presented at the ASME Internal Combustion Engine Division 2009 Spring Technical Conference, ICES2009-76103, 2009.

[19] S. Y. Ho and T.-W. Kuo, “A Hydrocarbon Autoignition Model for Knocking Combustion in SI Engines,” *SAE 971672*, 1997.

[20] T. Noda, K. Hasegawa, M. Kubo, and T. Itoh, “Development of a Transient Knock Prediction Technique by Using a Zero-Dimensional Knock Simulation with Chemical Kinetics,” *SAE 2004-01-0618*, 2004.

[21] E. Ortiz-Soto, D. Assanis, and A. Babajimopoulos, “A comprehensive engine to drive-cycle modelling framework for the fuel economy assessment of advanced engine and combustion technologies,” *International Journal of Engine Research*, vol. 13, no. 3, pp. 287–304, 2012.

CHAPTER 3

EXPERIMENTAL ANALYSIS OF ADVANCED COMBUSTON ENGINES

3.1 Heat Release Analysis of Experimental Cylinder Pressure Data

Current research into advanced combustion strategies for improved efficiency and emissions, such as Homogeneous-Charge Compression-Ignition (HCCI) and Spark-Assisted HCCI (SACI), requires fundamental understanding of the important combustion processes. Heat release analysis is an essential tool for interpreting experimental pressure data and provides key inputs for model development and validation.

Heat release analysis typically follows a regressive modeling approach, where the measured in-cylinder pressure, combustion efficiency and estimated trapped masses are used to calculated the mean gas temperature, composition and combustion heat release. Many frameworks have been presented in the literature using various approaches for cylinder pressure heat release analysis [1]-[8]. The most common method employs the First Law of Thermodynamics with a single-zone assumption to estimate the contributions of piston work, heat transfer and energy release due to combustion to the closed-system energy balance. Two-zone and multi-zone approaches have also been proposed in an effort to improve the accuracy of the results [3], [5], [9]; however, the added complexity and assumptions related to specific combustion modes are not always justified. Other approaches, such as the Rassweiler-Withrow [10] method can also be used to extract the normalized mass fraction burned (MFB).

The present work introduces a new heat release analysis framework that addresses the special demands of experimental advanced combustion research, which includes unconventional valve strategies, elevated dilution levels, and multi-mode combustion regimes. The ACE-HR (Advanced Combustion Engine Heat Release) framework was developed for experimental cylinder pressure heat release analysis of engines employing spark-ignition (SI), HCCI or an advanced combustion mode, such as SACI. This experimental analysis tool provides important combustion-related results necessary for the development and validation of the SACI combustion model at the core of this work, as illustrated in Figure 3.1.

ACE-HR employs the First Law approach and incorporates an extensive set of tools for gas properties, residual gas fraction (RGF) estimation and heat transfer modeling. An extended analysis for advanced combustion engine experiments also provides estimates of auto-ignition timing, flame vs. auto-ignition heat release fractions, auto-ignition heat release rate, and end-gas/post-flame states.

Several factors can strongly influence the accuracy of the heat release analysis results, on both an absolute and trend-wise basis. For typical engine experiments, these factors include engine geometry, data acquisition system errors, cylinder pressure data pre-conditioning, gas properties estimation, trapped mass estimation, combustion efficiency and heat transfer modeling. Therefore, it is important to understand the relative sensitivities of heat release analysis results to systematic errors in experimental data and from incorrect modeling assumptions.

This chapter demonstrates the comprehensive framework for heat release analysis of advanced combustion engines (ACE-HR). Closed-cycle KIVA simulation data for HCCI and SACI combustion modes are used for validation. Key input factors and modeling assumptions are evaluated using experimental data analysis and sensitivity assessment.

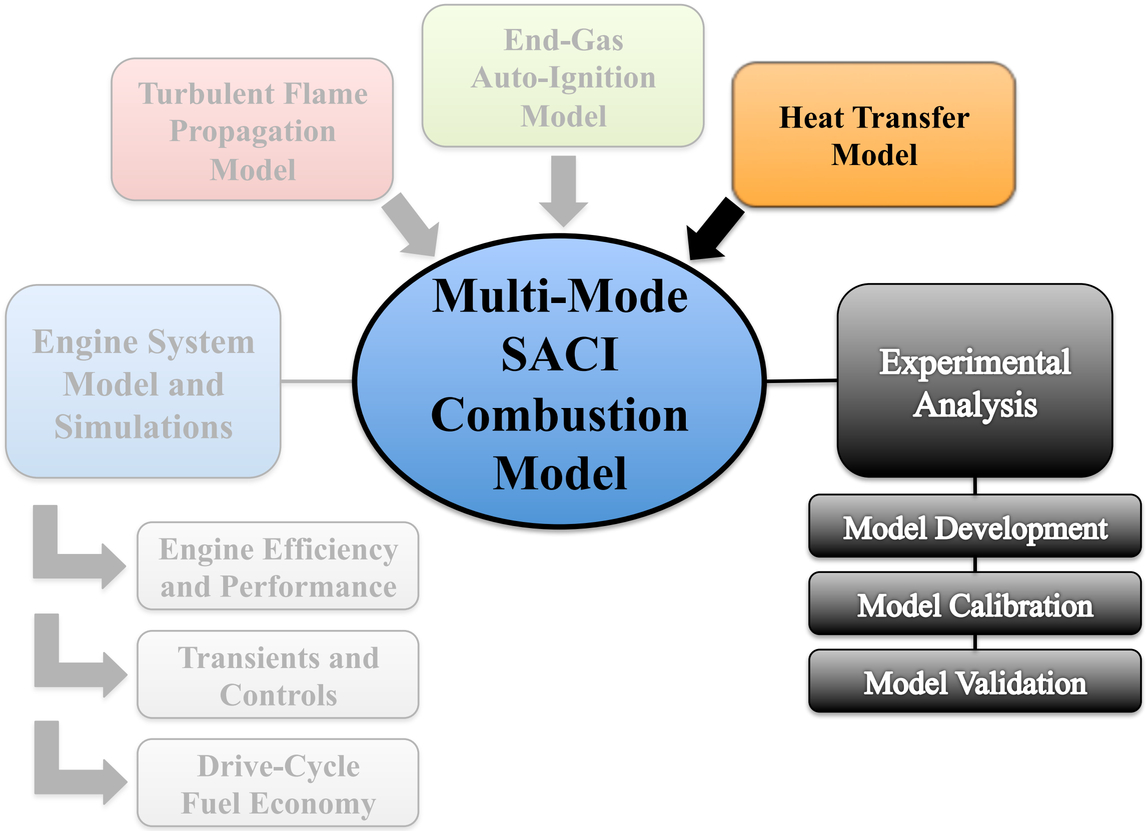

Figure 3.1 – General research framework for experimental analysis, model development and simulation of advanced SACI combustion engines. The ACE-HR experimental analysis presented in this chapter provides key combustion results for the development, calibration and validation of the SACI combustion model.

3.2 ACE-HR Experimental Analysis Methods

The ACE-HR package is implemented in MATLAB with a graphical user interface (GUI), shown in Figure 3.2. The most important methods, models and assumptions employed in ACE-HR are presented and discussed in the following sections.

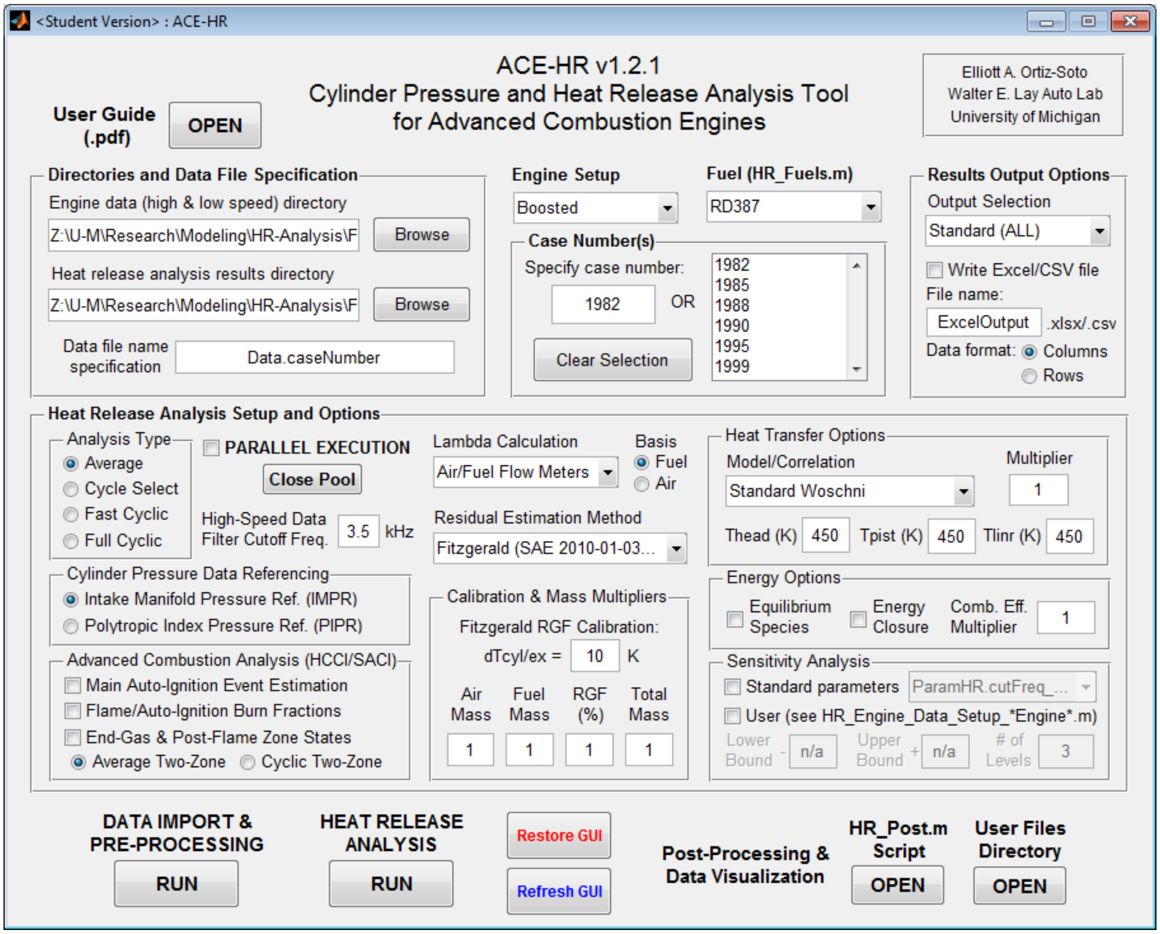

ACE-HR v1.2.1
Cylinder Pressure and Heat Release Analysis Tool
for Advanced Combustion Engines

Elliott A. Ortiz-Soto
Walter E. Lay Auto Lab
University of Michigan

Directories and Data File Specification
Engine data (high & low speed) directory: Z:\U-M\Research\Modeling\HR-Analysis\F
Heat release analysis results directory: Z:\U-M\Research\Modeling\HR-Analysis\F
Data file name specification: Data.caseNumber

Engine Setup: Boosted
Fuel (HR_Fuels.m): RD387
Case Number(s)
Specify case number: 1982 OR 1982 1985 1988 1990 1995 1999

Results Output Options
Output Selection: Standard (ALL)
☐ Write Excel/CSV file
File name: ExcelOutput .xlsx/.csv
Data format: ● Columns ○ Rows

Heat Release Analysis Setup and Options
Analysis Type: ● Average ○ Cycle Select ○ Fast Cyclic ○ Full Cyclic
☐ PARALLEL EXECUTION
High-Speed Data Filter Cutoff Freq. 3.5 kHz
Lambda Calculation: Air/Fuel Flow Meters
Basis: ● Fuel ○ Air
Residual Estimation Method: Fitzgerald (SAE 2010-01-03...

Heat Transfer Options
Model/Correlation: Standard Woschni
Multiplier: 1
Thead (K) 450 Tpist (K) 450 Tlinr (K) 450

Cylinder Pressure Data Referencing
● Intake Manifold Pressure Ref. (IMPR)
○ Polytropic Index Pressure Ref. (PIPR)

Calibration & Mass Multipliers
Fitzgerald RGF Calibration: dTcyl/ex = 10 K
Air Mass 1 Fuel Mass 1 RGF (%) 1 Total Mass 1

Energy Options
☐ Equilibrium Species ☐ Energy Closure Comb. Eff. Multiplier 1

Advanced Combustion Analysis (HCCI/SACI)
☐ Main Auto-Ignition Event Estimation
☐ Flame/Auto-Ignition Burn Fractions
☐ End-Gas & Post-Flame Zone States
● Average Two-Zone ○ Cyclic Two-Zone

Sensitivity Analysis
☐ Standard parameters ParamHR.cutFreq_...
☐ User (see HR_Engine_Data_Setup_*Engine*.m)
Lower Bound - n/a Upper Bound + n/a # of Levels 3

Figure 3.2 – ACE-HR graphical user interface.

3.2.1 Combustion Heat Release

The cylinder pressure heat release analysis employs a basic First Law of Thermodynamics approach [11] to estimate the combustion heat release rate. The gross chemical heat release rate from combustion ($dQ_{hr,ch}/dt$) can be expressed as:

$$\frac{dQ_{hr,ch}}{dt} = mc_v\frac{dT}{dt} + P\frac{dV}{dt} + \dot{Q}_{wall} \tag{3.1}$$

where m, c_v and T are the estimated mass, specific heat at constant volume and mean gas temperature, respectively. P is the measured cylinder pressure and V is the total cylinder volume, computed from the crank-slider relationships and engine geometry. The first two terms on the right hand side equal the net apparent heat release rate ($dQ_{hr,net}/dt$), which includes the change in sensible energy and piston work.

Errors in the data, pre-conditioning or estimation of mass and heat transfer can directly influence $Q_{hr,ch}$ at the end of combustion. The overall energy balance can be assessed using the ratio of gross chemical heat release at exhaust valve opening (EVO) and expected fuel energy released ($\eta_{comb} m_{fuel} Q_{LHV}$). A second metric for energy closure, α_{HT}, is also computed as a ratio of heat transfer, which can be directly applied to the calculated heat loss to close the overall energy balance:

$$\alpha_{HT} = \frac{\eta_{comb} m_{fuel} Q_{LHV} - Q_{hr,net}(EVO)}{Q_{loss}(EVO)} \tag{3.2}$$

The first term in the numerator gives the expected chemical energy release from the combustion efficiency η_{comb}, fuel mass m_{fuel} and lower heating value of the fuel Q_{LHV}. The second term in the numerator and the term in the denominator are the cumulative net heat release and heat loss, respectively, at EVO. It must be noted that using α_{HT} to force energy closure will lump errors from other sources, such as incorrect pressure referencing, compression ratio or residual mass estimation, into heat transfer, and could cause undesirable behavior in the shape of the heat release curve. Therefore, this method should only be used to enforce energy closure when a thorough evaluation of the experimental data and preliminary analysis reveals that heat transfer is the most likely source of discrepancy.

The burn fraction x_b is computed from the cumulative gross chemical heat release $Q_{hr,ch}$, integrated and normalized between the start (SOC) and end of combustion (EOC). SOC and EOC are assumed to be at the minimum and maximum points of $Q_{hr,ch}$, respectively. After correction of the burn fraction curve for SOC and EOC, the final rate of heat release ($RoHR$) can then be obtained by numerical differentiation of the cumulative heat release with respect to crank-angle.

The heat release analysis follows an iterative approach to allow for variable gas properties based on the estimated combustion profile. To reduce the computational expense when performing full cycle-by-cycle heat release analysis, an initial estimate of the properties on a crank-angle basis are obtained from an initial ensemble-averaged analysis.

3.2.2 Temperature, Gas Properties and Composition

The mean gas temperature required for heat release analysis and properties estimation is computed from the Ideal Gas Law equation of state:

$$T = \frac{PV}{mR} \tag{3.3}$$

Adequate treatment of gas properties is critical for obtaining reasonable estimates of trapped masses, temperature and combustion heat release. Of particular importance is the specific heat ratio γ, since the First Law formulation (Equation (3.1)) can also be expressed in terms of this single property [11] by employing some additional assumptions. A number of functional forms for γ have been proposed in the literature to capture the dependence on temperature, composition and, to a lesser extent, pressure [1], [2], [6], [9], [12]-[14]. However, it can be expected that the simple correlations used in these approaches will limit their applicability to general combustion analysis. To avoid these possible shortcomings, gas properties routines based on the thermodynamic data in the JANAF tables [15] and Burcat's Thermodynamic Database [16] are used along with a 15-species equilibrium model. The species included are: H, O, N, H_2, OH, CO, NO, O_2, H_2O, CO_2, N_2, AR, NO_2, HO_2 and fuel. The expressions for the properties were obtained from the Chemkin III manual [17], and the 15-species equilibrium model was initially developed and validated by Depcik et al. [18], which is itself an extension of the original 12-species equilibrium proposed by Olikara and Bormann [19]. The properties routines allow for multi-component fuels, such as gasoline surrogates, Primary Reference Fuels (PRF) and gasoline-ethanol blends. The fuel library includes some of the most commonly used fuels: Hydrogen (H_2), Iso-octane (i-C_8H_{18}), n-Heptane (n-C_7H_{16}), Pentene (n-C_5H_{12}), Benzene (C_6H_6) and Ethanol (C_2H_5OH). A gasoline surrogate composed of Iso-octane, Pentene, and benzene can be automatically generated to match the H/C ratio and molecular weight (MW) of a specific fuel.

The mean gas composition is assumed to be a mixture of unburned and burned gases, weighted by the burned mass fraction x_b:

$$Y^k = (1 - x_b) \cdot Y_u^k + x_b \cdot Y_b^k \tag{3.4}$$

where Y^k is the mass fraction of the k^{th} species. The unburned species Y_u^k are modeled as a mixture of fresh reactants Y_{reac}^k, determined from the given equivalence ratio, and the EGR composition, weighted by the trapped EGR fraction, as defined in the following section:

$$Y_u^k = (1 - EGR) \cdot Y_{reac}^k + EGR \cdot Y_{EGR}^k \tag{3.5}$$

The burned species Y_b^k are obtained from either equilibrium at the instantaneous temperature and pressure (Y_{equil}^k), or by assuming complete combustion products (Y_{prod}^k), again determined by the equivalence ratio.

3.2.3 Trapped Mass Estimation

Adequate estimation of the trapped mass in the cylinder is crucial when calculating quantities such as mean gas temperature, which affects gas properties and the overall energy balance. The total mass includes the fuel, air and re-circulated exhaust gas (EGR):

$$m_{tot} = m_{fuel} + m_{air} + m_{e-EGR} + m_{i-EGR} \tag{3.6}$$

where m_{fuel} is the injected fuel mass, m_{air} is the inducted air mass, m_{e-EGR} is the mass of EGR introduced with the intake flow (external) and m_{i-EGR} is the internally trapped EGR or RGF mass.

In most engine experiments, several independent methods are used to measure the mass flow of fuel and air into the cylinder, such as direct metering and exhaust Lambda (λ) sensors. The air-fuel ratio can also be computed using emissions data from the standard Brettschneider formula [20] and atomic balance expressions for carbon and oxygen. The external EGR fraction, which can be significant in advanced combustion engines, is computed from CO_2 measurements in the intake and exhaust, with the resulting EGR mass obtained based on the total incoming flow.

One of the major uncertainties in the trapped mass calculation typically arises from the residual mass estimation. It becomes even more significant in advanced combustion engines employing valve strategies such as Negative Valve Overlap (NVO), where large amounts of hot internal EGR are used to achieve and control auto-ignition. In these cases, the total EGR content can range between 30% and 60% of the total mass, with a large part of it recycled internally [21]. There can be uncertainty in the intake EGR calculation as well, especially if there is a high degree of unmixedness in the intake manifold at the point where CO_2 is measured.

Simple indirect estimation methods for residual mass are most commonly used in experimental heat release analysis and are employed in the present work. These are typically based on equations of state and assumptions about the thermodynamic processes during exhaust. However, the lack of temperature and composition measurements can lead to significant errors in the residual mass estimates. Direct measurement techniques are available [22], [23], but they are generally costly and impractical. Engine models using one-dimensional gas dynamics calculations and boundary conditions from experimental data can also be used to estimate the trapped masses [24]. However, the need for a complete engine model introduces additional complexities without a guaranteed improvement in accuracy. Another general limitation of the available methods is that they do not provide any information about stratification, which affects ignition and burn rates in advanced combustion engines.

Three residual mass estimation methods can be used in ACE-HR for NVO operation: the State Equation Method [25], the Yun and Mirsky Method [25], [26] and the Fitzgerald Method [25], [27]. Details of the models and implementation, as well as an in-depth assessment of the various methods, can be found in [25]. All three methods calculate the residual mass at exhaust valve closing (EVC), from which the RGF (internal) and total EGR fraction (internal + external) can be determined. The total EGR fraction can then be computed using:

$$EGR = \frac{m_{e-EGR} + m_{i-EGR}}{m_{tot}} \tag{3.7}$$

To incorporate the gas properties routines in the residual estimation methods, it is necessary to calculate an approximate EGR composition. The exhaust gas is assumed to be composed of fresh reactants (Y_{reac}^{k}) and complete combustion products (Y_{prod}^{k}) computed for the given fuel and measured equivalence ratio, weighted by the combustion efficiency (η_{comb}):

$$Y_{EGR}^{k} = (1 - \eta_{comb}) \cdot Y_{reac}^{k} + \eta_{comb} \cdot Y_{prod}^{k} \tag{3.8}$$

Although this assumption does not take into account the actual exhaust species measured by an emissions bench, the discrepancy in the calculated properties is expected to be minor.

The coupling between pressure, temperature, properties and mass requires all methods to be implemented using an iterative approach for EGR mass and composition. For cycle-by-cycle heat release analysis, the residual masses for individual cycles are computed using the pressure data during the gas-exchange period of the previous cycle.

3.2.4 Combustion Efficiency

The combustion efficiency is computed from exhaust emissions measurements using the standard approach presented by Stivender [28], corrected to account for the re-inducted fuel from EGR dilution. The exhaust combustion efficiency correction was proposed by Chang [29] after comparing HCCI engine experiments and cycle simulations employing the re-breathing valve strategy. He found that the steady state burned fuel mass was always higher in the simulations than the experiments, and concluded that the experimental combustion efficiency needed to be modified based on the EGR fraction. Using a simple burned fuel mass conservation argument, he derived an in-cylinder combustion efficiency ($\eta_{comb,cyl}$) expression as a function of the measured exhaust combustion efficiency ($\eta_{comb,exh}$) and EGR:

$$\eta_{comb,cyl} = \frac{(EGR + 1) - \sqrt{(EGR + 1)^2 - 4 \cdot EGR \cdot \eta_{comb,exh}}}{2 \cdot EGR} \tag{3.9}$$

This expression will always yield a lower efficiency than the emissions calculation.

3.2.5 Heat Transfer Modeling

Calculation of the gross heat release from cylinder pressure data requires the wall heat transfer loss to be estimated over the heat release analysis range. Typical engine experiments lack measurements of heat flux, gas temperature distributions and turbulent flow fields, so global heat transfer correlations are commonly employed. The wall heat transfer rate is the sum of the individual contributions from the head, piston and liner:

$$\dot{Q}_{wall} = \sum hA_i(T - T_i) \tag{3.10}$$

where the subscript i denotes the various heat transfer regions. The head area (A_{head}) and the piston area (A_{pist}) are specified for a given engine, and the liner area (A_{linr}) is computed using the crank-slider equations. The wall temperatures at these three regions (T_{head}, T_{pist} and T_{linr}) are also prescribed as constant values, whereas the mean gas temperature (T) is calculated on a crank-angle basis during the heat release analysis. The global convective heat transfer coefficient h (W/m^2-K) is generally a function of the instantaneous pressure, temperature, volume, and operating conditions. The present analysis incorporates some of the most common global heat transfer correlations found in the literature, originally derived from the Reynolds Analogy and are in general a function of temperature T, pressure P and mean piston speed $\overline{S_p}$, as well as some length scale given by the volume V, the bore B or a the instantaneous chamber height L. The expression for the heat transfer coefficients are listed in Table 3.1 and converted to use common units of length [m], pressure [kPa], temperature [K] and velocity [m/s].

Table 3.1 – Global engine heat transfer correlations in ACE-HR.

Woschni [30]	$h = 3.26 \cdot B^{-0.2} \cdot P^{0.8} \cdot T^{-0.53} \cdot w^{0.8}$ (3.11)
Chang [31]	$h = 3.4 \cdot 3.26 \cdot L^{-0.2} \cdot P^{0.8} \cdot T^{-0.73} \cdot w_{mod}^{0.8}$ (3.12)
Hohenberg [32]	$h = 3.26 \cdot V^{-0.06} \cdot P^{0.8} \cdot T^{-0.4} \cdot \left(\overline{S_p} + 1.4\right)^{0.8}$ (3.13)
Eichelberg [33]	$h = 0.24 \cdot P^{1/2} \cdot T^{1/2} \cdot \overline{S_p}^{1/3}$ (3.14)
Woschni-ACE	$h = 3.26 \cdot B^{-0.2} \cdot P^{0.8} \cdot T^{-0.55} \cdot w_{ACE}^{0.8}$ (3.15)

All Woschni-based correlations have a characteristic gas velocity term w (m/s) calculated from the expression:

$$w = C_1\overline{S_p} + C_2 V_d \left(\frac{T_r}{P_r V_r}\right)(P - P_{mot}) \tag{3.16}$$

The characteristic velocity is proportional to the mean piston speed, $\overline{S_P}$ (m/s), and a 'pressure velocity' given by the difference between firing and motoring pressure (P_{mot}) scaled by the displaced volume, V_d (m^3), and the temperature (T_r), pressure (P_r) and volume (V_r) at some reference condition (e.g. IVC). As suggested by Woschni, the constants used in the heat transfer correlation are $C_1 = 2.28$ and $C_2 = 3.24 \times 10^{-3}$ for the closed cycle. The 'pressure velocity' or 'flame enhancement' term is assumed to account for increases in heat transfer due to flame-induced turbulence. Based on experimental heat flux studies in an HCCI engine, Chang [31] proposed a modified characteristic velocity term for the Woschni correlation with a 1/6 reduction factor on the flame enhancement term, as well as a different temperature coefficient.

These and other global heat transfer correlations have been the subject of numerous studies investigating their applicability to different combustion modes [31],

[34]-[44], and various modified correlations for HCCI combustion, such as the Chang correlation, also called the Modified Woschni (Equation (3.12)), have been developed [31], [37], [41], [43]. SACI combustion, however, has yet to be the subject of an in-depth heat transfer investigation.

To address this shortcoming, we are proposing a hybrid model designated as the Woschni-ACE model, based on the general form of the standard Woschni correlation, but incorporating the reduced pressure velocity term found in the Modified Woschni (Chang) correlation. During the flame propagation phase or pure SI combustion, the model behaves exactly like the standard Woschni model. After the estimated occurrence of auto-ignition, the reduced pressure velocity term is imposed to decrease heat transfer on the same order as in the Chang model. Because in the experimental analysis the ignition timing estimate occurs based on the calculated burn fraction curve, this model is implemented in practice by running two independent calculations with and without the reduced pressure velocity term, and the results are then linearly blended around the ignition point. The performance of this model is examined in more detail against the existing correlations in Section 3.3.2.

Still, heat transfer remains one of the largest unknowns in engine modeling, and the uncertainty can be high when analyzing non-conventional combustion regimes, such as HCCI and SACI. In the absence of heat flux measurements or a new correlation specifically developed for advanced combustion modes, the existing correlations or derived models based on these correlations are the best available.

3.2.6 Estimation of Main Auto-Ignition Event

Auto-ignition is the principal feature of combustion modes such as HCCI and SACI, so the effects of operating conditions and control strategies on auto-ignition timing need to be understood. The chemically controlled nature of auto-ignition makes it difficult to identify with certainty where the gas initially begins reacting (e.g. 0% burn fraction). However, it is still possible to estimate the location of the main auto-ignition event (θ_{AI}) by inspection of the heat release profile. For HCCI combustion, this is straightforward since combustion proceeds solely due to auto-ignition. However, SACI combustion requires a more rigorous approach to capture the transition between slow spark-ignited deflagration and fast auto-ignition heat release. Persson et al. [45] identified two distinct regions in the heat release rate from SACI experiments using the second derivative of the $RoHR$ and defined the first region as the *Initial Slow Heat Release* (ISHR) phase. In the present work, we extend this approach and use the time of maximum curvature in the $RoHR$ as an additional metric to define the transition. The curvature, κ_{RoHR}, is calculated using the following expression:

$$\kappa_{RoHR} = \frac{RoHR''}{(1 + RoHR'^2)^{3/2}} \tag{3.17}$$

where $RoHR'$ and $RoHR''$ are the first and second derivatives of the heat release rate. It was found that the best results could be achieved by scaling the $RoHR$ and the crank-angle range to unity order. Figure 3.3 shows the $RoHR$, $RoHR''$ and κ_{RoHR} of a SACI case. The time of the first maxima in the $RoHR''$ and the first maxima in the curvature are too late and too early, respectively, compared to the expected location of auto-ignition identified by visual inspection of the $RoHR$ curve. However, the average of these two results was found to be a robust and accurate method for detecting auto-ignition and is shown with an asterisk in the figure. The present auto-ignition estimation method is limited to cases where the effects of auto-ignited combustion can be clearly detected. Conditions in which the pressure data does not show any significant auto-ignition heat release will incur potential errors.

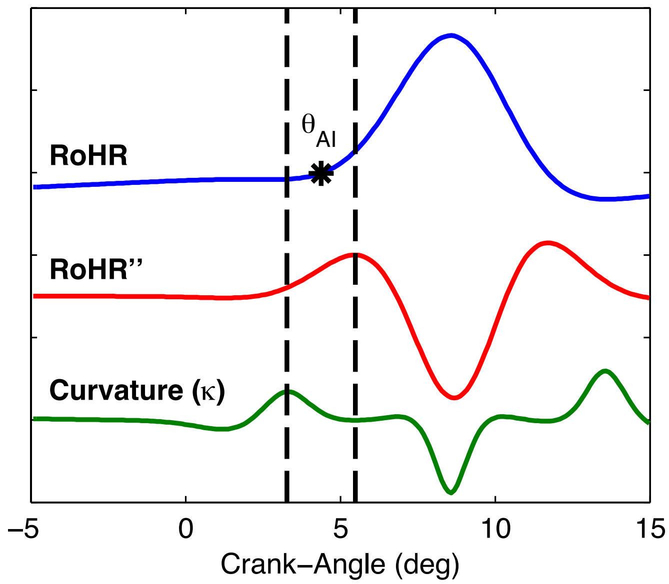

Figure 3.3 – RoHR, second derivative of the RoHR (RoHR'') and curvature (κ) used for estimating main auto-ignition event.

3.2.7 Estimation of SACI Flame and Auto-Ignition Burn Fractions

To investigate the effects of SACI operating conditions and flame propagation on the subsequent auto-ignition burn rate, the overall heat release rate can be further dissected into the relative contributions from flame propagation and end-gas auto-ignition. Using transient one-dimensional computational studies, Martz et al. [46] investigated the behavior of laminar reaction fronts propagating into auto-igniting end-gases at conditions representative of SACI operation. It was found that the rapid increase in end-gas temperature due to auto-ignition reduced transport effects across the flame and combustion within the front eventually became chemically controlled. The transition to the full auto-ignition regime was considered complete when the reaction front and chemical time scales were nearly equivalent, which occurred at the point of maximum chemical power where the end-gas temperature was around 1600 K. Further modeling studies of SACI combustion using full three-dimensional engine simulations in KIVA

[47] showed similar behavior, with the transition duration proportional to the rate of end-gas reaction progress between the onset of ignition and the time of maximum chemical power.

In the absence of detailed knowledge of chemistry and turbulent flame propagation, as is the case in the majority of engine experiments, the present work utilizes the estimated time of auto-ignition to approximate transition between combustion modes and to compute the relative burn fractions due to flame $(x_{b,FL})$ and auto-ignition $(x_{b,AI})$. The flame propagation rate $(\dot{x}_{b,FL})$ and local end-gas reaction progress $(x_{b,EG})$ are also obtained from these quantities by respectively differentiating and normalizing the burned gas fractions. Using a simple exponential function and assuming an end-gas burn fraction at ignition equal to 5% we can fit a smooth curve up to ignition, beyond which it is assumed the flame will quickly quench. The 5% burn assumption is based on visual inspection of extensive experimental and high fidelity simulation results of HCCI combustion. Larger estimation errors are expected in cases displaying noticeably slower transition chemistry or where the maximum flame propagation burn fraction is on the order of 5%.

The auto-ignition combustion efficiency $(\eta_{comb,AI})$ is computed from the measured overall efficiency $(\eta_{comb,cyl})$ using a scaling function to account for the mass already burned by flame propagation at the onset of ignition $(x_{b,FL,IGN})$:

$$\eta_{comb,AI} = \frac{\left(\eta_{comb,cyl} - x_{b,FL,IGN}\right)}{\left(1 - x_{b,FL,IGN}\right)} \tag{3.18}$$

This expression assumes that the only source of combustion inefficiency comes from auto-ignition, and implies that the post-flame zone equilibrium products will eventually reach complete combustion products. Although, this could lead to some errors in heat release predictions, they will be lumped into the general modeling inaccuracies of employing a highly simplified thermodynamic two-zone model to the complex processes found in advanced multi-mode combustion engines.

3.2.8 Estimation of End-Gas and Post-Flame Zone States

The end-gas temperature is a key input to ignition delay and laminar flame speed correlations, and the estimates can be used to gain more in-depth insights into engine combustion and performance. The two-zone thermodynamic model presented in Sections 2.2 and 2.2.2 is employed to compute the evolution of end-gas and post-flame zone temperatures. In the context of experimental analysis, the mean temperature, pressure and overall heat transfer are assumed known from experimental data and heat release analysis, but the composition is allowed to vary. The estimated flame and auto-ignition burn rates described in the previous section are used to model combustion.

The laminar flame speed at any point during the flame propagation phase can be computed using correlations in the literature. The recent correlations developed by Middleton et al. [48] for a wide range of conditions, including SACI-type temperatures and dilution levels are used for flame speed prediction. The correlations were developed using iso-octane as a gasoline surrogate, due to the similar burning velocities and ignition delays of the two fuels. These are described in more detail in Section 5.4.5.

3.2.9 Data Pre-Conditioning

Cylinder pressure data pre-conditioning is standard practice in experimental heat release analysis. The individual pressure traces are first subjected to a low-pass filter to reduce noise from the high-speed data acquisition system and minimize errors when computing numerical derivatives. A 2nd order low-pass Butterworth digital filter has been implemented in ACE-HR with a prescribed cutoff in the range of 2-5 kHz, which was found to adequately capture the high pressure-rise and heat release rates characteristic of auto-igniting and knocking cases.

The cylinder pressure signal, measured on a relative basis using a piezoelectric transducer, is referenced using one of the two most common techniques, namely Intake Manifold Pressure Referencing (IMPR) or Polytropic Index Pressure Pegging (PIPR). Details and reviews of these and other available methods can be found in the literature [49], [50], so they are discussed here only briefly.

The IMPR technique assumes the cylinder pressure is equal to the dynamic intake manifold or runner pressure, measured on an absolute basis, around intake BDC. This is used to compute a pressure offset P_{off} that is the applied to the rest of the cylinder pressure signal. If the manifold pressure waves are small, the average intake pressure can also be used for referencing without a noticeable sacrifice in accuracy.

The PIPR technique assumes a polytropic compression process to calculate P_{off} from the following equation:

$$P_{off} = P_1 - \frac{P_2 - P_1}{(V_1/V_2)^n - 1} \tag{3.19}$$

The pressures (P_1 and P_2) and volumes (V_1 and V_2) are chosen early in the compression stroke after IVC ($\theta_1 = -100$ deg ATDC and $\theta_2 = -60$ deg ATDC), and the range can be adjusted if analyzing cases with very advanced spark timings. The polytropic index n can be calculated from the pressure data and operating conditions; however, Randolph [49] showed that this approach can be very sensitive to measurement errors and recommended that a fixed prescribed value of 1.32 be used. It must be noted, that this value was based on conventional spark-ignition engines, and must be re-evaluated for highly diluted advanced combustion engines.

Engine experiments are typically performed under steady state conditions, with a number of cycles on the order of 200 to 1000 recorded to obtain statistically significant results and assess possible combustion stability issues. Studies involving HCCI, SACI or highly dilute SI, in particular, often exhibit high variability; hence the standard approach of analyzing the ensemble average pressure trace can mask the variability of cycle-by-cycle data and might not provide the most representative picture of combustion behavior. Thus, analysis of the full cyclic pressure ensemble is considered the preferred method for this study.

3.3 Heat Release Analysis and Thermodynamic SACI Model Assessment

The ACE-HR heat release analysis model has been assessed against a series of closed-cycle high fidelity engine simulations for both HCCI and SACI combustion modes using the KIVA-3V computational fluid dynamics (CFD) code. In the KIVA model, HCCI combustion was modeled using detailed chemical kinetics with a coupled CFD/Multi-Zone (MZ) approach [51]. Flame propagation in SACI combustion was simulated using a Coherent Flamelet Model (CFM) [52], with the laminar flame properties obtained from the correlations of Middleton et al. [48]. The skeletal 215 species iso-octane mechanism of Tham et al. [53] was used to compute the chemical kinetics and gas properties in all of the simulations. A full description of the KIVA-CFMZ model can be found in [47], [54].

The KIVA results provide a known data set with detailed predictions of heat release rates, in-cylinder temperatures, auto-ignition timing, flame speeds and other key parameters not resolved or measured in engine experiments. The results are ideal for evaluating the heat release analysis methods. Uncertainties related to cylinder pressure referencing, mass and initial composition estimation, and combustion efficiency are eliminated, allowing the validation focus to remain on the subset of models and assumptions used to extract combustion information from experimental pressure data.

The engine configuration for the HCCI and SACI simulations is shown in Table 3.2. The associated computational mesh was developed based on detailed geometry from the experimental FFVA engine setup [21]. Three cases for each combustion mode were used for validating the proposed heat release analysis models and methods. The HCCI cases consist of an initial temperature sweep for nearly constant initial pressure, equivalence ratio (Φ) and EGR. Here the equivalence ratio is defined as the dimensionless molar ratio of the fuel to fresh air in the charge compared to the stoichiometric ratio of fuel to air. The equivalence ratio does not consider the O_2 in the EGR gases. The EGR includes contributions from both external and internal exhaust gases. In the SACI cases, the initial temperature and the spark timing are simultaneously varied to maintain the crank-angle at 50% burn (CA50) near 8 deg ATDC. The operating conditions for both HCCI and SACI cases are described in Table 3.3 and Table 3.4.

Table 3.2 – Engine geometry from experimental FFVA engine setup used in high-fidelity KIVA simulations of HCCI and SACI combustion.

Compression Ratio	12.41 (nominal)
Bore × Stroke (mm)	86.0 × 94.3
Displaced Volume (cm^3)	547.8
Connecting Rod Length (mm)	152.2
Head Geometry	Pent-roof
Piston Geometry	Bowl

Table 3.3 – Operating conditions for high-fidelity KIVA HCCI simulations.

Operating Conditions	**Case 1**	**Case 2**	**Case 3**
Engine Speed (rev/min)	1993	1996	1994
Initial Pressure (bar)	1.177	1.186	1.193
Initial Temperature (K)	541.9	537.1	533.6
Equivalence Ratio, Φ	0.6342	0.6212	0.6084
EGR (%)	49	49	49

Table 3.4 – Operating conditions for high-fidelity KIVA SACI simulations.

Operating Conditions	**Case 1**	**Case 2**	**Case 3**
Engine Speed (rev/min)	1991	1999	1996
Initial Pressure (bar)	1.214	1.255	1.252
Initial Temperature (K)	479.2	502.1	510.3
Equivalence Ratio, Φ	0.9907	0.9950	0.9996
EGR (%)	40	40	40
Spark Timing (deg ATDC)	−44	−34	−25

3.3.1 Heat Release, Temperature and Equilibrium

To better understand the sources of error in the heat release analysis, simulations of gradually increasing complexity were performed for **Case 2** of both HCCI and SACI combustion modes, starting with motored (non-firing, non-reacting) and adiabatic (AD) simulations, then firing and adiabatic simulations, and finally firing with heat transfer (HT) simulations. The pressure traces for each combustion mode are shown in Figure 3.4. As expected, the combustion phasing is much earlier in the adiabatic simulations, compared to the calculations that include heat loss.

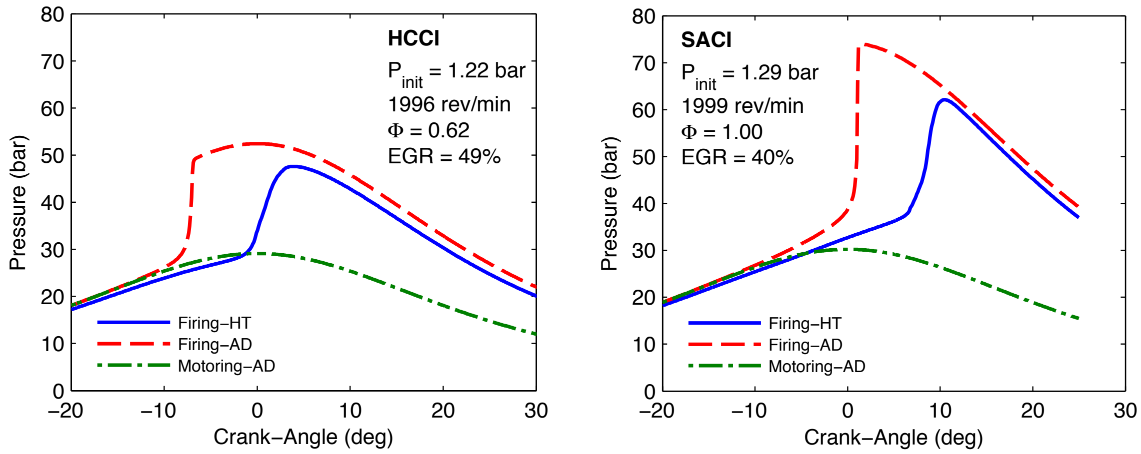

(a) (b)

Figure 3.4 – KIVA (a) HCCI and (b) SACI cylinder pressure results for motored-adiabatic (AD), firing-adiabatic runs and firing with heat transfer (HT) simulations.

The analysis of motored cases showed almost exact agreement between the KIVA and ACE-HR results, as can be seen from the temperature comparison in Figure 3.5. This implies that the heat release analysis is capable of estimating the mean gas temperature with good accuracy, given a known composition and heat transfer.

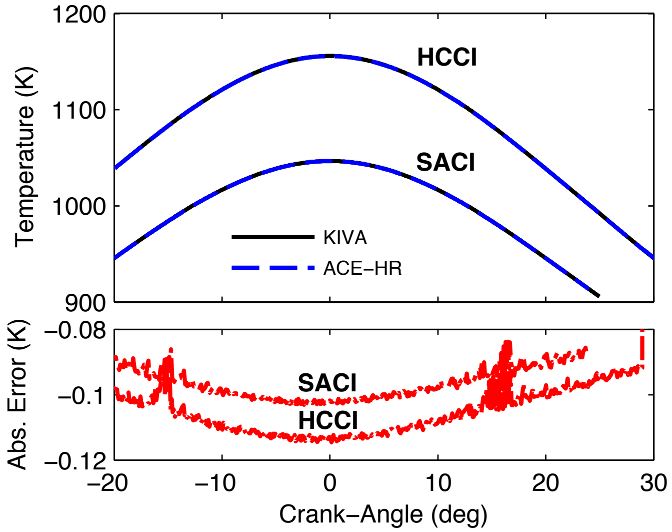

Figure 3.5 – Comparison of mean temperature between KIVA simulations and ACE-HR analysis estimate during motoring operation for HCCI (upper temperature data) and SACI (lower temperature data) conditions. The minimal absolute error between the KIVA and ACE-HR temperatures shown in the lower panel demonstrates the excellent agreement between the two results.

The firing-adiabatic runs are used to assess the effects of composition and properties on combustion heat release and temperature, shown in Figure 3.6. The analysis was performed with both equilibrium and non-equilibrium treatment of the burned products composition, as discussed in Section 3.2.2. It can be seen from the cumulative heat release (normalized) in Figure 3.6(a) that there is again excellent agreement between the KIVA and ACE-HR results. Small discrepancies are found during the initial state of ignition and at the end of combustion; however, the general shapes agree very well. The differences can be related to the temperature estimation, presented in Figure 3.6(b).

In the HCCI cases, the maximum temperature error was less than -0.15% at -7 deg ATDC, and becomes negligible beyond the peak temperature location. The error in the burn fraction has a similar behavior, with a maximum error of 0.04 fractional units at the same time in the cycle. The SACI cases show errors of similar magnitude. The likely source of the error is the lack of intermediate species kinetics in ACE-HR. During auto-ignition chemistry in KIVA, the iso-octane fuel molecule is initially broken into smaller fuel species, followed by production of CO and OH radicals, and finally CO is oxidized into CO_2, which accounts for the bulk energy release. The heat release analysis, however, treats the mean gas composition as a mixture of fresh reactants and complete (or equilibrium) combustion products. Thus, the mixture will contain a higher fraction of iso-octane until the fuel is globally oxidized into CO_2, resulting in a higher specific heat during the initial stages of ignition and an increase in the gross chemical heat release according to Equation 1, which in turn increases the temperature as well. The use of equilibrium products did not appear to have a major impact on the heat release and temperature estimates; however, the SACI case with equilibrium did show a slight decrease in the error for the burn fraction. This should be expected due to the higher peak temperatures seen during this combustion mode as a result of flame propagation. These relatively small effects when using equilibrium species during heat release analysis, even at high temperatures, are expected since most of the information regarding the state of the mixture is already contained in the pressure data. In a simulation, where temperature and pressure are calculated as a function of properties and composition, the difference from using equilibrium and non-equilibrium species would be much more noticeable.

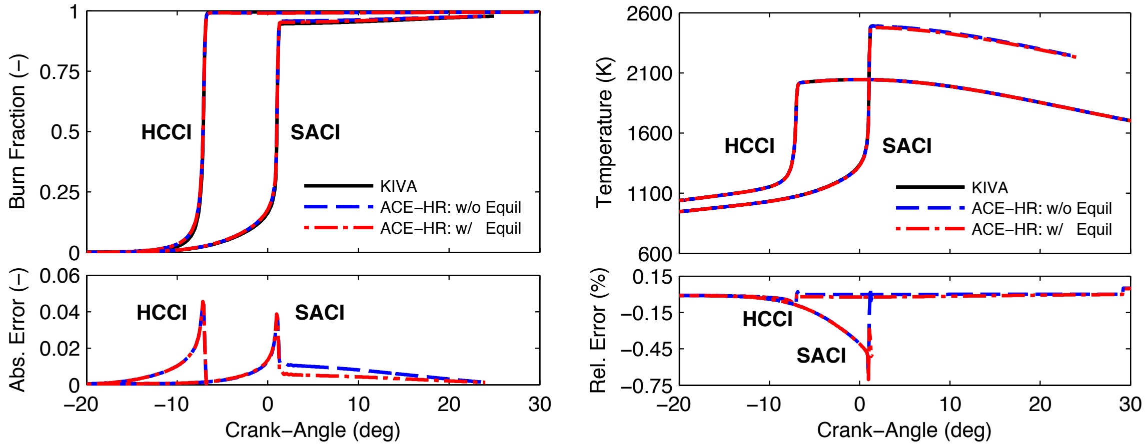

(a) (b)

Figure 3.6 – Comparison of (a) burn fraction and (b) mean gas temperature results for HCCI and SACI firing-adiabatic simulations between KIVA and ACE-HR. Results for equilibrium and non-equilibrium products in ACE-HR are shown.

3.3.2 Heat Transfer

Simulations allowing for wall heat losses are finally used to assess the effects of heat transfer modeling assumptions on the heat release analysis results. The heat transfer correlations described in 3.2.5 were employed in the analysis of both HCCI and SACI cases, assuming that the turbulence and heat transfer predictions in the high fidelity KIVA simulations are representative. Figure 3.7(a) shows the cumulative heat loss during the HCCI combustion period for the various correlations. Significantly different heat loss predictions are observed, especially after TDC when auto-ignition occurs. The Chang (2) correlation is the only one specifically developed for HCCI combustion, and as a result has the lowest energy balance error (10.2%) of the four published correlations, as seen in Figure 3.7(b). The proposed Woschni-ACE (5) correlation; however, shows an even lower energy balance error (3.6%), indicating the revised pressure velocity term in conjunction with the standard Woschni expression is a reasonably good approximation to the heat transfer behavior during HCCI operation.

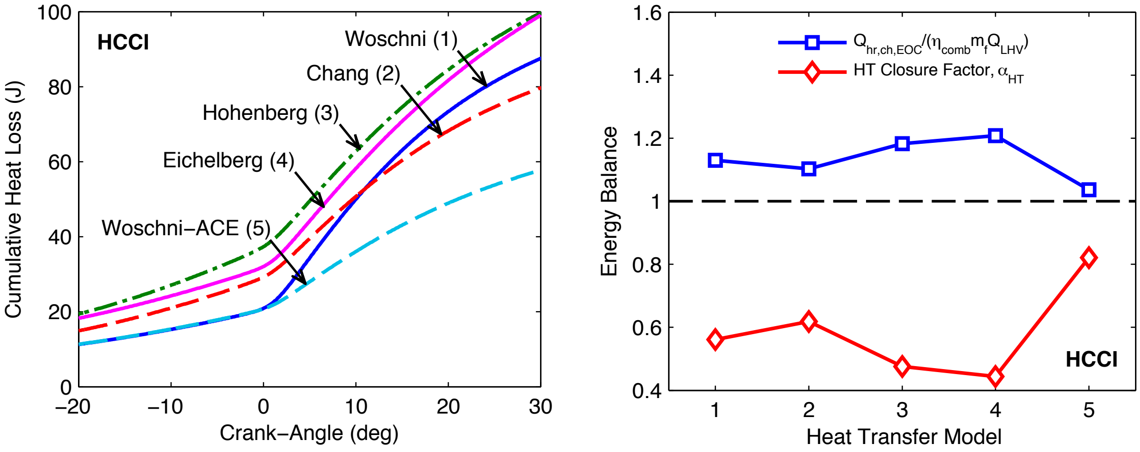

(a) (b)

Figure 3.7 – (a) Cumulative heat loss, (b) energy balance and heat transfer energy closure factor α_{HT} from various heat transfer correlations in ACE-HR analysis of HCCI case. The heat transfer models (1 to 5) refer to the correlations listed in the legend of panel (a) and listed in Table 3.1

The heat transfer energy closure factor, α_{HT}, is also presented in Figure 3.7(b), and is inversely proportional to the energy balance. Assuming that the energy balance errors are mostly due to heat transfer, then a larger error above unity in the cumulative heat release prediction requires a more significant heat transfer reduction. The effects of heat transfer errors, with (α_{HT} ON) and without (α_{HT} OFF) forced closure are shown in Figure 3.8, where CA02, CA10, CA50 and CA90 are the crank-angles at 2%, 10%, 50% and 90% burn, respectively. Even though the typical combustion phasing metric of CA50 is minimally affected by the heat transfer choice, the shape of the heat release curve towards the beginning and end of combustion is considerably more sensitive (blue squares). In this case, application of α_{HT} to force energy closure (red diamonds) greatly improves the agreement of combustion phasing results compared with KIVA (black circles).

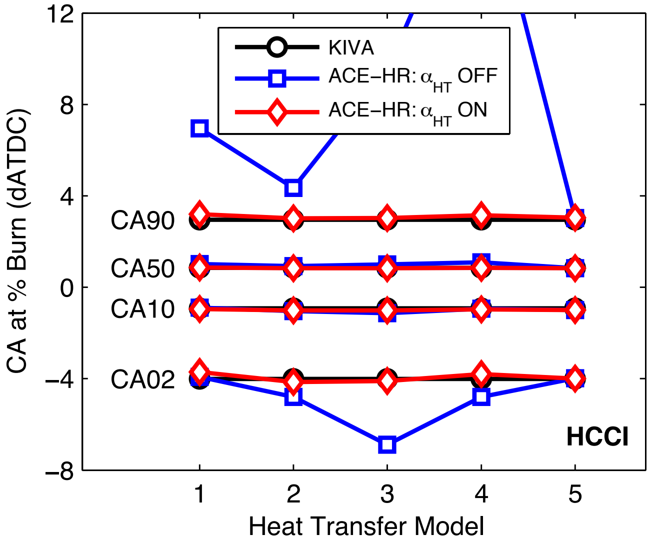

Figure 3.8 − Comparison of selected HCCI combustion phasing results between KIVA and ACE-HR. Analysis with (α_{HT} ON) and without (α_{HT} OFF) forced energy closure shown.

Similar results for the SACI combustion case are shown in Figure 3.9. Because of the flame propagation portion, it was expected that the standard heat transfer correlations would behave slightly better compared with the HCCI case. Even though the results in Figure 3.9(b) confirm this, flame propagation only consumes about 20% of the charge, so the improvement is not significant. As with the HCCI case, the proposed Woschni-ACE (5) correlation results in the smallest energy balance error.

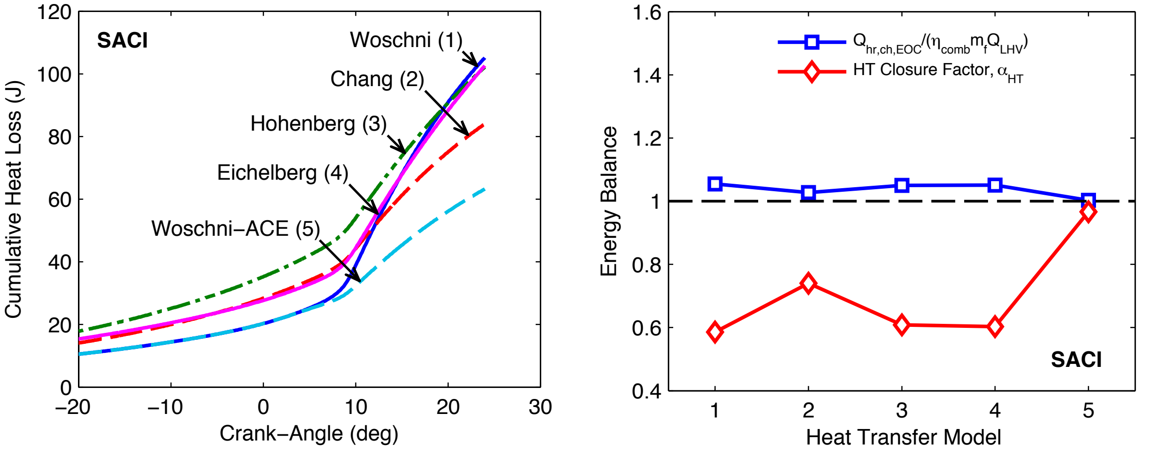

(a) (b)

Figure 3.9 – (a) Cumulative heat loss, (b) energy balance and heat transfer energy closure factor α_{HT} from various heat transfer correlations in ACE-HR analysis of SACI case. The heat transfer models (1 to 5) refer to the correlations listed in the legend of panel (a) and listed in Table 3.1

Figure 3.10 shows combustion phasing results for the SACI case, comparing KIVA (black circles) and ACE-HR with (red diamonds) and without (blue squares) forced closure. Some improvements in combustion phasing predictions during the initial combustion periods (CA02 and CA10) are again possible by applying α_{HT} to modify the heat transfer rate given by the different the models. Again, the Woschni-ACE heat transfer model provides the best energy closure and combustion phasing results. The Woschni-ACE model is subsequently applied to the rest of the HCCI and SACI cases presented.

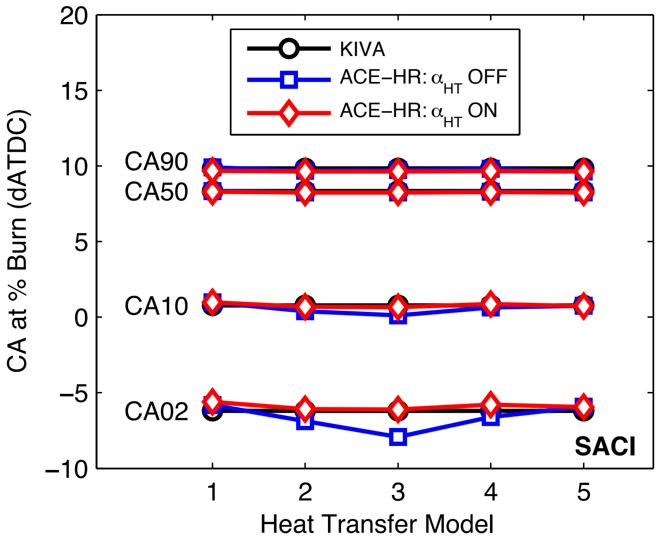

Figure 3.10 − Comparison of selected SACI combustion phasing results between KIVA and ACE-HR. Analysis with (α_{HT} ON) and without (α_{HT} OFF) forced energy closure shown.

The predictions for mean temperature for the HCCI and SACI cases using the Woschni-ACE heat transfer model is compared with the KIVA simulation results in Figure 3.11. With heat transfer, the maximum error in the HCCI temperature estimate changed to 1% below KIVA (−1%), whereas for the adiabatic case the maximum error was below the KIVA result by −0.15%. The SACI temperature error also increased in the same direction from −0.75% to −2%. The temperature was found to be relatively insensitive to the choice of heat transfer correlation, implying that the addition of heat transfer creates a systematic error independent of combustion mode or heat transfer model. This could be attributed to the fact that in an engine, and in a CFD simulation like KIVA, heat is only removed thorough the wall boundary layer, allowing the core gases to retain more heat and achieve a higher temperature compared with a single-zone thermodynamic model where heat is removed from the total charge uniformly.

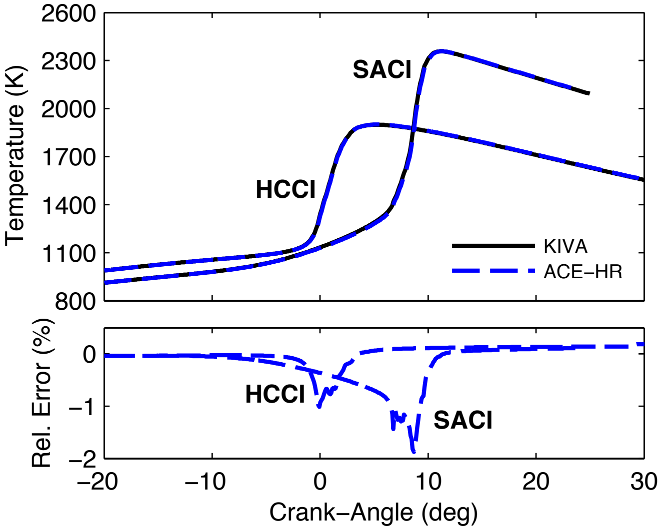

Figure 3.11 – Comparison of mean temperature predictions from ACE-HR and KIVA simulations for HCCI (lower temperature data) and SACI (higher temperature data) cases.

3.3.3 Advanced Combustion Analysis

After examining the modeling assumptions and associated limitations of the ACE-HR heat release analysis, the remainder of the validation discussion focuses on the HCCI and SACI combustion phasing studies described at the beginning of this section in Table 3.3 and Table 3.4. Figure 3.12 shows the cylinder pressures from KIVA for the six validation cases used as input to the ACE-HR analysis. The HCCI cases, shown in Figure 3.12(a), have increasingly later phasing as the initial temperature decreases, which slows combustion and reduces the maximum pressure. The SACI cases, shown in Figure 3.12(b), maintain similar overall combustion phasing and maximum pressure by trading-off initial temperature for spark advance. Earlier spark timing and lower IVC temperature results in pressure data that appears more SI-like than HCCI-like, whereas later spark timing and higher temperatures result in more HCCI-like behavior. The Woschni-ACE correlation with forced energy closure is used to model heat transfer in both the HCCI and SACI combustion modes. The burned gas is assumed to be composed of equilibrium products at the mean temperature and pressure.

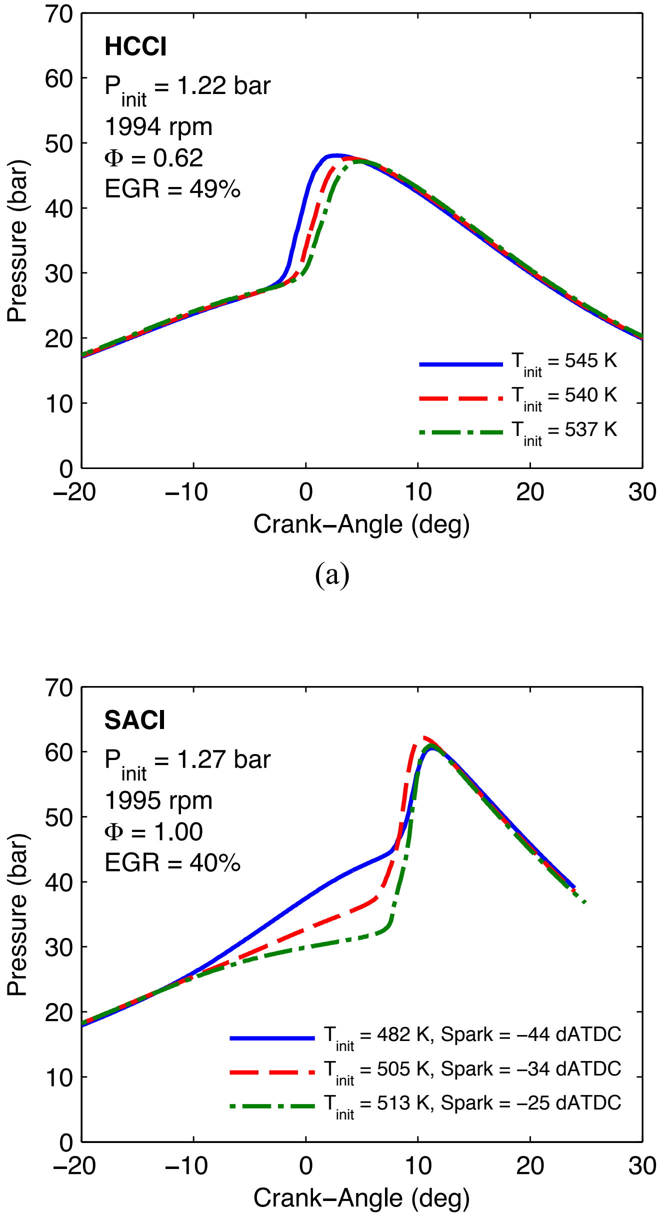

(a)

(b)

Figure 3.12 – KIVA cylinder pressure results for (a) HCCI and (b) SACI combustion phasing study used for ACE-HR heat release analysis validation.

Figure 3.13 presents the combustion phasing predictions from the heat release analysis compared with KIVA data for the HCCI and SACI validation cases. The data were extracted from the normalized cumulative mass fraction burned (MFB) curve. The results show excellent agreement, and the slight errors are limited to initial phases of combustion (e.g. CA02) for the SACI cases. These minor discrepancies can be attributed to composition and heat transfer modeling.

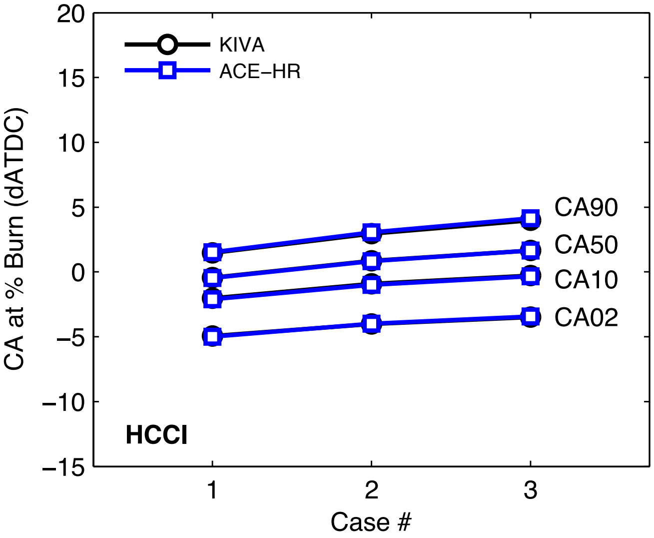

(a)

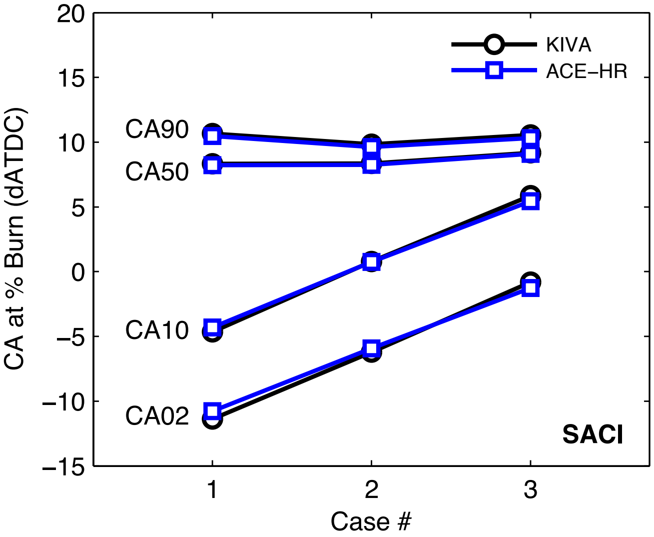

(b)

Figure 3.13 − Comparison of combustion phasing results predicted by KIVA simulations and ACE-HR analysis for (a) HCCI and (b) SACI validation cases.

The mean temperature estimate demonstrated very similar trends throughout the validation cases. For the HCCI cases, the error in temperature ranges from near 0% during compression and expansion, to a maximum close to −1% around the time of ignition. For the SACI cases, negligible errors in temperature are again found during both compression and expansion; however, the maximum error during combustion increased to 2%. For both combustion modes, the error in maximum temperature in every case is less than 0.5%.

The estimated location of the main auto-ignition event is shown in Figure 3.14 for the HCCI and SACI cases. By visually inspecting the burn fraction curves, it can be seen that the auto-ignition timing, marked by the asterisks, qualitatively agrees with the expected locations. Even for SACI cases with later phasing and moderate fractions of initial flame propagation, the auto-ignition event is relatively well identified. This is critical for the subsequent steps of the advanced combustion analysis.

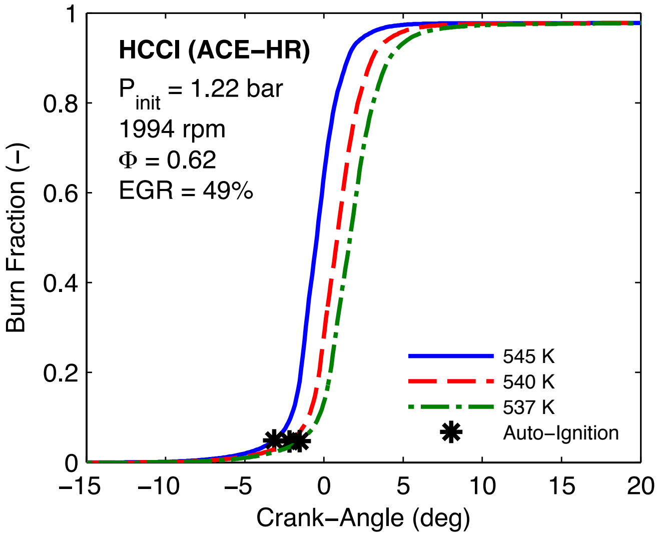

(a)

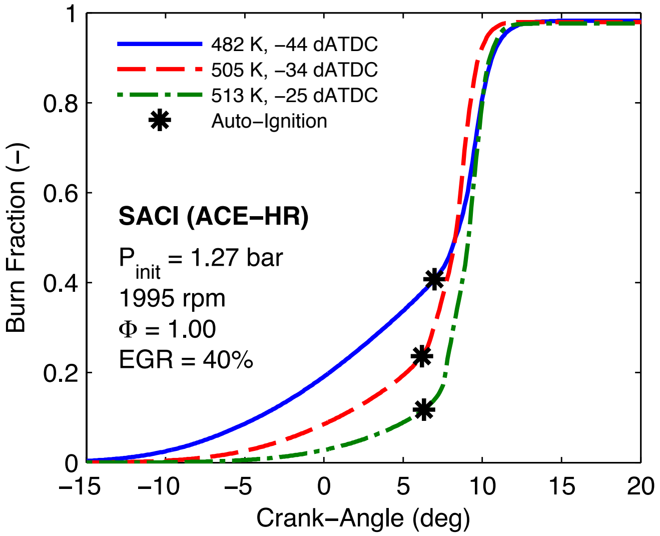

(b)

Figure 3.14 – Comparison of the timing of the auto-ignition events with burn fraction time histories for (a) HCCI and (b) SACI validation cases.

A comparison between the KIVA and the ACE-HR predictions for burn fractions by flame and auto-ignition for one of the SACI cases is presented in Figure 3.15. Overall, the plots show very good agreement between the models. The main differences are observed during the early stages of end-gas chemistry. The ACE-HR method uses an exponential function to transition from zero burn to ignition. The KIVA results show that flame heat release rate quickly becomes negligible, and appears to be representatively captured by the proposed method.

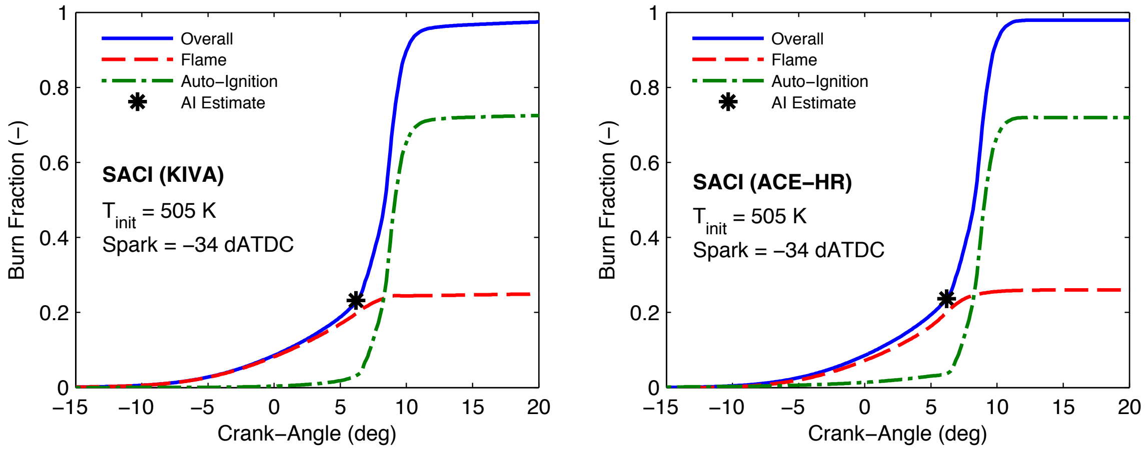

(a) (b)

Figure 3.15 – Comparison of relative flame and auto-ignition burn fractions between (a) KIVA results and (b) ACE-HR advanced combustion analysis estimate for one SACI validation case.

The end-gas reaction progress fractions (EG%) from KIVA and the ACE-HR model are compared in Figure 3.16. Very good trend-wise and absolute agreement is found between the KIVA and ACE-HR results, with a maximum error less than one-third of a crank-angle degree at EG90. These small errors can most likely be attributed to initial burn and blending assumptions.

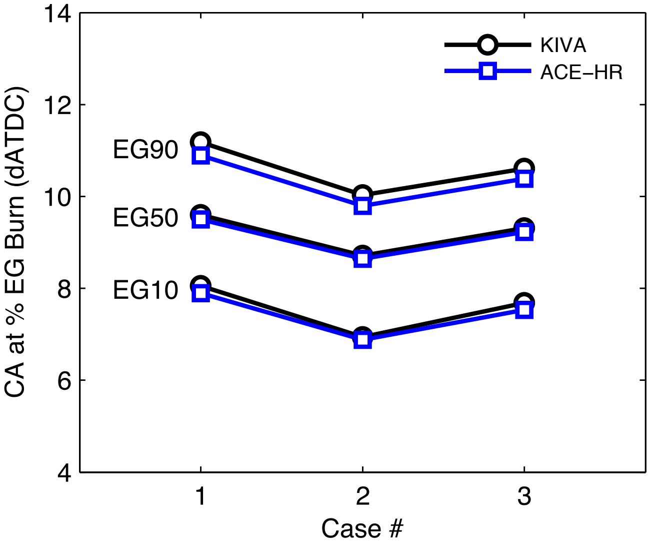

Figure 3.16 − KIVA and ACE-HR end-gas reaction progress phasing results of SACI validation cases.

Figure 3.17 compares the mean, end-gas and post-flame zone temperature estimates from the ACE-HR analysis KIVA simulations. The end-gas temperature, in particular, shows very good agreement. Errors, such as those found during the early to mid-stages of auto-ignition, are almost certainly related to the prescribed initial burn and transition assumptions. The KIVA model is also spatially resolved, where the ACE-HR model is not. So temperature gradients could be a source of discrepancy between the models.

The post-flame zone temperature, on the other hand, does show a more noticeable discrepancy, especially around the time of maximum temperature. This can probably be attributed to compounding errors in mean and end-gas state variables, together with the estimated burn rates, which are then used to define the post-flame zone. For both end-gas and post-flame zone temperatures, the average error is on the order of 1%, but it can reach more than 20% in the region where the mean temperature error is highest.

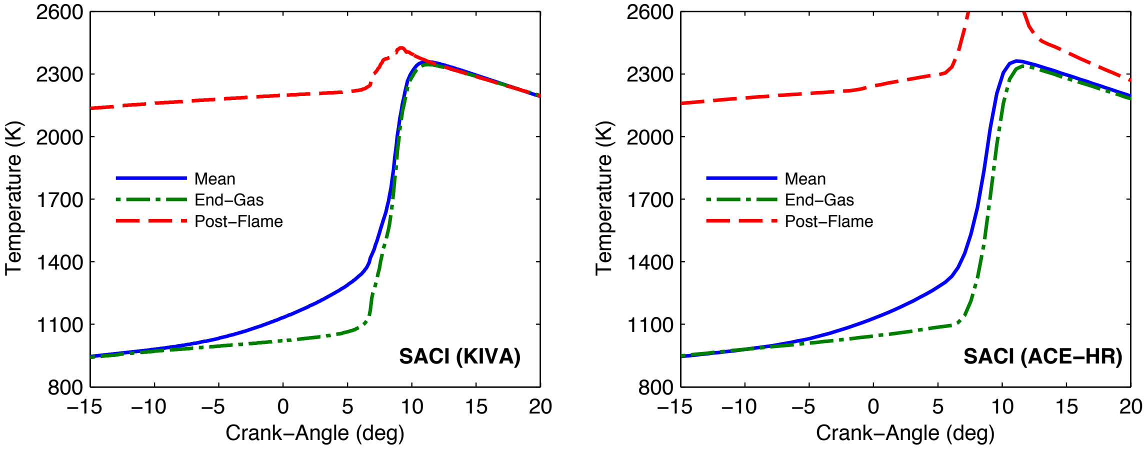

(a) (b)

Figure 3.17 − Comparison of (a) KIVA mean, end-gas and post-flame zone temperatures for a SACI validation case versus (b) ACE-HR estimates using a two-zone model with prescribed flame propagation and end-gas auto-ignition burn rates.

The end-gas temperature at spark timing $\left(T_{EG,spark}\right)$ and ignition timing $\left(T_{EG,IGN}\right)$, as well as the maximum values $\left(T_{EG,max}\right)$ are compared in Figure 3.18. All three results show excellent absolute and trend-wise agreement. The fact that $T_{EG,IGN}$ is closely estimated for all the cases means the approximation for the early heat release portion due to chemistry, as well as the ignition timing, are at least representative of the physics described by the high-fidelity model.

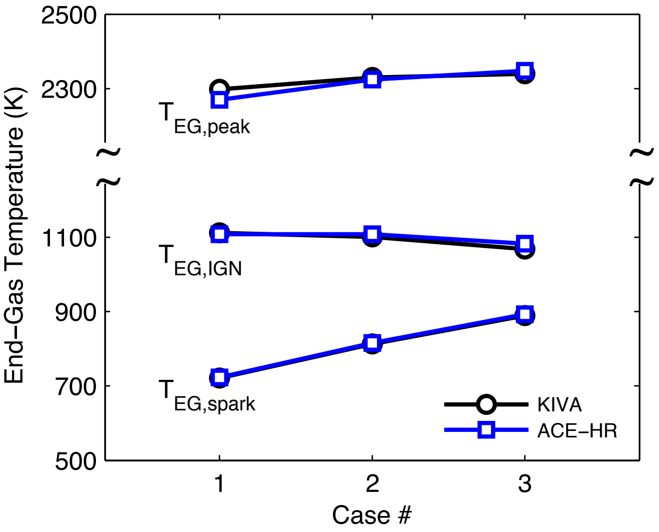

Figure 3.18 − End-gas temperature comprison between KIVA and ACE-HR predictions at times of spark- and auto-ignition for SACI validation cases. Maximum end-gas temperatures are also shown.

Laminar flame characteristics can also be estimated from the end-gas temperature and composition at any point during the flame propagation phase. Figure 3.19 shows the calculated laminar flame speed (S_L) at the times of spark and auto-ignition. These are compared with the KIVA simulation results, which were determined by averaging the values of the computational cells in the end-gas. $S_{L,spark}$ shows negligible error for all the cases, which could be expected from having almost identical end-gas temperatures. The relatively low temperature also means that no significant ignition chemistry would have occurred prior to this point. On the other hand, differences in the end-gas temperature and composition at the time of auto-ignition lead to more noticeable differences in $S_{L,IGN}$. Still, the trends are captured relatively well.

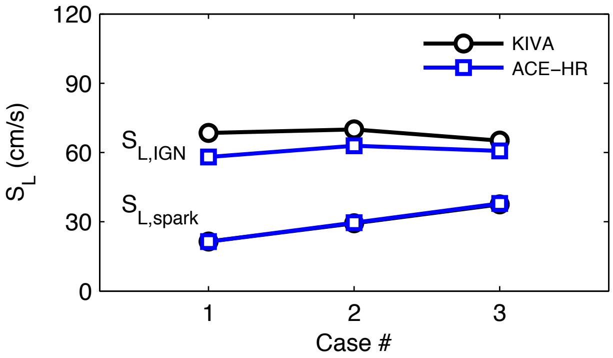

Figure 3.19 − Laminar flame speed from KIVA, averaged throughout the end-gas, compared with estimates in ACE-HR. Both KIVA and ACE-HR employ iso-octane correlations of Middleton et al. [48].

Overall, the validation results are very positive. They show that, not only can the mean heat release be calculated with a high degree of accuracy if the initial state is well defined, but also that the analysis can be extended with reasonable confidence to estimate other quantities of interest in advanced combustion engine experiments.

3.4 Sensitivity Assessment of Key Parameters

Experimental data, as well as the input data, models, and assumptions employed in the ACE-HR analysis are subject to uncertainties. In this section, a sensitivity analysis is performed on key parameters and the resulting effects on important performance and combustion-related predictions. The analysis is divided into three sub-sections. First, potential differences are quantified due to the type of ensemble analysis used. Then, errors related to engine geometry and data pre-conditioning options are assessed. Finally, the effects of uncertainties directly related to thermodynamic and combustion modeling are evaluated. Each parameter is perturbed to a high and low value from the baseline used to perform all of the analyses presented in this work. The sensitivity is reported in absolute or relative terms, according to the results in question. Only the most significant and interesting sensitivities are discussed. Two representative points for HCCI and SACI combustion were selected for the analysis, with the main operating conditions described in Table 3.5. The output parameters considered include: maximum pressure (P_{max}), net IMEP, maximum pressure-rise rate ($(dP/d\theta)_{max}$), residual gas fraction (RGF), global combustion phasing ($CA50$), global 10-90% burn duration ($BD\ 10-90\%$), maximum global temperature (T_{max}), maximum global rate of heat release ($RoHR_{max}$), ringing intensity ($R.I.$), auto-ignition timing (θ_{IGN}), end-gas temperature at auto-ignition $\left(T_{EG,IGN}\right)$, auto-ignited combustion efficiency $\left(\eta_{comb,AI}\right)$, flame burned fraction at auto-ignition $\left(x_{b,FL,IGN}\right)$, laminar flame speed at auto-ignition $\left(S_{L,IGN}\right)$, end-gas auto-ignited combustion phasing ($EG50$), maximum end-gas rate of heat release $\left(RoHR_{EG,max}\right)$ and maximum end-gas temperature $\left(T_{EG,max}\right)$.

Table 3.5 – Experimental operating conditions (average/nominal) for HCCI and SACI cases used in sensitivity assessment.

Operating Conditions	**HCCI**	**SACI**
Engine Speed (rev/min)	2000	2000
Intake Pressure (bar)	1.0	1.0
Intake Temperature (K)	368	321
Exhaust Back-Pressure (bar)	1.05	1.05
Fueling rate (mg/cycle)	9.5	19
Equivalence Ratio, Φ	0.62	1.00
External EGR (%)	0	20
NVO (deg)	157	128
Spark Timing (deg ATDC)	n/a	-34

3.4.1 Analysis Type

Many heat release analysis frameworks evaluate only the ensemble averaged pressure data. Although this is reasonable when analyzing conventional combustion regimes under stable operation, some combustion modes, such as SACI, display a large amount of cycle-to-cycle variability. Also, the mean pressure trace can obscure important cyclic events such as knock in both SI and advanced combustion regimes. ACE-HR allows for various types of ensemble analysis: average, fast cyclic (properties based on ensemble average properties) and full cyclic (cycle-by-cycle properties estimation). Moreover, the advanced two-zone analysis can also be conducted on the basis of the average heat release results, or computed cycle-by-cycle. Here we assess the sensitivity of key output results to the type of analysis used. The full cycle-by-cycle analysis is used as the standard for comparison. The cycle-by-cycle results are also averaged, but post-analysis. Table 3.6 and Table 3.7 summarize the sensitivity assessment results for the HCCI and SACI cases, respectively.

Table 3.6 – Sensitivity assessment summary of analysis type for experimental HCCI case.

Key Results	**Sensitivity Parameters**		
	Full Cyclic	**Fast Cyclic**	**Average**
$P_{max}\ [bar]$	45.41	45.41	45.25
$IMEP_{net}\ [bar]$	2.91	2.91	2.91
$(dP/d\theta)_{max}\ [bar/deg]$	3.99	3.99	3.99
$RGF\ [\%]$	46.76	46.76	46.76
$CA50\ [deg\ ATDC]$	2.68	2.67	2.67
$BD\ 10-90\%\ [deg]$	6.91	6.90	7.18
$RoHR_{max}\ [1/deg]$	0.17	0.17	0.15
$T_{max}\ [K]$	1857	1857	1853
$R.I.[MW/m^2]$	4.10	4.10	3.32
$\theta_{IGN}\ [deg]$	–2.63	–2.62	–2.90
$T_{EG,IGN}\ [K]$	1117	1117	1116
$\eta_{comb,AI}\ (\%)$	93.46	93.46	93.46

Table 3.7 – Sensitivity assessment summary of analysis type for experimental SACI case.

Key Results	**Sensitivity Parameters**		
	Full Cyclic	**Fast Cyclic**	**Average**
$P_{max}\ [bar]$	54.57	54.57	53.02
$IMEP_{net}\ [bar]$	6.18	6.18	6.18
$(dP/d\theta)_{max}\ [bar/deg]$	3.87	3.87	3.87
$RGF\ [\%]$	26.13	26.13	26.13
$CA50\ [deg\ ATDC]$	8.32	8.32	7.86
$BD\ 10-90\%\ [deg]$	16.43	16.3	17.99
$RoHR_{max}\ [1/deg]$	0.11	0.11	0.08
$T_{max}\ [K]$	2218	2220	2186
$R.I.[MW/m^2]$	3.74	3.74	1.57
$\theta_{IGN}\ [deg]$	4.34	4.34	2.80
$T_{EG,IGN}\ [K]$	1094	1094	1091
$x_{b,FL,IGN}\ [\%]$	21.01	20.90	17.10
$S_{L,IGN}\ [cm/s]$	63.62	63.62	63.45
$EG50\ [deg\ ATDC]$	9.46	9.45	9.07
$RoHR_{EG,max}\ [1/deg]$	0.15	0.15	0.10
$T_{EG,max}\ [K]$	2125	2127	2114
$\eta_{comb,AI}\ (\%)$	92.77	92.79	93.18

Results from the analysis based on the ensemble-averaged pressure data show relatively large differences in the maximum RoHR. For the HCCI case, it is close to 7%; however, for the SACI case the difference is much larger, on the order of 25%. Even larger errors were observed when comparing one of the common methods for constraining HCCI combustion, the ringing intensity (R.I.) [55], which is a function of the maximum rate of pressure-rise squared, divided by the maximum pressure. Results showed differences of ~20% and ~60% for the HCCI and SACI cases, respectively. Ignition timing and the respective results for both the mean and end-gas were also affected, but not as grossly as the rates of heat release.

The fast cyclic analysis, which uses properties for each cycle based on a preliminary mean calculation, shows minimal errors compared to the full cycle-by-cycle calculation. The difference in computational time is significant, so this type of analysis likely suffices for the majority of purposes with low computational costs.

3.4.2 Engine Geometry and Data Pre-Conditioning

The sensitivity assessment results of the engine geometry inputs and data pre-conditioning study are summarized in Table 3.8 and Table 3.9 for the HCCI and SACI cases, respectively. The base parameters and results are shown. The tables contain the relative percent change between the high/low and base values for the majority of the results, with the exception of $CA50$ and $EG50$ where the changes are given on an absolute basis.

Table 3.8 – Sensitivity assessment summary of engine geometry inputs and pressure data pre-conditioning parameters for experimental HCCI case.

Key Results (base)	**Sensitivity Parameters and Results**			
	Comp. Rat. 12.41 ± 0.25	**TDC Offset 0 deg ± 0.2**	**P_{cyl} Offset 0 kPa ± 10**	**Filter f_{cutoff} 3.5 kHz ± 1.5**
P_{max} (45.41 bar)	0.00 %	0.00 %	+0.22 % −0.22 %	+0.18 % −0.01 %
$IMEP_{net}$ (2.91 bar)	0.00 %	+3.32 % −3.32 %	0.00 %	0.00 %
$(dP/d\theta)_{max}$ (3.99 bar/deg)	0.00 %	0.00 %	0.00 %	+6.17 % −11.86 %
RGF (46.76 %)	−0.22 % +0.23 %	−0.16 % +0.13 %	+3.89 % −4.21 %	−0.06 % +0.14 %
$CA50$ (2.68 deg ATDC)	+0.19 deg −0.14 deg	+0.19 deg −0.18 deg	+0.16 deg −0.09 deg	−0.00 deg +0.03 deg
$BD\ 10-90\%$ (6.91 deg)	+15.98 % −1.02 %	+0.46 % +0.86 %	+15.06 % +2.31 %	+0.33 % +1.79 %
$RoHR_{max}$ (0.17 1/deg)	−2.25 % +0.45 %	−0.52 % +0.13 %	−2.38 % −0.84 %	+1.68 % −8.43 %
T_{max} (1857 K)	−1.73 % +1.83 %	+0.51 % −0.47 %	−3.15 % +3.45 %	+0.31 % −0.06 %
$R.I.$ (4.10 MW/m^2)	−0.91 % +0.95 %	+0.26 % −0.24 %	−1.87 % +2.00 %	+12.97 % −22.57 %
θ_{IGN} (−2.63 deg ATDC)	+2.26 deg −0.00 deg	+0.20 deg −0.19 deg	+2.01 deg −0.00 deg	+0.07 deg −0.32 deg
$T_{EG,IGN}$ (1117 K)	+2.77 % +1.99 %	+0.04 % +0.02 %	+1.05 % +3.34 %	+0.18 % −0.66 %
$\eta_{comb,AI}$ (93.46 %)	+0.01 % −0.01 %	+0.01 % −0.01 %	−0.21 % +0.21 %	+0.00 % −0.01 %

Table 3.9 – Sensitivity assessment summary of engine geometry inputs and pressure data pre-conditioning parameters for experimental SACI case.

Key Results (base)	**Sensitivity Parameters and Results**			
	Comp. Rat. 12.41 ± 0.25	**TDC Offset 0 deg ± 0.2**	**P_{cyl} Offset 0 kPa ± 10**	**Filter f_{cutoff} 3.5 kHz ± 1.5**
P_{max} (54.57 bar)	0.00 %	0.00 %	+0.37 % −0.37 %	+0.18 % −0.23 %
$IMEP_{net}$ (6.18 bar)	0.00 %	+1.62 % −1.62 %	0.00 %	−0.00 % +0.00 %
$(dP/d\theta)_{max}$ (3.87 bar/deg)	0.00 %	0.00 %	0.00 %	+10.20 % −15.23 %
RGF (26.13 %)	−0.39 % +0.41 %	−0.34 % +0.32 %	+12.02 % −13.13 %	−0.10 % +0.06 %
$CA50$ (8.32 deg ATDC)	+0.19 deg −0.19 deg	+0.17 deg −0.17 deg	+0.24 deg −0.21 deg	+0.03 deg −0.07 deg
$BD\ 10-90\%$ (16.43 deg)	+3.37 % +0.33 %	−0.90 % +1.19 %	+6.48 % +4.97 %	+1.07 % −0.50 %
$RoHR_{max}$ (0.11 1/deg)	−1.37 % +1.37 %	+0.09 % −0.12 %	−1.36 % −0.43 %	+1.47 % −7.92 %
T_{max} (2218 K)	−1.51 % +1.58 %	+0.64 % −0.62 %	−3.83 % +4.21 %	+0.32 % +0.05 %
$R.I.$ (3.74 MW/m^2)	−0.82 % +0.85 %	+0.32 % −0.31 %	−2.35 % +2.50 %	+22.59 % −29.17 %
θ_{IGN} (4.34 deg ATDC)	+0.00 deg −0.01 deg	+0.19 deg −0.20 deg	−0.01 deg +0.00 deg	+0.09 deg −0.50 deg
$T_{EG,IGN}$ (1094 K)	+0.05 % −0.04 %	+0.07 % −0.10 %	+4.07 % −7.30 %	+0.16 % −0.43 %
$x_{b,FL,IGN}$ (21.01 %)	−7.79 % +7.94 %	+1.15 % −1.27 %	−10.91 % +11.16 %	+0.95 % −8.16 %
$S_{L,IGN}$ (63.62 cm/s)	+0.53 % −0.52 %	+0.62 % −0.74 %	+11.97 % −22.90 %	+0.80 % −1.62 %
$EG50$ (9.46 deg ATDC)	+0.12 deg −0.12 deg	+0.18 deg −0.18 deg	+0.13 deg −0.08 deg	+0.03 deg −0.08 deg
$RoHR_{EG,max}$ (0.15 1/deg)	−3.57 % +3.80 %	+0.44 % −0.51 %	−4.39 % +2.80 %	+1.75 % −10.11 %
$T_{EG,max}$ (2125 K)	−1.26 % +1.35 %	+0.39 % −0.42 %	−1.42 % −0.53 %	−0.30 % +0.58 %
$\eta_{comb,AI}$ (92.77 %)	+0.18 % −0.19 %	−0.02 % +0.02 %	−0.05 % +0.06 %	−0.03 % +0.20 %

Compression Ratio

Despite the importance of compression ratio (CR) for engine performance, it is usually a very difficult parameter to measure exactly. For the sensitivity analysis, compression ratio was varied from the nominal value of 12.41 by ±0.25. Within this range, the sensitivity of most results was relatively small for both HCCI and SACI cases. The temperature estimates and heat release rate calculations saw noticeable variations, on the order of 1.5-3%. The 10-90% burn duration had the largest sensitivity, with a change of up to 16% in the HCCI. The HCCI case also showed some very asymmetrical changes, where the higher compression ratio tended to cause larger changes with respect to the baseline, compared to the low value. As an example, the peak heat release rate decrease by 2.25% for a CR = 12.41+0.25, whereas it only decreased by 0.41% for CR = 12.41–0.25. The estimate of ignition timing was affected in a similar way, where the high value resulted in a more retarded estimate by 2.25 deg, as opposed to no change for the low value. For the SACI case, however, the high and low variations resulted in relatively symmetrical sensitivity with respect to the baseline.

TDC Offset

The TDC offset accounts for the uncertainty of the crank-angle encoder used to establish the true reference TDC position in the engine. Although this is generally calibrated to zero, it is subject to drift and can cause problems when computing crank-angle dependent results such as the cylinder volume. A variation of ±0.2 deg was imposed on the TDC offset for the sensitivity analysis. The sensitivities appear relatively minor, and for many results they are also unidirectional, meaning that an increase and a decrease from the baseline produced changes in the same direction, albeit with slightly different magnitudes. Noticeable changes were observed in the IMEP calculation, up to

3%, as a result of the misaligned pressure and volume with respect to the true crank-angle.

Cylinder Pressure Referencing

Piezoelectric pressure transducers measure a relative signal that must be referenced to a known value, in this case the absolute intake pressure. Because it is not possible to truly know whether the pressures should be the same at the selected location, there will always be some uncertainty involved in this assumption. To assess the potential errors, the pressure was manually offset by ±10 kPa from the actual pegged value. Noticeable sensitivities were observed in the residual gas fraction estimates, on the order of 4% for the HCCI case and 12-13% for the SACI case, on a relative basis. On an absolute scale, the changes were similar between combustion modes, but since HCCI employs a much larger amount of internal EGR, the relative error appears lower. The temperature results were also affected, especially in the SACI case, where the end-gas temperature at auto-ignition varied up to 7%.

Filter Cutoff Frequency

The cutoff frequency used in the pressure data filter is a relatively arbitrary quantity selected based on subjective judgment. Experience has shown that for the low-pass filter used in ACE-HR, this parameter can be anywhere in the range of 2 to 5 kHz. Therefore, a baseline cutoff frequency at 3.5 kHz was selected and the frequency was varied ±1.5 kHz to assess the sensitivity of the results. The majority of the results show negligible sensitivity to the specified cutoff frequency. However, all rate-based results are highly sensitive to these changes, especially to lower cutoff frequencies. This could be particularly troublesome when assessing load limits in the experimental data. For a value of 5.0 kHz in the HCCI case, the maximum RoHR increased by ~1.5%, the maximum pressure-rise rate by 6% and the R.I. by 13%. Using 2.0 kHz, the maximum RoHR decreased by 8.5%, the maximum pressure-rise rate by 13% and the R.I. by 22.5%. The changes are significant, and can affect the selection of viable points within a specified pressure-rise rate or R.I. limit. The variations in the SACI case were on the same order.

3.4.3 System Masses, Combustion Efficiency and Heat Transfer

The results of the sensitivity assessment related to system masses and combustion efficiency are summarized in Table 3.10 and Table 3.11 for the HCCI and SACI cases, respectively. Table 3.12 and Table 3.13 contain the sensitivity assessment results for parameters involved in heat transfer estimation. The results are given on a relative percent change basis between the high/low and base values, except for $CA50$ and $EG50$, which are given on an absolute basis.

Table 3.10 – Sensitivity assessment summary of system masses and combustion efficiency for experimental HCCI case.

Key Results (base)	**Sensitivity Parameters and Results**			
	m_{fuel} Mult. 1.0 ± 0.10	**m_{air} Mult. 1.0 ± 0.10**	**RGF Mult. 1.0 ± 0.10**	**η_{comb} Mult. 1.0 ± 0.02**
RGF (46.76 %)	−5.40 % +5.95 %	−5.71 % +6.30 %	+10.01 % −10.01 %	−0.07 % +0.06 %
$CA50$ (2.68 deg ATDC)	+0.16 deg −0.05 deg	+0.19 deg −0.17 deg	+0.10 deg −0.07 deg	+0.03 deg −0.02 deg
$BD\ 10-90\%$ (6.91 deg)	+37.65 % −11.00 %	+83.42 % −28.53 %	+8.31 % −2.60 %	+4.63 % −3.89 %
$RoHR_{max}$ (0.17 1/deg)	−7.59 % +4.66 %	−7.87 % +9.00 %	−2.34 % +1.31 %	+2.00 % −1.96 %
T_{max} (1857 K)	−4.70 % +5.27 %	−4.88 % +5.45 %	−8.77 % +8.77 %	+0.02 % −0.02 %
$R.I.$ (4.10 MW/m^2)	−2.49 % +2.70 %	−2.59 % +2.81 %	−4.66 % +4.45 %	+0.02 % −0.02 %
θ_{IGN} (-2.63 deg ATDC)	−0.00 deg +1.15 deg	−0.00 deg +0.01 deg	+0.50 deg −0.01 deg	−0.00 deg +0.04 deg
$T_{EG,IGN}$ (1117 K)	−4.73 % +7.85 %	−4.92 % +5.53 %	−7.90 % +8.89 %	+0.01 % +0.08 %
$\eta_{comb,AI}$ (93.46 %)	+0.27 % −0.32 %	+0.25 % −0.30 %	−0.55 % +0.48 %	+3.58 % −3.40 %

Table 3.11 – Sensitivity assessment summary of system masses and combustion efficiency for experimental SACI case.

Key Results (base)	**Sensitivity Parameters and Results**			
	m_{fuel} Mult. 1.0 ± 0.10	**m_{air} Mult. 1.0 ± 0.10**	**RGF Mult. 1.0 ± 0.10**	**η_{comb} Mult. 1.0 ± 0.02**
RGF (26.13 %)	−8.45 % +9.70 %	−8.56 % +9.83 %	+10.01 % −10.01 %	−0.16 % +0.15 %
$CA50$ (8.32 deg ATDC)	+0.21 deg −0.17 deg	+0.23 deg −0.19 deg	+0.04 deg −0.04 deg	+0.03 deg −0.03 deg
$BD\ 10-90\%$ (16.43 deg)	+23.45 % −9.07 %	+31.28 % −10.71 %	+0.50 % −0.25 %	+2.79 % −2.41 %
$RoHR_{max}$ (0.11 1/deg)	−6.45 % +6.50 %	−6.6 % +6.82 %	−0.49 % +0.44 %	+1.89 % −1.83 %
T_{max} (2218 K)	−6.25 % +7.16 %	−6.29 % +7.22 %	−3.53 % +3.53 %	0.00 %
$R.I.$ (3.74 MW/m^2)	−3.32 % +3.66 %	−3.34 % +3.7 %	−1.84 % +1.80 %	+0.02 % −0.01 %
θ_{IGN} (4.34 deg ATDC)	+0.11 deg −0.01 deg	+0.50 deg −0.00 deg	−0.01 deg +0.00 deg	0.00 deg
$T_{EG,IGN}$ (1095 K)	−4.44 % +5.02 %	−4.36 % +5.05 %	−2.71 % +2.66 %	−0.06 % +0.05 %
$x_{b,FL,IGN}$ (21.01 %)	−0.14 % +1.69 %	+9.64 % +2.27 %	−2.23 % +1.92 %	+3.79 % −3.84 %
$S_{L,IGN}$ (63.62 cm/s)	−14.58 % +19.71 %	−14.32 % +19.52 %	−19.50 % +22.55 %	−4.98 % +4.93 %
$EG50$ (9.46 deg ATDC)	+0.37 deg −0.21 deg	+0.95 deg −0.22 deg	+0.02 deg −0.03 deg	+0.05 deg −0.05 deg
$RoHR_{EG,max}$ (0.15 1/deg)	−7.87 % +7.35 %	−9.72 % +7.87 %	−1.15 % +1.03 %	+3.13 % −3.01 %
$T_{EG,max}$ (2125 K)	−4.05 % +3.65 %	−5.14 % +3.85 %	−3.07 % +3.06 %	+0.58 % −0.59 %
$\eta_{comb,AI}$ (92.77 %)	+0.08 % −0.30 %	−0.77 % −0.31 %	−0.19 % +0.19 %	+4.36 % −4.10 %

Table 3.12 – Sensitivity assessment summary of heat transfer parameters for experimental HCCI case.

Key Results (base)	**Sensitivity Parameters and Results**			
	H.T. Mult. 1.0 ± 0.40	**T_{head} 400 K ± 50**	**T_{piston} 400 K ± 50**	**T_{liner} 400 K ± 50**
RGF (46.76 %)	0.00 %	−0.01 % +0.01 %	0.00 %	−0.04 % +0.04 %
$CA50$ (2.68 deg ATDC)	0.00 deg	+0.01 deg −0.00 deg	0.00 deg	0.0 deg
$BD\ 10-90\%$ (6.91 deg)	+0.03 % −0.02 %	+0.16 % −0.15 %	+0.11 % −0.10 %	+0.43 % −0.40 %
$RoHR_{max}$ (0.17 1/deg)	−0.01 % +0.01 %	−0.03 % +0.03 %	−0.02 % +0.02 %	−0.16 % +0.16 %
T_{max} (1857 K)	0.00 %	+0.01 % −0.01 %	0.00 %	+0.04 % −0.03 %
$R.I.$ (4.10 MW/m^2)	0.00 %	0.00 %	0.00 %	+0.02 % −0.02 %
θ_{IGN} (-2.63 deg ATDC)	0.00 deg	−0.00 deg +0.01 deg	−0.00 deg +0.01 deg	−0.00 deg +0.01 deg
$T_{EG,IGN}$ (1117 K)	0.00 %	+0.01 % +0.03 %	−0.00 % +0.03 %	+0.04 % −0.00 %
$\eta_{comb,AI}$ (93.46 %)	0.00 %	0.00 %	0.00 %	0.00 %

Table 3.13 – Sensitivity assessment summary of heat transfer parameters for experimental SACI case.

Key Results (base)	**Sensitivity Parameters and Results**			
	H.T. Mult. **1.0** **± 0.40**	T_{head} **400 K** **± 50**	T_{piston} **400 K** **± 50**	T_{liner} **400 K** **± 50**
RGF (26.13 %)	0.00 %	−0.01 % +0.00 %	0.00 %	−0.06 % +0.06 %
$CA50$ (8.32 deg ATDC)	0.00 deg	+0.01 deg −0.01 deg	0.00 deg	0.00 deg
$BD\ 10-90\%$ (16.43 deg)	+0.02 % −0.02 %	−0.06 % +0.06 %	−0.04 % +0.04 %	+0.10 % −0.09 %
$RoHR_{max}$ (0.11 1/deg)	−0.02 % +0.02 %	+0.01 % −0.01 %	+0.01 % −0.01 %	−0.07 % +0.07 %
T_{max} (2218 K)	0.00 %	0.00 %	0.00 %	+0.02 % −0.02 %
$R.I.$ (3.74 MW/m^2)	0.00 %	0.00 %	0.00 %	+0.01 % −0.01 %
θ_{IGN} (4.34 deg ATDC)	0.00 deg	0.00 deg	0.00 deg	0.00 deg
$T_{EG,IGN}$ (1094 K)	−1.86 % +1.84 %	+0.28 % −0.28 %	+0.19 % −0.19 %	+0.20 % −0.20 %
$x_{b,FL,IGN}$ (21.01 %)	+0.13 % −0.13 %	−0.32 % +0.31 %	−0.21 % +0.21 %	−0.04 % +0.04 %
$S_{L,IGN}$ (63.62 cm/s)	−8.90 % +9.57 %	+1.41 % −1.40 %	+0.96 % −0.96 %	+1.03 % −1.02 %
$EG50$ (9.46 deg ATDC)	0.00 deg	0.00 deg	0.00 deg	0.00 deg
$RoHR_{EG,max}$ (0.15 1/deg)	+0.02 % −0.02 %	−0.08 % +0.08 %	−0.05 % +0.05 %	−0.08 % +0.08 %
$T_{EG,max}$ (2125 K)	−1.37 % +1.37 %	+0.13 % −0.13 %	+0.09 % −0.09 %	+0.08 % −0.08 %
$\eta_{comb,AI}$ (92.77 %)	0.00 %	+0.01 % −0.01 %	0.00 %	0.00 %

System Masses (Fuel, Air and Residual)

Within typical experimental engine setups, it is not possible to measure in-cylinder mass and composition, so models and simplifying assumptions are usually necessary to obtain reasonable estimates. Fuel flow and air flow are commonly metered, but the accuracy can vary significantly depending on the measurement approach. On the other hand, residual mass is very difficult to measure at any level of accuracy, so the burden of modeling and related uncertainty falls on this estimate. It becomes especially important when employing residual trapping strategies for HCCI combustion control. To assess the sensitivity of the various mass quantities, the fuel mass, air mass, residual gas fraction (RGF) and total mass have been independently varied by ±10% using a direct multiplier on the measured value or baseline estimate.

The sensitivity to mass is significant for most of the important results. For the fuel mass sensitivity study, the trapped residual mass estimate changes by ~5% in the HCCI case and ~9% on the SACI case. This mass error is then reflected in all the temperatures, with maximum values changing by 5-7% in both instances. The higher fuel mass also causes changes in the 10-90% burn duration that are on the order of 3-4 deg, which translates to relative variations of up to 80%; CA50 was only minimally affected. This result indicates the shape of the burn curve is more sensitive to the early and later combustion phases, partly due to the change in energy balance. The mean RoHR results varied by 7-9%; however, the local end-gas reaction rate close to the maximum in the SACI case revealed slightly larger errors, close to 10%. The sensitivity to the air mass was similar, since the fuel is derived from the air measurement. When varying the internal residual gas fraction, slightly larger errors were observed, as a result of applying the multiplier to the residual gas fraction, not the residual mass, and the observed trends were the same.

Combustion Efficiency

Combustion efficiency is commonly calculated from emissions measurements in the exhaust. Errors in combustion efficiency affect the system energy balance for heat release analysis, and potentially the assumed composition for properties estimation. To assess the sensitivity due to uncertainties in the data acquisition system, the combustion efficiency was varied ±2% from the estimated baseline. Overall, the sensitivity to the combustion efficiency within this range was minor. The peak RoHR showed changes of around 2% for both HCCI and SACI cases. In the latter, the calculated auto-ignition combustion efficiency $(\eta_{comb,AI})$ and burn fraction by flame at ignition $(x_{b,FL,IGN})$ were slightly more affected, and the ~4% variations observed are a direct result of the combustion efficiency applied to the burn fraction calculation.

Heat Transfer

As shown in Section 3.3.2, the selection of heat transfer model can have a very significant impact on certain results derived from the heat release analysis. Detailed assessments of these variations have been the subject other studies. Here we apply a straightforward approach consistent with the rest of the sensitivity analysis, where the calculated heat transfer coefficient obtained from the proposed Woschni-ACE correlation is directly increased and decreased 40% by way of a multiplier. This type of heat transfer variation did not seem to affect the majority of results in a significant way, with the exception of certain estimates based on the two-zone model in the SACI case. The end-gas temperature at ignition showed a change close to 2%.

Wall Temperature

The wall temperature must be specified for the heat transfer calculation. Some dedicated heat transfer studies have been able to measure average surface temperatures in the engine, but most setups do not have this capability. Thus, for heat release analysis, these are typically specified based on the expected operating conditions and previous experimental work. For the present analysis, uniform wall temperatures of 400 K were assumed for the baseline condition of both the HCCI and SACI cases. The wall temperature for each region (head, piston and liner) was then varied independently over the relatively large range of ±50 K. The impact was for the most part negligible for the three wall temperature variations. The largest change was of 1% on the laminar flame speed at ignition $\left(S_{L,IGN}\right)$ in the SACI case.

3.5 References

[1] J. A. Gatowski, E. N. Balles, K. M. Chun, F. E. Nelson, J. A. Ekchian, and J. B. Heywood, “Heat release analysis of engine pressure data,” *SAE 841359*, 1984.

[2] M. F. J. Brunt, H. Rai, and A. L. Emtage, “The Calculation of Heat Release Energy from Engine Cylinder Pressure Data,” *SAE 981052*, 1998.

[3] Y. G. Guezennec and W. Hamama, “Two-Zone Heat Release Analysis of Combustion Data and Calibration of Heat Transfer Correlation in an I. C. Engine,” *SAE 1999-01-0218*, 1999.

[4] A. E. Catania, D. Misul, A. Mittica, and E. Spessa, “Unsteady Convection Model for Heat Release Analysis of IC Engine Pressure Data,” *SAE 2000-01-1265*, 2000.

[5] A. E. Catania, D. Misul, A. Mittica, and E. Spessa, “A Refined Two-Zone Heat Release Model for Combustion Analysis in SI Engines,” *JSME International Journal*, vol. 46, no. 1, 2003.

[6] A. Kulzer, D. Lejsek, A. Kiefer, and A. Hettinger, “Pressure Trace Analysis Methods to Analyze Combustion Features and Cyclic Variability of Different Gasoline Combustion Concepts,” *SAE 2009-02-0501*, 2009.

[7] M. Fathi, R. K. Saray, and M. D. Checkel, “Detailed approach for apparent heat release analysis in HCCI engines,” *Fuel*, vol. 89, no. 9, pp. 2323–2330, 2010.

[8] M. Baratta and D. Misul, “Development and assessment of a new methodology for end of combustion detection and its application to cycle resolved heat release analysis in IC engines,” *Applied Energy*, vol. 98, pp. 174–189, 2012.

[9] R. Egnell, “Combustion Diagnostics by Means of Multizone Heat Release Analysis and NO Calculation,” *SAE 981424*, 1998.

[10] G. M. Rassweiler and L. Withrow, “Motion Pictures of Engine Flames Correlated with Pressure Cards,” *SAE Transactions*, vol. 42, 1938.

[11] J. B. Heywood, *Internal Combustion Engine Fundamentals*. McGraw-Hill, Inc., 1988.

[12] R. Lanzafame and M. Messina, “ICE GROSS HEAT RELEASE STRONGLY INFLUENCED BY SPECIFIC HEAT RATIO VALUES,” *International Journal of Automotive Technology*, vol. 4, no. 3, pp. 135–133, 2003.

[13] M. Klein and L. Eriksson, “A specific heat ratio model for single-zone heat release models,” *SAE 2004-01-1464*, 2004.

[14] M. A. Ceviz and İ. Kaymaz, “Temperature and air–fuel ratio dependent specific heat ratio functions for lean burned and unburned mixture,” *Energy Conversion and Management*, vol. 46, no. 15, pp. 2387–2404, 2005.

[15] “NIST-JANAF Thermochemical Tables.” http://kinetics.nist.gov/janaf/.

[16] A. Burcat, “Prof. Burcat's Thermodynamic Data.” http://garfield.chem.elte.hu/Burcat/burcat.html.

[17] R. J. Kee, F. M. Rupley, E. Meeks, and J. A. Miller, “CHEMKIN-III: A FORTRAN CHEMICAL KINETICS PACKAGE FOR THE ANALYSIS OF GAS-PHASE AND PLASMA KINETICS,” Sandia National Laboratories, 1996.

[18] C. Depcik, T. Jacobs, J. Hagena, and D. Assanis, “Instructional use of a single-zone, premixed charge, spark-ignition engine heat release simulation,”

International Journal of Mechanical Engineering Education, vol. 35, no. 1, pp. 1–31, 2007.

[19] C. Olikara and G. L. Borman, "A COMPUTER PROGRAM FOR CALCULATING PROPERTIES OF EQUILIBRIUM COMBUSTION PRODUCTS WITH SOME APPLICATIONS TO I.C. ENGINES," *SAE 750468*, 1975.

[20] J. Brettschneider, "Berechnung des luftverhaeltnisses lambda von luft-kraftstoff gemischen und des einflusses von messfehlern auf lambda," Robert Bosch GMB, 1979.

[21] L. Manofsky, J. Vavra, D. Assanis, and A. Babajimopoulos, "Bridging the Gap between HCCI and SI: Spark-Assisted Compression Ignition," *SAE 2011-01-1179*, 2011.

[22] D. A. Rothamer, J. A. Snyder, R. K. Hanson, R. R. Steeper, and R. P. Fitzgerald, "Simultaneous imaging of exhaust gas residuals and temperature during HCCI combustion," *Proceedings of the Combustion Institute*, vol. 32, no. 2, pp. 2869–2876, 2009.

[23] R. G. Prucka, Z. S. Filipi, and D. N. Assanis, "An Evaluation of Residual Gas Fraction Measurement Techniques in a High Degree of Freedom Spark Ignition Engine," *SAE 2008-01-0094*, 2008.

[24] GTI, "GT-SUITE Engine Performance Application Manual," Gamma Technologies, 2010.

[25] E. A. Ortiz-Soto, J. Vavra, and A. Babajimopoulos, "Assessment of Residual Mass Estimation Methods for Cylinder Pressure Heat Release Analysis of HCCI Engines With Negative Valve Overlap," *Journal of Engineering for Gas Turbines and Power*, vol. 134, no. 8, 2012.

[26] H. J. Yun and W. Mirsky, "Schlieren-Streak Measurements of Instantaneous Exhaust Gas Velocities from a Spark-Ignition Engine," *SAE 741015*, 1974.

[27] R. P. Fitzgerald, R. R. Steeper, J. A. Snyder, R. K. Hanson, and R. P. Hessel, "Determination of Cycle Temperatures and Residual Gas Fraction for HCCI NVO Operation," *SAE 2010-01-0343*, 2010.

[28] D. L. Stivender, "Development of a Fuel-Based Mass Emission Measurement Procedure," *SAE 710604*, 1971.

[29] K. Chang, "MODELING AND ANALYSIS OF AN HCCI ENGINE DURING THERMAL TRANSIENTS USING A THERMODYNAMIC CYCLE SIMULATION WITH A COUPLED WALL THERMAL NETWORK," Ph. D. Thesis, University of Michigan, 2010.

[30] G. Woschni, "A Universally Applicable Equation for the Instantaneous Heat Transfer Coefficient in the Internal Combustion Engine," *SAE 670931*, 1967.

[31] J. Chang, O. Guralp, Z. Filipi, D. Assanis, T.-W. Kuo, P. Najt, and R. Rask, "New Heat Transfer Correlation for an HCCI Engine Derived from Measurements of Instantaneous Surface Heat Flux," *SAE 2004-01-2996*, 2004.

[32] G. F. Hohenberg, "Advanced Approaches for Heat Transfer Calculations," *SAE 790825*, 1979.

[33] G. Eichelberg, "Some New Investigations on Old Combustion Engine Problems," *Engineering*, vol. 148, pp. 463–466 and 547–550, 1939.

[34] T. Suzuki, Y. Oguri, and M. Yoshida, “Heat Transfer in the Internal Combustion Engine,” *SAE 2000-01-0300*, 2000.
[35] S. Hajireza and B. Sunden, “Prediction of Heat Transfer to the Walls for Autoignition Related Situations in SI Engines,” *SAE 2000-01-1084*, 2000.
[36] B. Grandin and D. N. Assanis, “The Effect of Knock on Heat Transfer in SI Engines,” *SAE 2002-01-0238*, 2002.
[37] T. Tsurushima, E. Kunishima, Y. Asaumi, Y. Aoyagi, and Y. Enomoto, “The Effect of Knock on Heat Loss in Homogeneous Charge Compression Ignition Engines,” *SAE 2002-01-0108*, 2002.
[38] A. Sharief and T. K. Chandrashekar, “Study on Heat Transfer Correlation in IC Engines,” *SAE 2008-01-1816*, 2008.
[39] R. T. M. Junior and C. R. P. Belchior, “Analysis of Different Correlations for Heat Transfer to the Cylinder Wall in Spark-Ignition Engines with a Generalized Computational Algorithm,” *SAE 2008-36-0187*, 2008.
[40] S. Hensel, F. Sarikoc, F. Schumann, H. Kubach, and U. Spicher, “Investigation on the Heat Transfer in HCCI Gasoline Engines,” *SAE 2009-01-1804*, 2009.
[41] S. Hensel, F. Sarikoc, F. Schumann, H. Kubach, A. Velji, and U. Spicher, “A New Model to Describe the Heat Transfer in HCCI Gasoline Engines,” *SAE 2009-01-0129*, 2009.
[42] J. A. Caton, “Comparisons of Global Heat Transfer Correlations for Conventional and High Efficiency Reciprocating Engines,” presented at the ASME 2011 Internal Combustion Engine Division Fall Technical Conference, ICEF2001-60017, 2011.
[43] N. P. Komninos and G. M. Kosmadakis, “Heat transfer in HCCI multi-zone modeling: Validation of a new wall heat flux correlation under motoring conditions,” *Applied Energy*, vol. 88, no. 5, pp. 1635–1648, 2011.
[44] M. S. Lounici, K. Loubar, M. Balistrou, and M. Tazerout, “Investigation on heat transfer evaluation for a more efficient two-zone combustion model in the case of natural gas SI engines,” *Applied Thermal Engineering*, vol. 31, no. 2, pp. 319–328, 2011.
[45] H. Persson, A. Hultqvist, and B. Johansson, “Investigation of the Early Flame Development in Spark Assisted HCCI Combustion Using High Speed Chemiluminescence Imaging,” *SAE 2007-01-0212*, 2007.
[46] J. B. Martz, G. A. Lavoie, H. G. Im, R. J. Middleton, A. Babajimopoulos, and D. N. Assanis, “The propagation of a laminar reaction front during end-gas auto-ignition,” *Combustion and Flame*, vol. 159, no. 6, pp. 2077–2086, 2012.
[47] J. B. Martz, “SIMULATION AND MODEL DEVELOPMENT FOR AUTO-IGNITION AND REACTION FRONT PROPAGATION IN LOW-TEMPERATURE HIGH-PRESSURE LEAN-BURN ENGINES,” Ph. D. Thesis, University of Michigan, 2010.
[48] R. J. Middleton, J. B. Martz, G. A. Lavoie, A. Babajimopoulos, and D. N. Assanis, “A computational study and correlation of premixed isooctane air laminar reaction fronts diluted with EGR,” *Combustion and Flame*, vol. 159, no. 10, pp. 3146–3157, 2012.
[49] A. L. Randolph, “Methods of Processing Cylinder-Pressure Transducer Signals

to Maximize Data Accuracy," *SAE 900170*, 1990.

[50] M. F. J. Brunt and C. R. Pond, "Evaluation of Techniques for Absolute Cylinder Pressure Correction," *SAE 970036*, 1997.

[51] A. Babajimopoulos, D. N. Assanis, D. L. Flowers, S. M. Aceves, and R. P. Hessel, "A fully coupled computational fluid dynamics and multi-zone model with detailed chemical kinetics for the simulation of premixed charge compression ignition engines," *International Journal of Engine Research*, vol. 6, no. 5, pp. 497–512, 2006.

[52] B. P. Vanzieleghem, "COMBUSTION MODELING FOR GASOLINE DIRECT INJECTION ENGINES USING KIVA-3V," Ph. D. Thesis, University of Michigan, 2004.

[53] Y. F. Tham, F. Bisetti, and J.-Y. Chen, "Development of a Highly Reduced Mechanism for Iso-Octane HCCI Combustion With Targeted Search Algorithm," *Journal of Engineering for Gas Turbines and Power*, vol. 130, no. 4, pp. 042804–042807, 2008.

[54] J. B. Martz and R. J. Middleton, "KIVA CFMZ Paper," *In preparation*.

[55] J. A. Eng, "Characterization of Pressure Waves in HCCI Combustion," *SAE 2002-01-2859*, 2002.

CHAPTER 4

EMPIRICAL AUTO-IGNITION BURN RATE MODEL FOR SACI COMBUSTION

The present chapter addresses the end-gas auto-ignition burn rate model for SACI combustion, considered one of the most critical components of the framework developed for this work. The model is consistent with the physical assumptions of the proposed reduced order thermodynamic SACI model, and uses experimental results provided by the ACE-HR heat release analysis tool developed for this work to formulate and validate the model. The development of the auto-ignition modeling within the general SACI combustion modeling framework is conceptually shown in Figure 4.1.

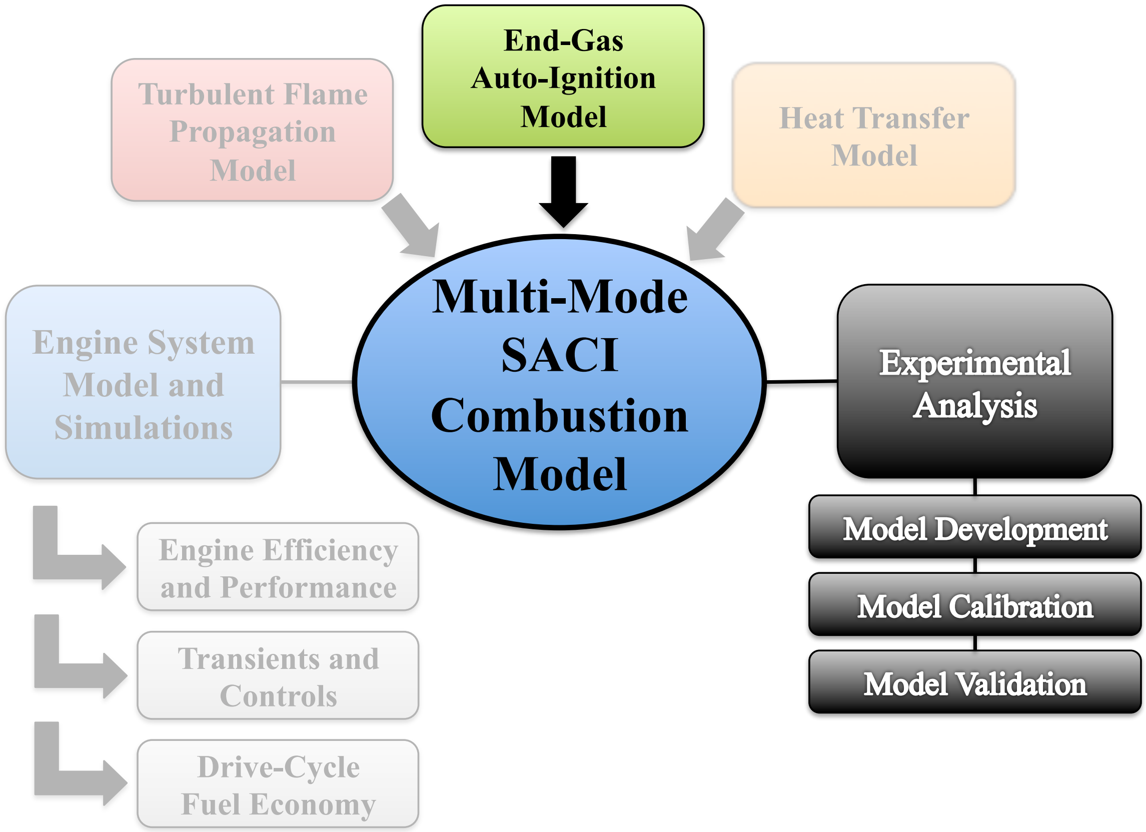

Figure 4.1 – General research framework for experimental analysis, model development and simulation of advanced SACI combustion engines. The end-gas auto-ignition model is a critical component of the SACI combustion modeling framework and uses the ACE-HR experimental analysis in this work for development and validation.

4.1 Auto-Ignition Combustion Modeling: Review

It is generally accepted that both HCCI combustion and SI end-gas knock are combustion events driven by auto-ignition predominantly controlled by chemical kinetics, as opposed to mixing as in Diesel engines. Therefore, the incorporation of chemistry is essential to obtain realistic performance predictions of engines employing SI, HCCI and SACI combustion. Simulations of varying degrees of complexity have been developed to understand the coupled effects of chemistry, thermodynamics and gas-exchange within these engines. These have ranged from CFD with detailed chemistry, to zero-dimensional models with simple ignition and empirical burn-rate correlations. We presently focus our review on existing auto-ignition modeling approaches in the context of reduced order simulations, consistent with the motivations and objectives of this work.

4.1.1 Ignition Delay Integral

The auto-ignition integral approach, originally proposed by Livengood and Wu [1], has been widely used SI knock and HCCI combustion models because of its simplicity and minimal computational cost. The expression for ignition delay, τ, is typically given in Arrhenius form. Occurrence of ignition, t_{IGN}, is defined as the time when the auto-ignition integral reaches the value of 1:

$$\int_{t_0}^{t_{IGN}} \frac{1}{\tau} dt = 1 \tag{4.1}$$

Many ignition delay correlations for τ have been published over the years for a wide range of fuels and conditions [2]-[4]. Since the integration merely provides a threshold value, this approach is mainly used to estimate the global onset of ignition or knock [5]-[7], where sometimes the simulations assume the rest of the end-gas burns instantaneously. Lawler et al. [8] also developed an experimental post-processing methodology incorporating the ignition delay integral into a multi-zone model to evaluate stratification in HCCI engines. However, burn rate predictions within engine simulations using an approach for predominantly auto-igniting conditions, such as in HCCI and SACI combustion, are generally not possible. The empirical nature of these correlations can also limit the range and utility when investigating new combustion regimes, where large extrapolations would be necessary.

4.1.2 Single- and Multi-Zone Chemical Kinetics

Reduced order zonal models with detailed chemical kinetics have demonstrated the potential for more general predictability of auto-ignition. These have been applied with varying degrees of complexity in chemical kinetics to model both SI knock [9], [10] and HCCI combustion [11], [12]. Lower zonal models, such as single-zone HCCI or two-zone SI, appear to provide suitable estimates of ignition timing, but realistic burn rates from auto-ignition can only be captured by higher zonal models with temperature or compositional gradients representative of experimental engine conditions. However, these models tend to be very sensitive to the number of zones employed and still require extensive calibration to be able to approximate these gradients.

The chemistry employed can also be an important source of uncertainty. Detailed oxidation mechanisms for practical fuels, such as iso-octane [13], deliver the most accurate chemistry, but they are usually too computationally expensive due to the large number of species and reactions involved. Derived skeletal mechanisms [14] can be significantly faster, but their accuracy and valid range of applicability can be limited. The Nissan PRF mechanism for HCCI combustion [15] is an example of more extreme mechanism reduction strategies for specific combustion modes, with the number of species in the dozens, instead of hundreds. Similarly, the well-known “Shell” model [16] has been extensively used for knock modeling [9] and is based on a reduced set of general reactions instead of actual chemical species.

4.1.3 Empirical Burn Rate Modeling

As a compromise between modeling complexity and accuracy, researchers at the University of Michigan developed an empirical burn rate model to fit a standard Wiebe function, with parameters obtained through correlations for 0-50% and 0-90% burn intervals, peak temperature and combustion efficiency [17]. Unfortunately, the model was never formally published, so a thorough derivation and experimental validation are not available. Moreover, the functional form is not optimal, since it allows for the possibility of the 0-50% correlation to “step over” the 0-90% correlation under limiting conditions, which is obviously non-physical and breaks down any resulting predictions.

The model was fitted solely to simulation results from parametric studies of HCCI combustion using the coupled CFD/Multi-Zone modeling approach of Babajimopoulos et al. [18], introducing an additional level of uncertainty. The correlated points encompassed typical naturally aspirated HCCI conditions, so potential effects resulting from near stoichiometric equivalence ratios, internal residual trapping, intake charge boosting and spark-assisted operation were not considered. On the other hand, the model has been shown capable of capturing the knock and stability constrained HCCI operating regime consistent with experimental results, with a low enough computational cost to allow for large parametric and engine mapping studies [5]. These potential benefits over alternative approaches motivated the present development of a more general model that could incorporate experimental data, a larger range of conditions and SACI combustion.

4.2 Empirical SACI Auto-Ignition Burn Rate Model

The burn rate model for auto-ignited combustion developed in this work builds upon the approach presented in [17] described in the previous section. The new model accounts for boosted conditions and spark-assisted operation. It is primarily based on experimental data, whereas the previous model was solely based on reduction of simulation results from the KIVA Multi-Zone (KMZ) framework [18].

Conceptually, auto-ignited combustion in an engine is typically modeled as an ignition cascade process. This model assumes that after the end of piston compression, the hotter zones ignite first and expand, heating adjacent zones to the point of ignition as by increasing the internal energy from compression work transfer. This process continues until the reactants are fully consumed or until piston expansion cools the mixture enough to inhibit auto-ignition. Therefore, both chemical and transport phenomena play a role in determining the burn rate of auto-ignited combustion. Composition and chemistry determine the rate at which each virtual element burns, as well as their final thermodynamic state. Fluid dynamics, transport properties and heat transfer establish the gradients through which the ignition cascade proceeds. Moreover, due to the reciprocating nature of engines, the temporal location of the combustion event and the engine rotational speed must also be considered.

Chemical effects are typically determined from fundamental combustion studies, such as shock tube and rapid compression machine experiments, or simple constant volume/pressure reactor simulations. From ignition delay studies and correlation, such as the one presented in [3], we can infer that the main chemical effects are captured by fuel-oxygen composition, inert diluent content, pressure and temperature. In the present work, the fuel-oxygen equivalence ratio (φ) is employed to capture the fuel-oxygen composition or fuel energy potential. φ is computed by an atomic balance for carbon (C), hydrogen (C) and oxygen (O) in the unreacted mixture, as shown in Equation (4.2). Any carbon or hydrogen present at CO_2 or H_2O in the charge (e.g. via EGR) is not included in the determination of φ. Although this formulation is only valid for non-oxygenated fuels, it can be easily modified to account for the additional oxygen content [18].

$$\varphi = \frac{2C^{\#}_{-CO_2} + \frac{1}{2}H^{\#}_{-H_2O}}{O^{\#}_{-CO_2-H_2O}} \tag{4.2}$$

The effect of residual gas diluents is captured by the mole fraction of stoichiometric combustion products (X_{SCP}), an approach initially presented in [19]. X_{SCP} is computed based on stoichiometry, assuming complete combustion products CO_2, H_2O and N_2, where x and y are the number of carbon and hydrogen atoms in the fuel:

$$X_{SCP} = X_{CO_2} + X_{H_2O} + X_{N_{2,st}} = \left[1 + \frac{y}{2x} + \left(x + \frac{y}{4}\right)\frac{3.76}{x}\right] X_{CO_2} \tag{4.3}$$

Finally, it is assumed that the effects of pressure and temperature can be captured by the respective mean values at the estimated point of ignition, P_{IGN} and $T_{EG,IGN}$. The use of the end-gas temperature T_{EG} instead of the global mean temperature follows the conceptual SACI two-zone model described in Section 2.2, where auto-ignition chemistry is assumed to take place only in the end-gas zone.

Practical engine applications introduce a series of complexities not found in standard combustion testing equipment such as constant volume bombs, shock tubes and rapid compression machines. The rotational speed, for example, changes the time scales available for chemistry, with respect to the geometrical coordinate of the piston position. More specifically, as engine speed increases, combustion will take a relatively longer time in crank-angle degrees, which can be detrimental for efficiency and combustion quality. This issue is particularly critical for chemistry-driven combustion, compared to turbulent flame propagation. High engine speeds also incur higher turbulence levels. Turbulent combustion scales relatively well with engine speed such that it is possible to run spark-ignition engines up to 6000 rev/min and higher. Auto-ignition combustion is presumably much less dependent on turbulence and much more dependent on chemical kinetic rates. Thus, if the proper thermal state cannot be attained in order to ignite the mixture early enough, the viable range in terms of engine speed will be much more limited. This is supported by the HCCI correlation work [17], where the authors determined engine speed (RPM) contributed significantly to burn rate variations.

Another important phenomenon observed in engines is the effect of compositional and thermal stratification. Recently, based on high-fidelity computational studies, [20] demonstrated that use of residual-trapping strategies such as NVO to achieve auto-ignition temperatures introduced significant thermal and compositional stratification, which contributed to increases in burn duration up to 30% compared with PVO strategies with intake pre-heating. However, for a zero-dimensional simulation such as the one employed in the present work the lack of spatial resolution precludes any accurate determination of in-cylinder gradients. Therefore, to estimate these effects, we propose an empirical lumped stratification or unmixedness factor, f_{unmix}. It is assumed that for a binary mixture, in this case composed of the intake charge and the trapped residuals, the maximum level of unmixedness occurs when equal amounts of each component is present. If we arbitrarily select the trapped residuals as the quantity being tracked, then this amount is given by the internal EGR fraction, $iEGR$. Therefore, f_{unmix} peaks at $iEGR = 50\%$ and goes to zero when $iEGR = 0\%$ or $iEGR = 100\%$. Selecting a quadratic profile for f_{unmix} as a function of $iEGR$, we obtain the following expression:

$$f_{unmix}(iEGR) = 4(1 - iEGR)iEGR \tag{4.4}$$

where f_{unmix} has a maximum of unity at $iEGR = 50\%$. The unmixedness function is plotted in Figure 4.2.

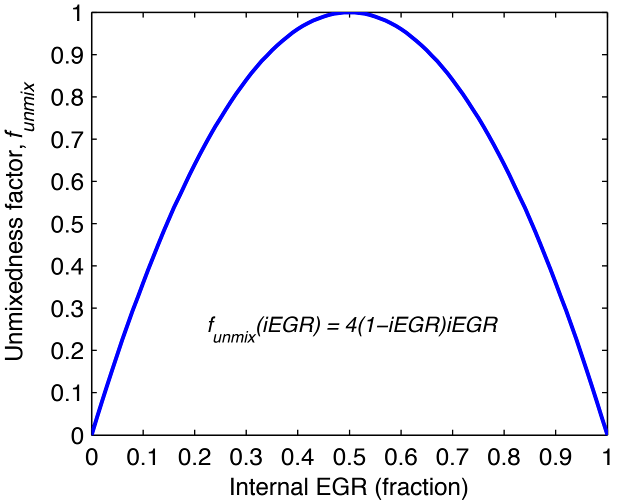

Figure 4.2 – Proposed unmixedness factor as a function of internal EGR fraction.

Even though the true nature of the stratification is much more complex, and depends on bulk flow, turbulence, transport properties, molecular diffusion and heat transfer, this simple function is consistent with the present zero-dimensional approach and is considered sufficient for the purposes of system-level engine studies. Other approaches, such as a multi-zone "balloon" model [20], have also been employed in this type of framework, but they are much more computationally expensive and still require empirical tuning factors to properly model the thermal gradients.

The last key component of the model relates to spark-assisted operation. Experimental SACI studies have shown that it is possible to modulate the burn rate at constant combustion phasing using varying levels of spark-assist and pre-compression temperatures [21]. Lowering the temperature and advancing the spark resulted in a higher proportion of flame propagation, as well as a decrease in peak rate of heat release (RoHR). The reason provided by the authors was that by consuming more of the charge by slow deflagrative flame propagation, less fuel energy was available to be released under rapid auto-ignition. This effect, however, would not require any further modifications to the current empirical model, since it would be inherently captured by the solution of the thermodynamic system during the simulation. On the other hand, recent computational studies [22] have shown that flame propagation can actually alter the compositional and thermal gradients, as seen by the potentially auto-igniting mixture. For a centrally mounted spark plug, the flame will proceed with an approximately spherical geometry, thus consuming the central core region first, which is also generally the hottest part of the mixture where the auto-ignition cascade will initiate. By effectively removing part of this region, not only will auto-ignition be delayed until flame compression brings the end-gas up to igniting temperature, but also the proportion of the end-gas closer to the wall will be higher, resulting in an overall steeper gradient and a slower burn.

This effect can be estimated by applying the SACI two-zone model to experimental data presented in [21] using ACE-HR (see CHAPTER 3). Figure 4.3(a) shows the relatively constant phasing of combustion, both in the auto-ignition event (CA-IGN) and CA50, despite the significant decrease in global peak RoHR seen in Figure 4.3(b). This effect is highly desirable, since it is one of the key mechanisms for SACI load expansion.

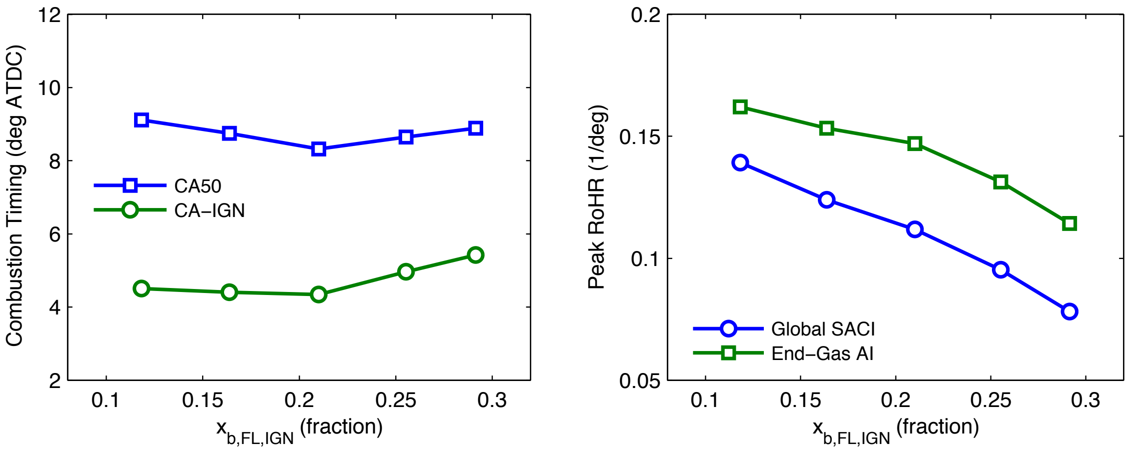

(a) (b)

Figure 4.3 – (a) Combustion timing and (b) peak RoHR vs. flame fraction at ignition.

But the results presented here also show that the peak RoHR in the auto-igniting end-gas region decreases as well, and this behavior cannot be explained by the argument of decreasing fuel energy for auto-ignition. As the flame fraction increases, ignition timing, ignition temperature and composition remain relatively fixed. The pressure at ignition increases as a result of the increasing flame heat release, and higher pressures under pure auto-igniting conditions will actually tend to increase the burn rate. These observations imply that, in theory, the end-gas burn rate should increase if chemistry alone is considered. Therefore, a likely explanation is that flame propagation is affecting the thermal and compositional gradients in the end-gas in a way that slows the ignition cascade process. The present model will attempt to capture these effects by including a term for the fraction of heat release by flame at the estimated point of ignition, or $x_{b,FL,IGN}$.

The following sub-sections describe the mathematical formulation and specific assumptions of the new empirical SACI auto-ignition burn rate model. The principal objective of this model is to capture the most important quantities that affect engine efficiency and the viable operating range. These are assumed to be combustion phasing (CA50), peak RoHR and combustion efficiency. The empirical burn rate model is tied to the conceptual SACI two-zone model presented in CHAPTER 2, and assumes that auto-ignition can be determined using mean quantities in a chemically reacting zone without heat release from other sources. This assumption is used with most single-zone and multi-zone models of pure HCCI combustion, as well as multi-zone SACI models such as the one developed in this work. More specifically, under spark-assisted operation, the combustion phasing, RoHR, and combustion efficiency computed by the model refer to the local end-gas auto-ignited combustion event. Under HCCI combustion, these quantities are assumed equivalent to their global counterparts. To ensure clarity, the nomenclature will be modified accordingly.

4.2.2 Ignition to 50% Burn Duration

The first component of the model is combustion phasing. The crank-angle at the normalized 50% burn is the standard combustion phasing result reported in engine research studies, as it generally incurs minimal modeling uncertainty from experimental heat release analysis. Previous work [17] demonstrated that a simple power law was enough to capture the effects of fuel energy and engine speed on combustion phasing and burn rate. Moreover, power laws are also present in most ignition delay correlations for the diluent and pressure terms, whereas the temperature term is exponential. After analyzing the data available in these terms, these formulations were identified as appropriate and have been adopted in the model. The new unmixedness and flame terms are applied as simple linear functions, with unity slope and intercept, within a power law expression. Other more complex approaches are possible, but the intention was to minimize the number of fit parameters. Combustion phasing was also found to be highly dependent on ignition timing, but with a behavior that cannot be modeled with a power law, in part due to the crank-angle scale. Various approaches were tested and a quadratic function provided adequate behavior with minimal complexity. The functional form of the combustion phasing model is shown in Equations (4.5) and (4.6), with fit parameters a_i $(i = 1, 2 \ldots 10)$. $\Delta\theta_{IGN-EG50}$ denotes the burn duration from the estimated time of auto-ignition (θ_{IGN}) to the time of the normalized 50% end-gas AI burn (θ_{EG50}), on a crank-angle scale:

$$\begin{aligned}\Delta\theta_{IGN-EG50} &= f_1(\theta_{IGN}) \\ &\times \left(\frac{\varphi}{0.5}\right)^{a_4} \left(\frac{1 - X_{SCP}}{0.3}\right)^{a_5} \exp\left(\frac{a_6}{T_{EG,IGN}/1100}\right) \left(\frac{P_{IGN}}{50}\right)^{a_7} \\ &\times \left(\frac{RPM}{2000}\right)^{a_8} \left(\frac{1 + f_{unmix}(iEGR)}{1.5}\right)^{a_9} \left(\frac{1 + x_{b,FL,IGN}}{1.5}\right)^{a_{10}}\end{aligned} \tag{4.5}$$

The quadratic function for ignition timing is given by:

$$f_1(\theta_{IGN}) = a_1 + a_2\theta_{IGN} + a_3\theta_{IGN}^2 \tag{4.6}$$

For numerical accuracy and computational precision during least-squares fitting, all the power law terms were centered using an approximate mean value for the expected range [23]. The model also assumes that ignition can be estimated in some way, either based on an ignition delay integral or with a more advanced method such as the one described in Section 3.2.6.

4.2.3 Rate of Heat Release at 50% Burn

The maximum RoHR generally occurs at, or very close, to the normalized 50% burn point. So from a mathematical modeling standpoint, it is convenient to choose the burn rate at this temporal location as a surrogate for the peak heat release rate. By capturing the peak RoHR, it will be possible to more accurately assess knock and ringing in auto-ignited combustion, since these characteristics are closely related to the peak pressure-rate and peak RoHR. For consistency reasons, the functional form for the normalized end-gas AI RoHR at 50% burn ($RoHR_{EG}|_{EG50}$) is very similar to the combustion phasing model, in this case with fit parameters b_i ($i = 1, 2 \ldots 10$). The main difference lies with the timing term. We can take advantage of the combustion phasing calculation to improve the accuracy of the $RoHR_{EG}|_{EG50}$ calculation by using θ_{EG50} instead of θ_{IGN}. Again, a quadratic function was found to be satisfactory to represent the functional behavior of θ_{EG50} without incurring additional unnecessary complexity.

$$\begin{aligned} RoHR_{EG}|_{EG50} = {} & f_2(\theta_{EG50}) \\ & \times \left(\frac{\varphi}{0.5}\right)^{b_4} \left(\frac{1 - X_{SCP}}{0.3}\right)^{b_5} \exp\left(\frac{b_6}{T_{EG,IGN}/1100}\right) \left(\frac{P_{IGN}}{50}\right)^{b_7} \\ & \times \left(\frac{RPM}{2000}\right)^{b_8} \left(\frac{1 + f_{unmix}(iEGR)}{1.5}\right)^{b_9} \left(\frac{1 + x_{b,FL,IGN}}{1.5}\right)^{b_{10}} \end{aligned} \tag{4.7}$$

The quadratic function for combustion phasing is given by:

$$f_2(\theta_{EG50}) = b_1 + b_2\theta_{EG50} + b_3\theta_{EG50}^2 \tag{4.8}$$

4.2.4 Combustion Efficiency

Combustion efficiency presents a more difficult problem for various reasons. First, the definition of combustion efficiency based on experimental data is typically not fully consistent with the requirement for models used in engine cycle simulations. Experimental combustion efficiencies are usually calculated using emissions data of partially oxidized species and an energy-based approach as described in [24], whereas most engine simulations apply a mass-based combustion efficiency to the burning law employed, resulting in fully unburned fuel at EVO. Moreover, the equilibrium assumption for the burned gases employed in most engine simulations affects the in-cylinder species present during the combustion event, which changes as the mixture expands and cools until to EVO. Experimental measurements also do not account for the actual amount of reactants in-cylinder when large amounts of exhaust gas are being recirculated, as is commonly done in advanced combustion engines. In ACE-HR, the exhaust combustion efficiency is modified to account for EGR using the expression presented in [25], which the author found necessary to match experimental data and engine cycle simulations. This value is further adjusted to account for estimated amount of flame heat release fraction at ignition as described in Section 3.2.7. Even though these approaches mix mass-based and energy-based definitions of combustion efficiency, and ignore potential equilibrium effects, they have shown to provide a suitable bridge between experimental results and modeling needs. The combustion efficiency predicted by the empirical model presented here is intended for use with a prescribed burn schedule, such as the one provided by a Wiebe function, which assumes a mass-based definition. Chemical equilibrium, if used, will determine the actual energy and species present once the given amount of fuel mass has been burned.

Previous simulation studies demonstrated that HCCI combustion efficiency correlates very well with peak temperature, as shown in Figure 4.4 for the simulation results in that study. Combustion efficiency appears to vary little for a wide range of temperatures, but the efficiency rapidly decreases as the temperature drops below some threshold value. To capture this behavior, the authors of [17] proposed fitting a hyperbola to two straight lines. This is conceptually shown in red in Figure 4.4 for a set of naturally aspirated high fidelity HCCI simulations.

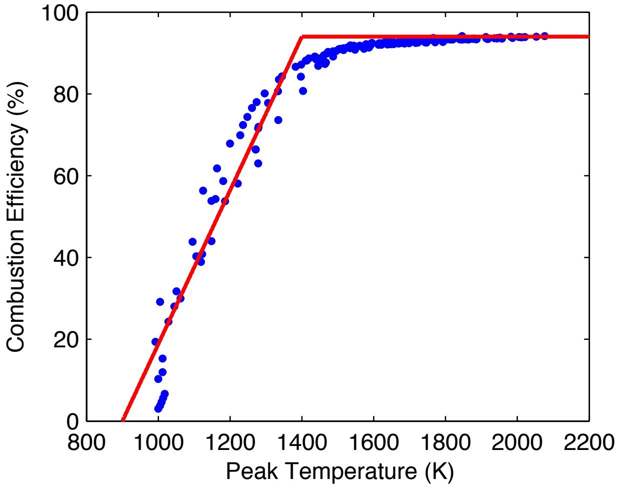

Figure 4.4 – Auto-ignition combustion efficiency vs. peak temperature from high fidelity HCCI simulation. The two intersection lines in the combustion efficiency regimes provide the basis for the hyperbolic fit used in the model.

We start with the general derivation of the hyperbolic fit. Consider two straight lines:

$$\begin{aligned} y_1 &= m_1 x + b_1 \\ y_2 &= m_2 x + b_2 \end{aligned} \tag{4.9}$$

If the parameters are not the same, then the two curves will intersect at some point. The aim is to find an expression of the curve that is asymptotic to these two lines. Another way to look at the equations is to put everything on the same side and equate to zero. Thus, the two line equations become:

$$\begin{aligned} y_1 - m_1 x - b_1 &= 0 \\ y_2 - m_2 x - b_2 &= 0 \end{aligned} \tag{4.10}$$

If a point is to lie on either of these two lines, then one of these two equations must be true (i.e. equal to zero). Therefore, a way to express this is by taking the product of the two lines and setting to zero:

$$(y_1 - m_1 x - b_1)(y_2 - m_2 x - b_2) = 0 \tag{4.11}$$

which can be rearranged to form a second order polynomial for y:

$$\begin{aligned} & y^2 + (-m_1 x - m_2 x - b_1 - b_2)y \\ & \quad + (m_1 m_2 x^2 + m_1 b_2 x + b_1 m_2 x + b_1 b_2) = 0 \end{aligned} \tag{4.12}$$

The above is a quadratic equation of the for $Ay^2 + By + C = 0$, where

$$\begin{aligned} A &= 1 \\ B &= -m_1 x - m_2 x - b_1 - b_2 \\ C &= m_1 m_2 x^2 + m_1 b_2 x + b_1 m_2 x + b_1 b_2 \end{aligned} \tag{4.13}$$

The two solutions to the above are:

$$y = \frac{-B \pm \sqrt{B^2 - 4AC}}{2A} \tag{4.14}$$

In order to add curvature between the two line segments, the product of the two line equations has to be equated to a positive number (instead of 0):

$$(y_1 - m_1 x - b_1)(y_2 - m_2 x - b_2) = g > 0 \tag{4.15}$$

Solving again for y results in a small modification for the expression for C:

$$C = m_1 m_2 x^2 + m_1 b_2 x + b_1 m_2 x + b_1 b_2 - g \tag{4.16}$$

The general hyperbolic fit presented above can then be applied to the observed relationship between combustion efficiency and peak temperature. Setting $y = \eta$ and $x = T - T_0$, the two line equations become:

$$\begin{aligned} \eta &= m_1(T - T_0) + b_1 \\ \eta &= m_2(T - T_0) + b_2 \end{aligned} \tag{4.17}$$

where η is the efficiency of auto-ignited combustion, T is the peak end-gas temperature and T_0 is a temperature at which the combustion efficiency reaches a value of η_0. This can be seen as the intersection point between the two lines. Using this assumption, it is possible to solve for the y-intercepts, where $b_1 = b_2 = \eta_0$. Based on the data in Figure 4.4, line 1 can also be assumed to be an asymptote of slope zero $(m_1 = 0)$. Applying these results to the equations for B and C, we obtain:

$$\begin{aligned} B &= -m_2(T - T_0) - \eta_0 - \eta_0 \\ &= -m_2(T - T_0) - 2\eta_0 \end{aligned} \tag{4.18}$$

$$\begin{aligned} C &= \eta_0 m_2(T - T_0) + \eta_0 \eta_0 - g \\ &= \eta_0[\eta_0 + m_2(T - T_0)] - g \end{aligned} \tag{4.19}$$

Therefore, to obtain an expression for the combustion efficiency as a function of peak temperature, it is necessary to fit four parameters: T_0, η_0, m_2 and g.

For consistency and improved accuracy, the combustion efficiency model developed in this work also includes the terms for composition, ignition state, engine speed, stratification and flame propagation used in the combustion phasing and heat release rate expressions. Furthermore, the parameters m_2, g and T_0 have been renamed to c_1, c_2 and c_3, respectively, completing the set of least-squares fitting parameters c_i $(i = 1, 2 \dots 10)$. Equation (4.20) shows the functional form of the combustion efficiency model:

$$\begin{aligned}\eta_{comb,AI} &= f_3\left(T_{EG,peak}\right) \\ &\times \left(\frac{\varphi}{0.5}\right)^{c_4} \left(\frac{1 - X_{SCP}}{0.3}\right)^{c_5} \exp\left(\frac{c_6}{T_{EG,IGN}/1100}\right) \left(\frac{P_{IGN}}{50}\right)^{c_7} \\ &\times \left(\frac{RPM}{2000}\right)^{c_8} \left(\frac{1 + f_{unmix}(iEGR)}{1.5}\right)^{c_9} \left(\frac{1 + x_{b,FL,IGN}}{1.5}\right)^{c_{10}}\end{aligned} \tag{4.20}$$

The hyperbolic fit describing the peak temperature dependency is recast with slightly different nomenclature in the following functions:

$$f_3\left(T_{EG,peak}\right) = \frac{-g_1\left(T_{EG,peak}\right) - \sqrt{g_1\left(T_{EG,peak}\right)^2 - 4 \cdot g_2\left(T_{EG,peak}\right)}}{2} \tag{4.21}$$

$$g_1\left(T_{EG,peak}\right) = -c_1\left(T_{EG,peak} - c_3\right) - 2\eta_0 \tag{4.22}$$

$$g_2\left(T_{EG,peak}\right) = \eta_0\left[\eta_0 + c_1\left(T_{EG,peak} - c_3\right)\right] - c_2 \tag{4.23}$$

It was opted to set the parameter η_0 manually in order to maintain a uniform number of least-squares fitting parameters for the three model components. It is also worth noting that the physical significance of the original hyperbola parameters (T_0, η_0), as the approximate values at which the two lines intersect, does not carry over when the rest of the power law terms are added to the model.

4.3 Least-Squares Model Fit

The 10 fit parameters for each model component are determined using the standard method of least squares using a combination of experimental data and high-fidelity simulation results. The ranges for each data set are shown in Table 3.1. The KMZ-HCCI simulation results were included to supplement the experimental data where limited conditions were available, such as in the engine speed and pressure space. The simulations were run for a single cycle, and initialized with a fully homogeneous mixture. For this reason, we are assuming here that the full amount of EGR is premixed. Since the HCCI and SACI experiments are predominantly controlled by an NVO strategy, the majority of the EGR is trapped internally. Therefore, the fully premixed assumption in the simulations completes the parameter space for the unmixedness factor. To prevent biasing the model towards the simulation results, the experimental data were weighted twice the simulation data when computing the least squares. The fit quality was assessed by visual residual analysis, as well as using the standard metric of the coefficient of determination, R^2. The adjusted R^2, which accounts for the number of fit parameters relative to data points, was also evaluated.

Table 4.1 – Description of experimental (FFVA) and simulation (KMZ) data used to fit empirical auto-ignition burn rate model.

	FFVA-HCCI (Experimental)	FFVA-SACI (Experimental)	KMZ-HCCI (Simulation)
# of points	384	151	460
$\Delta\theta_{IGN-EG50}$ (deg)	4.7 − 7.4	4.8 − 7.1	1.5 − 13.2
$RoHR_{EG}\|_{EG50}$ (1/deg)	0.10 − 0.21	0.10 − 0.18	0.05 − 0.44
$\eta_{comb,AI}$ (%)	84 − 97	87 − 96	51 − 99
θ_{IGN} (deg ATDC)	-8.0 − 4.7	0.4 − 7.8	-9.4 − 18.0
θ_{EG50} (deg ATDC)	-3.3 − 10.9	5.9 − 14.9	-7.0 − 28.1
φ	0.40 − 0.83	0.58 − 1.00	0.18 − 0.98
X_{SCP}	0.20 − 0.58	0.24 − 0.51	0.00 − 0.67
$T_{EG,IGN}$ (K)	1049 – 1139	1054 − 1133	982 – 1143
P_{IGN} (bar)	26 – 31	29 − 44	19 – 83
RPM	1985 – 2196	1986 − 2015	750 – 3750
f_{unmix}	0.81 − 1.00	0.55 − 0.99	0
$x_{b,FL,IGN}$	0	0.03 − 0.39	0
$T_{EG,peak}$ (K)	1495 − 2097	1831 − 2258	1123 – 2076

Figure 4.5 shows the correlation plot between the data and auto-ignition model estimates for the combustion phasing component, $\Delta\theta_{IGN-EG50}$, described in Section 4.2.2. The model is able to capture close to 80% of the variation observed in the data. Compared to the rest of the fitting results for the auto-ignition model, the $\Delta\theta_{IGN-EG50}$ correlation yielded the lowest fit quality in terms of R^2. This might be due to a variety of reasons. First, it could be related to the uncertainty in the ignition estimate or some other parameter. The slope of the simulation data also appears to be slightly different than that seen in the experimental data, indicating a potential difference in the combustion behavior of the simulation related to turbulence, chemistry or engine geometry. There is also the possibility that some physical behavior was simply not included in the model due to lack of knowledge. Overall, however, the experimental data are well correlated, so the

R^2 value most likely reflects the minor discrepancies in the simulation results, and, more importantly, the results indicate that the model can capture the principal effect of flame propagation effect on combustion phasing during SACI operation.

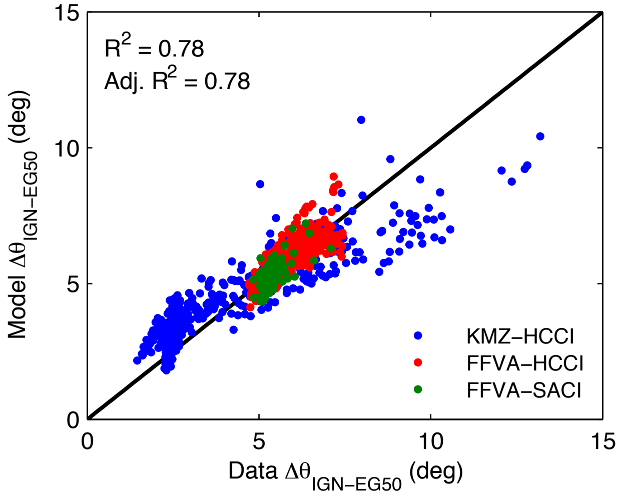

Figure 4.5 – Correlation plot of input data and empirical model predictions for end-gas auto-ignition combustion phasing (IGN-EG50) model.

The correlation results for the rate component of the empirical auto-ignition combustion model, $RoHR_{EG}|_{EG50}$, are shown in Figure 4.6. The fit quality is much higher, with 92% of the variation captured by the model. In part, this reflects the increased robustness in the CA50 and RoHR calculations, compared with ignition timing. Since the RoHR at CA50 is closely related to the peak RoHR, we can expect to capture the high load limits with relatively good accuracy.

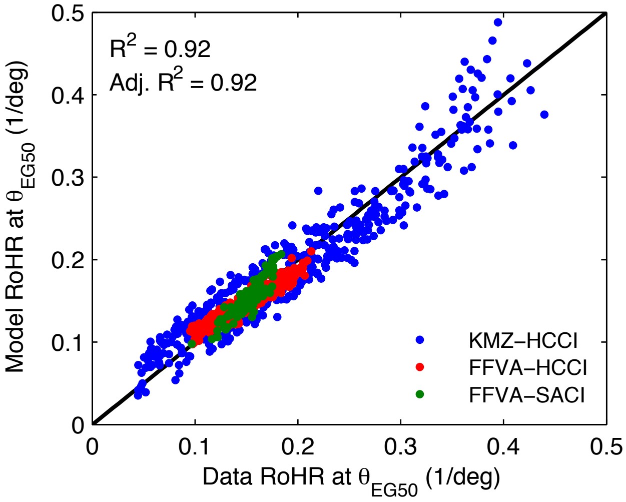

Figure 4.6 – Correlation plot of input data and empirical model predictions for end-gas auto-ignition burn rate (RoHR at EG50) model.

The correlation results for the combustion efficiency component of empirical auto-ignition model are shown in Figure 4.7. Since the high-fidelity model calculations used in the fit consider a single cycle only, it is possible to get much lower combustion efficiencies compared with the experiment, where one or more consecutive poor combustion events can induce large cyclic instability or misfire. Without the simulation data, it would not be possible to fit the proposed hyperbola, and the model would not be able to capture the rapid falloff beyond a threshold temperature.

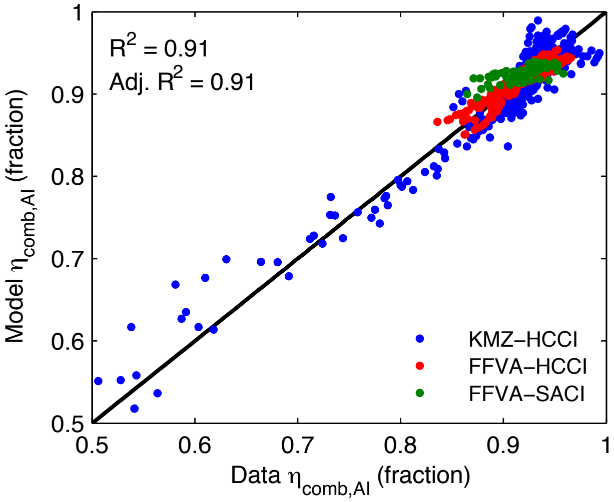

Figure 4.7 – Correlation plot of input data and empirical model predictions for end-gas auto-ignition combustion efficiency model.

The least squares fitting results for all three model components are presented in Table 4.2. For $\eta_{comb,AI}$, we have somewhat arbitrarily chosen $\eta_0 = 0.96$ in order to maintain a consistent number of 10 fit parameters per model component. Section 4.4 presents a detailed assessment of the model based on simple parametric studies, providing more intuitive interpretation of the physical significance of the computed fit parameters in terms of sign and magnitude.

Table 4.2 – Least squares fitting results for empirical auto-ignition burn rate model parameters.

$\Delta\theta_{IGN-\mathrm{EG50}}$		$RoHR_{EG}\vert_{EG50}$		$\eta_{comb,AI}$	
a_1	0.67	b_1	2.21E-02	c_1	11.18
a_2	3.93E-02	b_2	-1.22E-03	c_2	2589.11
a_3	1.35E-03	b_3	1.79E-05	c_3	902.64
a_4	-1.05	b_4	1.30	c_4	-0.14
a_5	-1.15	b_5	1.67	c_5	-0.16
a_6	3.36	b_6	0.16	c_6	0.37
a_7	-0.28	b_7	0.13	c_7	4.89E-03
a_8	0.25	b_8	-3.92E-03	c_8	-1.38E-02
a_9	1.13	b_9	-0.85	c_9	-5.25E-03
a_{10}	1.53	b_{10}	-2.12	c_{10}	3.65E-03

4.4 Assessment of General Model Behavior

In the following section we employ a series of parametric studies with inputs based on representative conditions for HCCI and SACI combustion. Ignition timing is varied from -5 to 10 deg ATDC at four levels of key model parameters. The results are presented in terms of end-gas combustion phasing ($EG50$), calculated by adding $\Delta\theta_{IGN-\mathrm{EG50}}$ to the prescribed θ_{IGN}, and end-gas burn rate at $EG50$, which is a direct output of the model.

4.4.1 Effects of Ignition Timing and Equivalence ratio

Figure 4.8 shows the parametric study results for ignition timing and fuel/air equivalence ratio, Φ, which is directly proportional to the molar fuel/oxygen ratio for a fixed residual gas fraction. We have selected typical HCCI naturally aspirated conditions at 2000 rev/min, where the pressure and temperature at ignition $(P_{IGN}, T_{EG,IGN})$ are 30 bar and 1100 K, respectively. The total EGR fraction ($tEGR$) of 10% and relative portion of internally trapped residuals $(iEGR/tEGR)$ of 100% resemble a positive valve overlap (PVO) strategy with no external recirculation. No flame propagation is considered in this case.

From the $\Delta\theta_{IGN-\mathrm{EG50}}$ correlation results displayed in Table 4.2, we see that the ignition timing function has positive coefficients $(a_1, a_2\ and\ a_3)$. The effects of the positive values are clearly illustrated in Figure 4.8(a) where later ignition timings always result in later overall combustion phasing. The later $EG50$ values then cause slower combustion rates, as shown in Figure 4.8(b), and is a direct result of the negative linear coefficient of the $EG50$ function (b_2). Both effects are significant, where delaying combustion ignition by 5 degrees from TDC can cause combustion to retard by approximately the same amount and the rate to drop by more than 30%. These results are also directionally consistent with fundamental combustion behavior in engines, where later phasing will tend to produce longer burn durations due to increasing piston expansion rates and charge cooling.

The trend with Φ is also meaningful. The burn duration and burn rate coefficients $(a_4\ and\ b_4)$ for the φ term, which is directly proportional to φ for a fixed residual dilution, have large magnitudes, indicating that fuel/oxygen content is a major influencing factor. The power law directionality (sign) is mathematically correct, where the rate has the inverse sign of the duration. It is also physically consistent, and is likely related to chemical "bootstrapping", where the increasing concentration of reactive intermediate species from the larger amount of fuel results in a compounding effect on the overall burn rate. Comparable results have been calculated in experimental ignition delay correlations [3]. Transport effects could also be involved, but they are more difficult to extract without more detailed knowledge of in-cylinder flows and gradients. Ultimately, for ignition at TDC, increasing the equivalence ratio from 0.2 to 0.5 results in a more than four-fold increase in the heat release rate. A similar trend is also noted in the combustion phasing, where the curves are closer together for higher fuel concentrations. At later burns, the differences become less significant due to the overwhelming effect of expansion cooling.

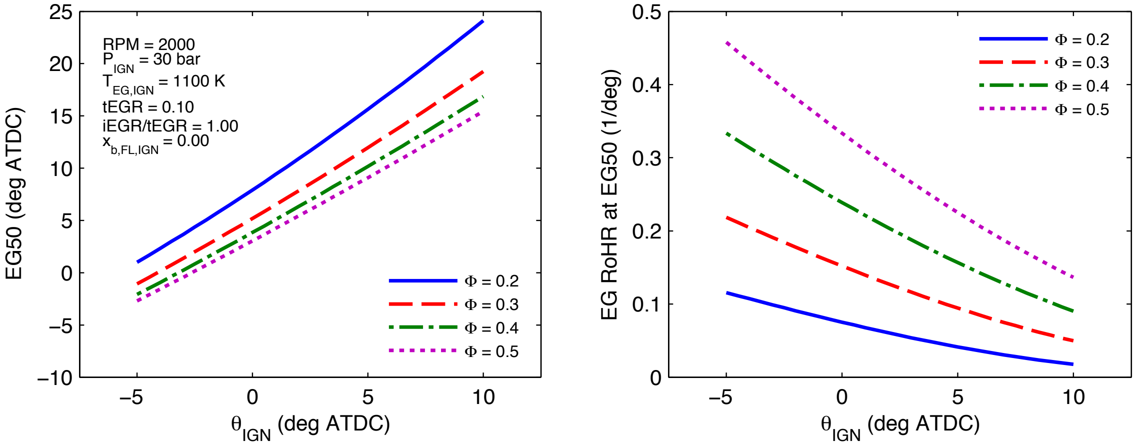

(a) (b)

Figure 4.8 – Empirical auto-ignition combustion model behavior as a function of ignition timing and equivalence ratio.

4.4.2 Effects of EGR Dilution

Figure 4.9 shows a second set of composition-related results for various levels of EGR dilution. EGR is set on a mass basis and assumed to be composed of complete combustion products. In this case, the equivalence ratio is stoichiometric, and EGR is assumed to be almost entirely premixed with the incoming charge. The trends with EGR are inverted compared with the Φ results, but otherwise very similar. This could be expected from the similar magnitude and sign of X_{SCP} parameters, a_5 and b_5. This can be related to changes in thermophysical properties and chemical reactions when the mixture contains larger amounts of inert product gases such as CO_2 and H_2O. Transport properties are also likely to play a role, but it is not possible to decompose the relative contributions with the amount of information available. With respect to an overall dilution basis, EGR appears to have a larger effect on burn rate compared to Φ. Increasing the EGR fraction from 50% to 80% is equivalent to decreasing Φ from 0.5 to 0.2 in terms of fuel energy content (assuming complete products for EGR); however, the burn rate decrease for ignition at TDC is more than 7X when employing EGR, compared to ~4.5X when diluting with air.

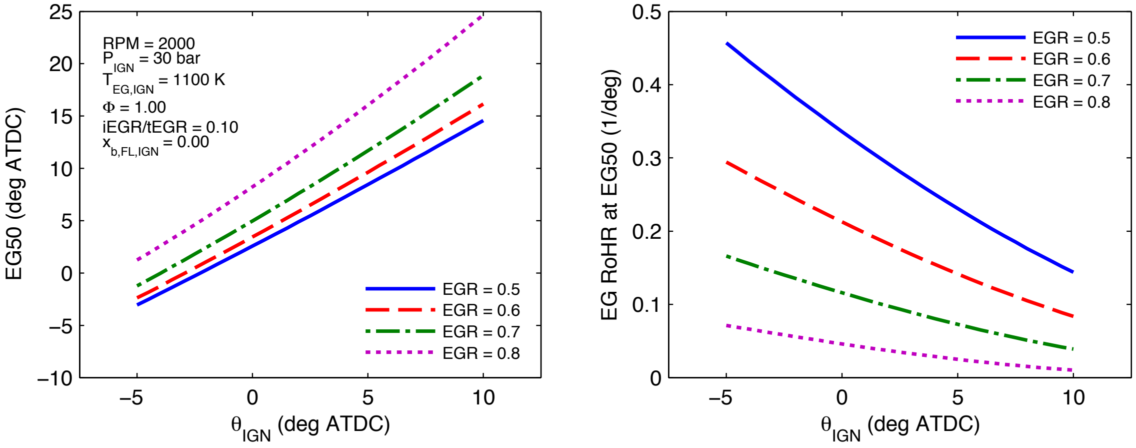

(a) (b)

Figure 4.9 – Empirical auto-ignition combustion model behavior as a function of ignition timing and EGR dilution (given on a mass fraction basis and composed of complete combustion products).

4.4.3 Effects of Ignition Pressure (Boost)

Intake charge boosting has been demonstrated to be a feasible load expansion strategy for HCCI, so it was of great interest to capture high pressure effects on combustion phasing and burn rate. Figure 4.10 shows results for the relevant parameter study, where ignition pressure is a proxy for intake pressure. The conditions are analogous to a potential boosted HCCI high load point. The trends as a function of pressure appear much less significant than with Φ or EGR, which is directly attributable to the noticeable smaller correlated power law coefficients, a_7 and b_7. Increasing pressure has been shown to decrease ignition delay for fuels without significant negative temperature behavior such as iso-octane [3], indicating that the correlated exponents and changes in burn rate seen in Figure 4.10(b) are directionally consistent. The results also show a diminishing effect on burn rate as pressure increases. Even though for these conditions, the rate of heat release with ignition at TDC is relatively high (compared to experimental results of non-knocking combustion typically on the order of ~0.1-0.2 1/deg), the results show later phasing can significantly reduce heat release rates, potentially enabling boosted high load operation.

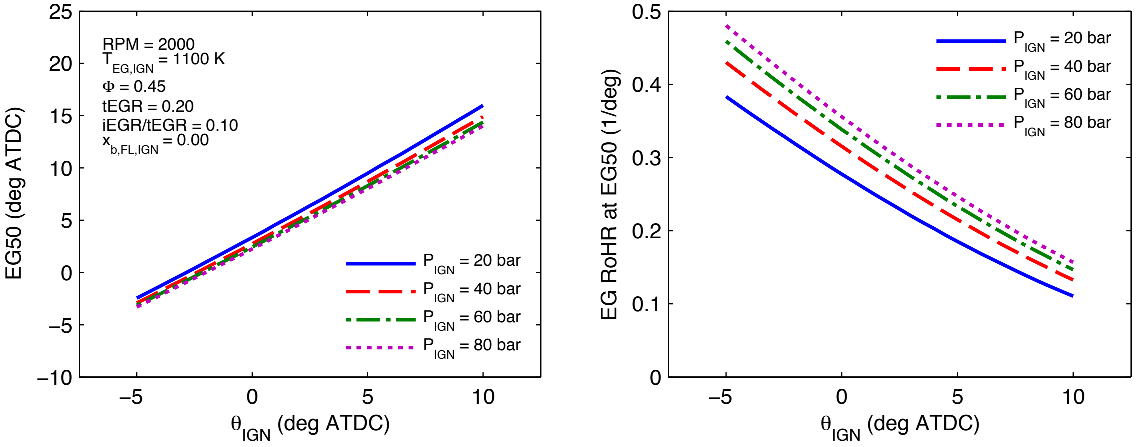

(a) (b)

Figure 4.10 – Empirical auto-ignition combustion model behavior as a function of ignition timing and ignition pressure, representative of intake charge boosting.

4.4.4 Effects of Engine Speed

The behavior of the model with respect to engine speed is presented in Figure 4.11 for typical naturally aspirated HCCI operating conditions employing large amounts of internally trapped residuals. The effects appear relatively mild, considering the large speed range. Also, compared to the burn duration exponent a_8 of 0.25, the burn rate fitting value of b_8 is two orders of magnitude smaller, which means it scales directly with the speed. This is reasonable since burn rate is defined on a crank-angle basis. The changes observed in Figure 4.11(b) are then almost exclusively due to the change in phasing in Figure 4.11(a). Given the same ignition timing and approximately the same thermal state and composition, the longer durations seen as the engine speed increases are mostly the result of overall less time available for finite rate chemistry to occur. Thermal and compositional gradients could also be affected by changing turbulence. From the results in Figure 4.11, it would sensible to conclude that it is possible to run HCCI up to very high engine speeds; however, most experimental and computational studies have shown consistent speed limits around 4000 rpm [5], [26], [27]. The difficulty usually arises in achieving auto-ignition because, as engine speed increases, less time is available for chemistry to reach the critical ignition point.

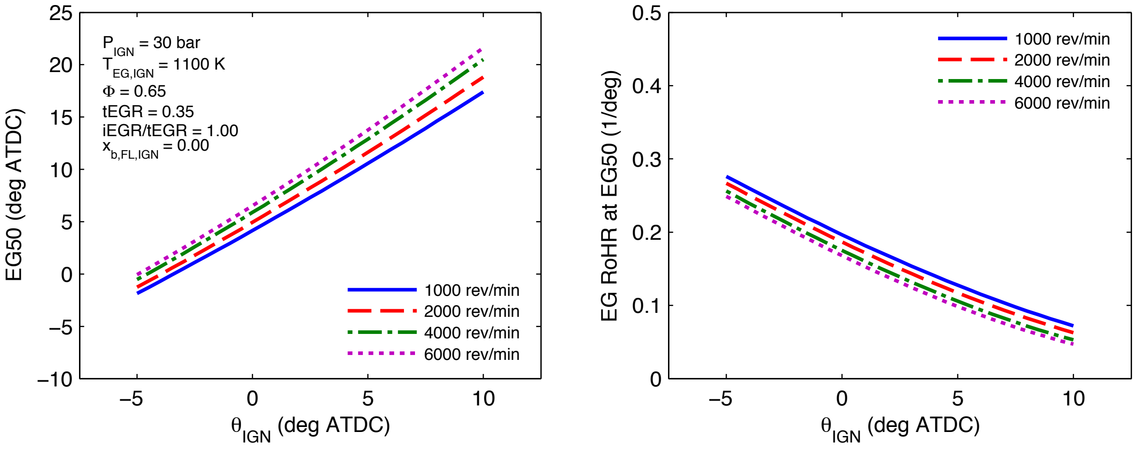

(a) (b)

Figure 4.11 – Empirical auto-ignition combustion model behavior as a function of ignition timing and engine speed.

4.4.5 Effects of Unmixedness/Stratification

Temperature and charge stratification in HCCI engines related to charge preparation strategies has been the subject of recent computational studies by Kodavasal

[20], where it was found that temperature gradients developing as a result of internal residual trapping strategies could have significant effects on burn rates. These effects are incorporated in the empirical auto-ignition model using the proposed unmixedness factor, $f_{unmix}(iEGR)$. The fitted coefficients a_9 and b_9 in Table 4.2 for burn duration and rate are relatively large, demonstrating that the model is sensitive to the unmixedness factor. The results in Figure 4.12 quantitatively show this for the same naturally aspirated HCCI conditions presented in the previous section. In this case, the internal EGR fraction is progressively changed from 25% to 100% of the total. For ignition at TDC, the model predicts that combustion phasing will be retarded by 1.7 deg, and the burn rate is decreased by 34%. This is on the same order of magnitude as the results from Kodavasal [20] when he compared NVO strategies to premixed heated intake charge.

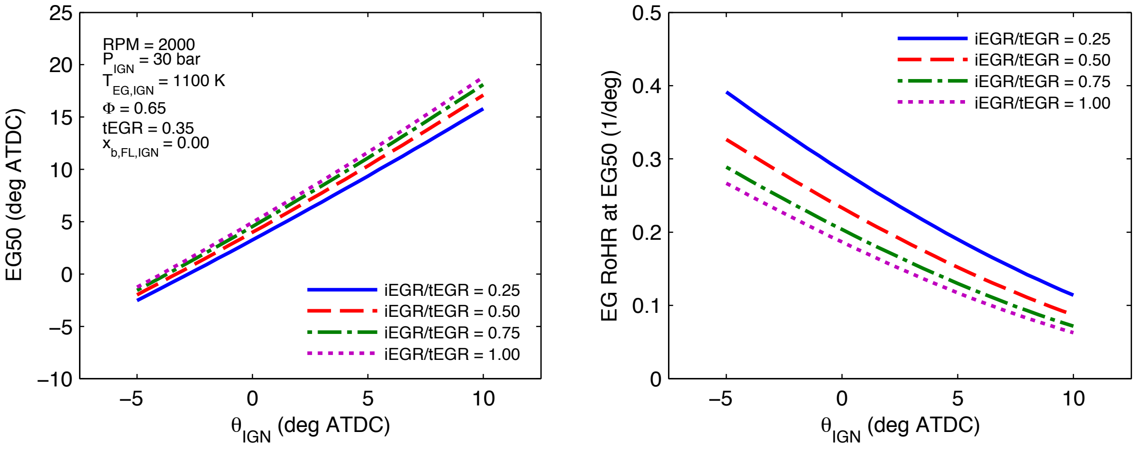

(a) (b)

Figure 4.12 – Empirical auto-ignition combustion model behavior as a function of ignition timing and relative internal EGR fraction, which is used as an indication of in-cylinder stratification.

4.4.6 Effects of Flame Propagation

We can also evaluate the behavior of the model under expected SACI operating conditions, and assess the potential for burn rate control and load expansion using flame propagation, as shown in Figure 4.13. The equivalence ratio for this case has been set to stoichiometric with 40% EGR, where half of the EGR is internal. This would correspond to mid/high load SACI operation according the experimental results by Manofsky [28]. The relatively large magnitude of the fitted exponents a_{10} and b_{10} for the flame fraction burned at auto-ignition indicates that flame propagation has a significant effect on both burn duration and heat release rate. Assuming ignition at TDC, the results in Figure 4.13 show that it would in theory be possible to delay combustion phasing 3 degrees by allowing a flame to consume 60% of the charge, while at the same time decreasing the burn rate more than three-fold. This presents a key motivation for employing SACI, and potentially coupling SACI to boosted conditions for high load advanced combustion strategies.

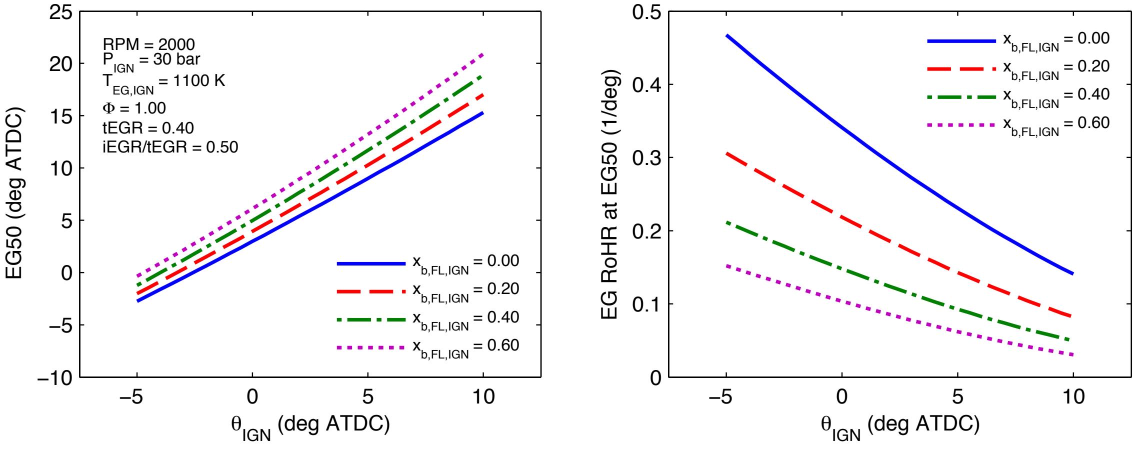

(a) (b)

Figure 4.13 – Empirical auto-ignition combustion model behavior as a function of ignition timing and burn fraction by flame at ignition, representative of SACI operation.

4.5 Model Sensitivity Analysis

A sensitivity analysis was conducted to provide quantitative understanding of the impact of uncertainty in the input parameters. We have adopted a sensitivity analysis instead of a strict uncertainty analysis, since it is difficult to incorporate all the sources of uncertainty in an explicit way. Examples of uncertainty include measurement accuracy, cyclic variability in engine experiments, uncertainty in the chemical kinetic rates used in the simulations and estimation errors in the analytical methods for quantities such as ignition timing as a result of noise, to name a few. Section 3.4 presented a sensitivity assessment of the experimental analysis for an HCCI and SACI case, illustrating the major sources of error when computing the input data used in the model. Here we employ a similar approach for four cases corresponding to representative HCCI and SACI conditions under naturally aspirated and boosted operation. At each base condition, the input parameters for the three model components are perturbed by approximately 10% high and low, and combined to give an estimated overall prediction sensitivity parameter using Equation (4.24), where Y_j is the prediction for each model component j (e.g. θ_{EG50}, $RoHR_{EG}|_{EG50}$ and $\eta_{comb,AI}$) and X_i are the respective individual model inputs (e.g. θ_{IGN}, φ, P_{IGN}, etc.). Numerical finite difference methods are used to calculate the partial derivatives around a small interval for each baseline point. Similar results would be obtained by parametrically varying the inputs and obtaining the individual outputs, but this method is more consistent with typical experimental uncertainty analysis.

$$\Delta Y_j = \left[\sum \left(\frac{\partial Y_j}{\partial X_i} dX_i\right)^2\right]^{1/2} \tag{4.24}$$

The sensitivity analysis input parameter setup for the HCCI cases is shown in Table 4.3. The input parameters have been approximated from actual experimental conditions in [28], [29]. To compute the local gradient (∂X_i), ignition timing was varied by 0.05 degrees around the baseline, and the rest of the parameters were varied by 0.1%. The sensitivity dX_i was assessed using an interval of 5 degrees for ignition timing and a 10% interval for the rest.

Table 4.3 – Baseline conditions for sensitivity analysis of empirical auto-ignition burn rate model for HCCI cases.

Parameter	**HCCI – Nat. Asp.**	**HCCI - Boosted**
θ_{IGN}	0 deg ATDC	5 deg ATDC
$\Phi\ (\varphi)$	0.65	0.45
$tEGR\ (X_{SCP})$	35 %	20 %
P_{IGN}	30 bar	50 bar
$T_{EG,IGN}$	1100 K	1100 K
RPM	2000 rev/min	2000 rev/min
$iEGR\ (f_{unmix})$	33 %	2 %
$T_{EG,peak}$	1900 K	1900 K

Table 4.4 and Table 4.5 summarize the model sensitivity analysis results for naturally aspirated and boosted HCCI, respectively. ΔY_j is given on an absolute basis for combustion phasing (θ_{EG50}), and on a relative percent change basis for burn rate ($RoHR_{EG}|_{EG50}$) and combustion efficiency $\left(\eta_{comb,AI}\right)$. For this specified range it was found that the burn rate model is most sensitive to ignition timing, resulting in a 6.3 deg change θ_{EG50} and a 41% change in $RoHR_{EG}|_{EG50}$. The latter was also noticeably affected by the composition variables, φ and X_{SCP}, as well as the end-gas temperature at ignition $\left(T_{EG,IGN}\right)$, with sensitivities between 10-15%. The rest of the parameters showed variations of less than 5% for the imposed error. For the combustion efficiency, most of the sensitivities were relatively low with the temperature input resulting in the largest values close to 5%. The behavior between the naturally aspirated and boosted conditions was relatively similar. The naturally aspirated case showed a total sensitivity given by Equation (4.24) of 4.43 deg for θ_{EG50} and 32% for $RoHR_{EG}|_{EG50}$. The boosted case

displayed slightly lower values, with 4.37 deg and 26%, respectively. This reduction could be in part due to the lower sensitivities to errors in $T_{EG,IGN}$ (7.6%) and X_{SCP} (5.2%), compared to >10% in the naturally aspirated case. In both cases the total sensitivity for the combustion efficiency was less than 0.5%.

Table 4.4 – Model sensitivity analysis summary for naturally aspirated HCCI conditions.

Sensitivity Parameters (Base X_i)	**Sensitivity Results, ΔY_j (Base Y_j)**		
	θ_{EG50} (4.87 deg ATDC)	$RoHR_{EG}\vert_{EG50}$ (0.19 1/deg)	$\eta_{comb,AI}$ (92.55 %)
θ_{IGN} (0 deg ATDC)	+6.30 deg	−41.55 %	n/a
RPM (2000 rev/min)	+0.13 deg	−0.83 %	−0.14 %
P_{IGN} (30 bar)	−0.14 deg	+2.24 %	+0.05 %
$T_{EG,IGN}$ (1100 K)	−1.88 deg	+10.00 %	−3.94 %
φ (0.55)	−0.52 deg	+14.98 %	−1.37 %
X_{SCP} (23.70 %)	+0.42 deg	−13.41 %	+0.80 %
$iEGR$ (33 %)	+0.14 deg	−3.02 %	−0.01 %
$x_{b,FL,IGN}$ (0 %)	n/a	n/a	n/a
$T_{EG,peak}$ (1900 K)	n/a	n/a	+4.58 %

Table 4.5 – Model sensitivity analysis summary for boosted HCCI conditions.

Sensitivity Parameters (Base X_i)	**Sensitivity Results, ΔY_j (Base Y_j)**		
	θ_{EG50} (8.46 deg ATDC)	$RoHR_{EG}\|_{EG50}$ (0.23 1/deg)	$\eta_{comb,AI}$ (94.73 %)
θ_{IGN} (5 deg ATDC)	+5.95 deg	−43.79 %	n/a
RPM (2000 rev/min)	+0.09 deg	−0.66 %	−0.14 %
P_{IGN} (50 bar)	−0.10 deg	+2.06 %	+0.05 %
$T_{EG,IGN}$ (1100 K)	−1.34 deg	+7.58 %	−3.94 %
φ (0.40)	−0.38 deg	+15.01 %	−1.40 %
X_{SCP} (9.47 %)	+0.12 deg	−5.21 %	+0.37 %
$iEGR$ (2 %)	+0.03 deg	−0.80 %	−0.00 %
$x_{b,FL,IGN}$ (0 %)	n/a	n/a	n/a
$T_{EG,peak}$ (1900 K)	n/a	n/a	+4.58 %

Table 4.6 reports the sensitivity analysis setup for the naturally aspirated and boosted SACI cases. The conditions for the naturally aspirated case were also based on the experimental data of [28]; however, boosted SACI data are not yet available in the literature, so the parameters were estimated assuming a similar relationship to their HCCI counterparts.

Table 4.6 – Baseline conditions for sensitivity analysis of empirical auto-ignition burn rate model for SACI cases.

Parameter	**SACI – Nat. Asp.**	**SACI - Boosted**
θ_{IGN}	0 deg ATDC	5 deg ATDC
Φ (φ)	0.95	0.95
$tEGR$ (X_{SCP})	40 %	50 %
P_{IGN}	30 bar	50 bar
$T_{EG,IGN}$	1100 K	1100 K
RPM	2000 rev/min	2000 rev/min
$iEGR$ (f_{unmix})	20 %	10 %
$x_{b,FL,IGN}$	30 %	30 %
$T_{EG,peak}$	1900 K	1900 K

Table 4.7 and Table 4.8 summarize the model sensitivity analysis results for naturally aspirated and boosted SACI, respectively. The general sensitivity behavior is consistent with the HCCI results, with variations in ignition timing also causing the largest prediction error, on the order of 6 deg for θ_{EG50} and 40-50% for $RoHR_{EG}|_{EG50}$. Likewise, φ, X_{SCP} and $T_{EG,IGN}$ had noticeable effects, with sensitivities above 10% for all three parameters. For the prescribed SACI conditions, the model was more sensitive to X_{SCP} than to φ, as in the HCCI cases. The related error was 17% for naturally aspirated operation and 25% for boosted operation. The flame term, $x_{b,FL,IGN}$, displayed mild sensitivities on the order of 6%, for both SACI conditions. This additional parameter, as well as the greater errors due to θ_{IGN} and X_{SCP}, increased the overall sensitivity of the burn rate to 43% and 51% in the naturally aspirated and boosted SACI cases, respectively. The combustion phasing sensitivity did not change significantly. Combustion efficiency was again minimally affected by most parameters, except the peak temperature, which caused a 4.5% change. The overall cumulative sensitivity, however, was still below 1%.

Table 4.7 – Model sensitivity analysis summary for naturally aspirated SACI conditions.

Sensitivity Parameters (Base X_i)	**Sensitivity Results, ΔY_j (Base Y_j)**		
	θ_{EG50} (4.68 deg ATDC)	$RoHR_{EG}\vert_{EG50}$ (0.17 1/deg)	$\eta_{comb,AI}$ (89.41 %)
θ_{IGN} (0 deg ATDC)	+6.25 deg	−40.97 %	n/a
RPM (2000 rev/min)	+0.12 deg	−0.79 %	−0.14 %
P_{IGN} (30 bar)	−0.14 deg	+2.20 %	+0.05 %
$T_{EG,IGN}$ (1100 K)	−1.81 deg	+9.49 %	−3.94 %
φ (0.92)	−0.50 deg	+13.94 %	−1.33 %
X_{SCP} (39.08 %)	+0.50 deg	−17.46 %	+1.03 %
$iEGR$ (20 %)	+0.16 deg	−3.57 %	−0.02 %
$x_{b,FL,IGN}$ (30 %)	+0.16 deg	−6.03 %	+0.01 %
$T_{EG,peak}$ (1900 K)	n/a	n/a	+4.58 %

Table 4.8 – Model sensitivity analysis summary for boosted SACI conditions.

Sensitivity Parameters (Base X_i)	**Sensitivity Results, ΔY_j (Base Y_j)**		
	θ_{EG50} (10.43 deg ATDC)	$RoHR_{EG}\|_{EG50}$ (0.10 1/deg)	$\eta_{comb,AI}$ (92.38 %)
θ_{IGN} (5 deg ATDC)	+6.48 deg	−51.27 %	n/a
RPM (2000 rev/min)	+0.14 deg	−1.08 %	−0.14 %
P_{IGN} (50 bar)	−0.16 deg	+2.53 %	+0.05 %
$T_{EG,IGN}$ (1100 K)	−2.10 deg	+13.63 %	−3.94 %
φ (0.90)	−0.57 deg	+14.13 %	−1.30 %
X_{SCP} (48.64 %)	+0.74 deg	−25.27 %	+1.54 %
$iEGR$ (10 %)	+0.15 deg	−3.13 %	−0.01 %
$x_{b,FL,IGN}$ (30 %)	+0.19 deg	−6.43 %	+0.01 %
$T_{EG,peak}$ (1900 K)	n/a	n/a	+4.58 %

4.6 Generating Full Burn Rate Profile

4.6.1 New Rate-Based Wiebe Function Fitting Approach

To use the empirical combustion model in engine simulations, a standard Wiebe function was employed to translate the model into profiles for burn fraction and a burn rate. The normalized expression for the burn fraction according to the Wiebe function is given by:

$$x_b = 1 - \exp\left[-\left(\frac{\theta - \theta_0}{\Delta\theta}\right)^{w+1}\right] \tag{4.25}$$

The rate form of the Wiebe function, differentiated with respect to crank-angle, is given by:

$$\dot{x}_b = \left(\frac{w+1}{\Delta\theta}\right)\left(\frac{\theta - \theta_0}{\Delta\theta}\right)^{w} \exp\left[-\left(\frac{\theta - \theta_0}{\Delta\theta}\right)^{w+1}\right] \tag{4.26}$$

Three shape parameters define the Wiebe function, θ_0, $\Delta\theta$ and w. The empirical model provides us with three known points that can be applied to the equations above: $(\theta_0, x_{b,0})$, $(\theta_{50}, x_{b,50})$ and $(\theta_{50}, \dot{x}_{b,50})$, where $x_{b,0} = 0$ and $x_{b,50} = 0.50$. Because we will have other means for computing the initial slow heat release leading to ignition, the Wiebe function will only be used to obtain the post-ignition burn profile and allows us to assume $\theta_0 = \theta_{IGN}$. The x-coordinate of the second point and y-coordinate of the third point are obtained directly from the empirical model, where $\theta_{50} = \theta_{EG50}$ and $\dot{x}_{b,50} = RoHR_{EG}|_{EG50}$. The final burn rate is obtained by multiplying the above expressions with the computed parameters times the combustion efficiency. This novel approach for fitting the Wiebe function using the rate at 50% instead of the more traditional burn duration from 0- or 10-90% is much better suited to peak heat release rate and HCCI knock predictions. The main limitation of this approach is that the final burn interval will not be adequately captured. This is considered acceptable, since the main objective of the studies using this model is to assess engine efficiency trends and load limits, which are less sensitive to the latter phase of combustion. Moreover, this portion of the burn curve is subject to much higher uncertainty when computed from experimental data (see Section 3.4) and the true shape is also the result of complex crevice flows and late burning events, which are difficult to capture with a model. On the other hand, θ_{50} and the peak rate of heat release, which is close to $\dot{x}_{b,50}$ are much more robust quantities to extract from experimental, and have a direct effect on efficiency and knock.

By mathematical manipulation, it is possible to obtain an analytical solution to the system of equations above. Rearrange Equations (4.25) and (4.26):

$$x_b = 1 - \exp\left[-\left(\frac{1}{\Delta\theta}\right)^{w+1} (\theta - \theta_0)^{w+1}\right] \tag{4.27}$$

$$\dot{x}_b = (w+1)(\theta - \theta_0)^w \left(\frac{1}{\Delta\theta}\right)^{w+1} \exp\left[-\left(\frac{1}{\Delta\theta}\right)^{w+1} (\theta - \theta_0)^{w+1}\right] \tag{4.28}$$

and creating a substitution variable A, where:

$$A = \left(\frac{1}{\Delta\theta}\right)^{w+1} \tag{4.29}$$

Equations (4.27) and (4.28) can be expressed as:

$$x_b = 1 - \exp[-A(\theta - \theta_0)^{w+1}] \tag{4.30}$$

$$\dot{x}_b = (w+1)(\theta - \theta_0)^w A \exp[-A(\theta - \theta_0)^{w+1}] \tag{4.31}$$

Applying the known values at 50% burn, θ_{50}, $x_{b,50}$ and $\dot{x}_{b,50}$:

$$x_{b,50} = 1 - \exp[-A(\theta_{50} - \theta_0)^{w+1}] \tag{4.32}$$

$$\dot{x}_{b,50} = (w+1)(\theta_{50} - \theta_0)^w A \exp[-A(\theta_{50} - \theta_0)^{w+1}] \tag{4.33}$$

Equation (4.32) can now be partially solved for the unknowns:

$$\exp[-A(\theta_{50} - \theta_0)^{w+1}] = 1 - x_{b,50} \tag{4.34}$$

$$-A(\theta_{50} - \theta_0)^{w+1} = \ln\left(1 - x_{b,50}\right) \tag{4.35}$$

$$-A(\theta_{50} - \theta_0)^w(\theta_{50} - \theta_0) = \ln\left(1 - x_{b,50}\right) \tag{4.36}$$

$$A(\theta_{50}-\theta_0)^w = -\frac{\ln\left(1-x_{b,50}\right)}{(\theta_{50}-\theta_0)} \tag{4.37}$$

The R.H.S. of Equation (4.37) is known, so a new substitution variable B can be created:

$$B = A(\theta_{50}-\theta_0)^w = -\frac{\ln\left(1-x_{b,50}\right)}{(\theta_{50}-\theta_0)} \tag{4.38}$$

Now taking Equation (4.33) and rearranging we get:

$$\dot{x}_{b,50} = (w+1)\, A(\theta_{50}-\theta_0)^w \exp[-A(\theta_{50}-\theta_0)^w(\theta_{50}-\theta_0)] \tag{4.39}$$

and substituting the variable B:

$$\dot{x}_{b,50} = (w+1)\, B \exp[-B(\theta_{50}-\theta_0)] \tag{4.40}$$

Thus, a solution for the shape parameter w can be readily obtained:

$$\frac{\dot{x}_{b,50}}{B\exp[-B(\theta_{50}-\theta_0)]} = (w+1) \tag{4.41}$$

$$w = \frac{\dot{x}_{b,50}}{B\exp[-B(\theta_{50}-\theta_0)]} - 1 \tag{4.42}$$

Knowledge of w can then be used together with B to determine A:

$$A = \frac{B}{(\theta_{50}-\theta_0)^w} \tag{4.43}$$

which is used in Equations (4.30) or (4.31) to compute the burn fraction and burn rate, respectively, as a function of crank-angle.

4.6.2 Blending Pre-Ignition Heat Release with Wiebe Function

The Wiebe function fit described in the previous section only provides the post-ignition burn rate. If heat release is also computed before the main ignition event, e.g. using chemical kinetics, the pre-ignition burn rate must be transitioned with the Wiebe function to create a continuous heat release schedule. The Bézier curve, commonly used in computer graphics to model smooth curves, has been adopted as the blending function for the present work. The quadratic Bézier curve expression is given by:

$$\mathbf{B}(t) = (1-t)^2\mathbf{P_0} + 2(1-t)t\mathbf{P_1} + t^2\mathbf{P_2}\,, \qquad t \in [0,1] \tag{4.44}$$

where $\mathbf{P_k}$ are the three control points and t is a unit distance traversing the blending space. The ignition timing and burn fraction are set as the first control point, $\mathbf{P_0}$. The second control point, $\mathbf{P_1}$, is obtained by connecting a line from the ignition point with a constant slope and finding the intersection point with the Wiebe function. The third control point, $\mathbf{P_2}$, is assumed to be located at the same unit distance from $\mathbf{P_1}$as $\mathbf{P_1}$is from $\mathbf{P_0}$. One potential issue with this approach is if the ignition timing estimate is too late and/or the slope is too high, the line from $\mathbf{P_0}$ can intersect at very late locations or even miss the Wiebe function altogether. The ignition estimate is therefore adjusted as necessary to obtain an intersection point before the average of the ignition timing and the 50% burn location. Figure 4.14 shows a sample burn profile fit and the associated blending procedure using experimental results.

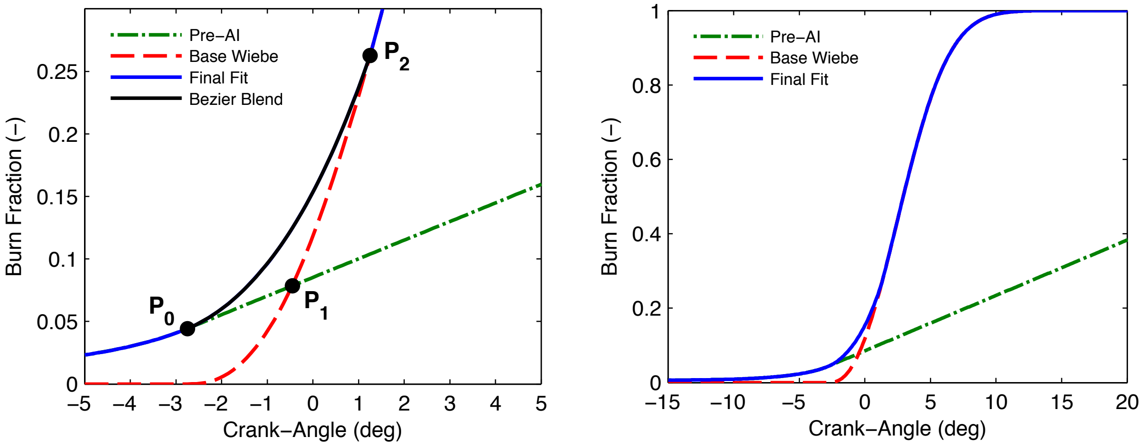

(a) (b)

Figure 4.14 – (a) Bezier blending curve between initial auto-ignition heat release phase (experimental) and fitted Wiebe function. (b) Complete combustion profile based on experimental input data.

4.7 Model Validation

To validate the empirical auto-ignition burn model, an HCCI data set was selected that includes data not used in the least squares fit. Notably, these experiments were part of a larger study intended to understand fuel composition effects on burn rate, and uses iso-octane instead of the research grade gasoline used in all of the experiments used to fit the model. The results are from a combustion phasing study using NVO at fixed fueling rate and intake temperature. The purpose of this validation exercise is to assess the complete post-ignition empirical burn rate modeling approach. Thus, the empirical fit is calculated using the experimental operating conditions, ignition timing estimate and the related end-gas state. The experimental pre-ignition burn fractions are then blended with the Wiebe function to obtain the final burn curve.

Figure 4.15 compares the resulting burn profile to the mean experimental calculation including combustion efficiency for one operating condition. It can be readily seen that the main portion of the burn profile is captured with good accuracy, both in terms of rate and combustion phasing. The difference in the latter burn interval was expected as a result of the Wiebe fitting approach (see Section 4.6.1). It is worth noting that capturing the full shape of this curve would be very difficult, if not impossible, with the standard Wiebe function. Using a more complex approach, such as a double Wiebe, could potentially approximate the measured burn fraction with better fidelity, but would require an extended empirical model. This is a possible area of future improvement.

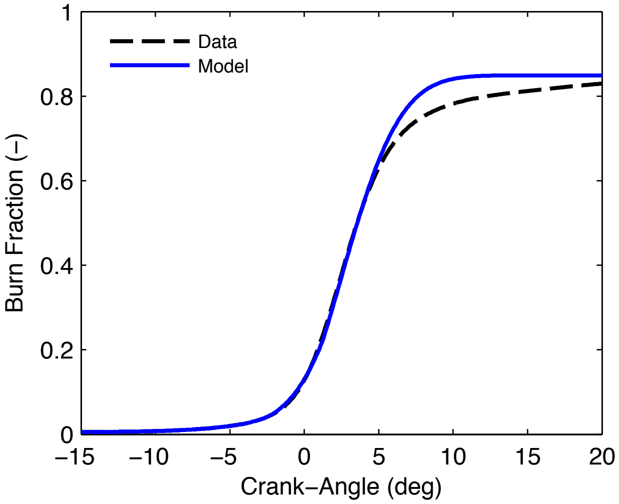

Figure 4.15 – Comparison between experimental heat release profile (data) and empirical model prediction for an HCCI operating condition.

Figure 4.16 presents key results for the combustion phasing study. The error bars in the experimental data indicate one standard deviation of the cycle-by-cycle results. Figure 4.16(a) compares the combustion phasing results from the empirical model with the experimental data. The model shows good trend-wise and absolute agreement, where the model results are entirely within the experimental cycle-by-cycle variability. The trend for the peak relative burn rate, shown in Figure 4.16(b), also demonstrates good agreement, with a maximum error between the model and experimental data of ~10%.

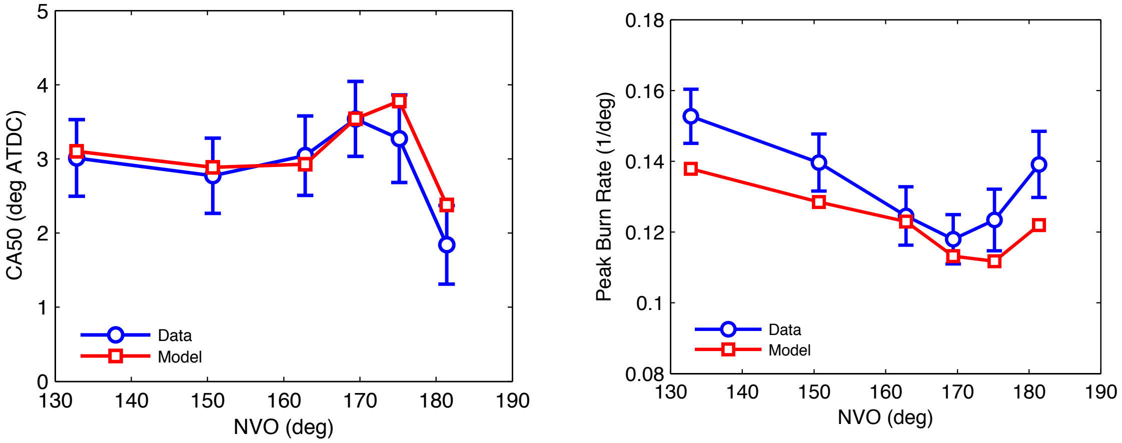

(a) (b)

Figure 4.16 – (a) Combustion phasing and (b) peak burn rate validation results of empirical auto-ignition burn rate model. The error bars of the experimental data represent on one standard deviation of the cyclic variability.

The largest absolute errors are found in the 10-90% burn duration, shown in Figure 4.17. These can be related to the behavior observed in Figure 4.15, where the experimental data exhibits a long "tail" at the end of combustion that cannot be replicated by the Wiebe function. Overall, the model appears to behave appropriately and capture the key trends in quantities such as combustion phasing and peak burn rate that will be important for assessing operating limits and engine efficiency.

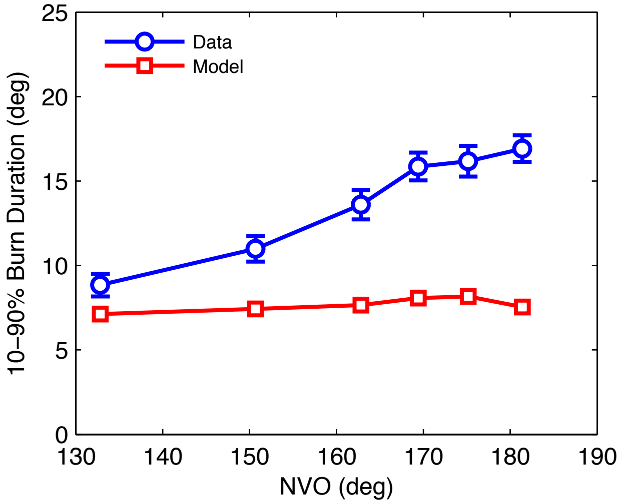

Figure 4.17 – Comparison of 10-90% burn duration between experimental data and empirical auto-ignition burn rate model predictions. The discrepancy is due to the inability of the standard Wiebe function to accurately capture the slow burn characteristics during the last phase of combustion observed in the experimental data. The error bars of the experimental data represent on one standard deviation of the cyclic variability.

4.8 References

[1] J. C. Livengood and P. C. Wu, “CORRELATION OF AUTOIGNITION PHENOMENA IN INTERNAL COMBUSTION ENGINES AND RAPID COMPRESSION MACHINES,” *5th Symposium on Combustion*, pp. 347–356, 1955.

[2] A. M. Douaud and P. Eyzat, “Four-Octane-Number Method for Predicting the Anti-Knock Behavior of Fuels and Engines,” *SAE 780080*, 1978.

[3] X. He, M. T. Donovan, B. T. Zigler, T. R. Palmer, S. M. Walton, M. S. Wooldridge, and A. Atreya, “An experimental and modeling study of iso-octane ignition delay times under homogeneous charge compression ignition conditions,” *Combustion and Flame*, vol. 142, no. 3, pp. 266–275, 2005.

[4] S. S. Goldsborough, “A chemical kinetically based ignition delay correlation for iso-octane covering a wide range of conditions including the NTC region,” *Combustion and Flame*, vol. 156, no. 6, pp. 1248–1262, 2009.

[5] E. Ortiz-Soto, D. Assanis, and A. Babajimopoulos, “A comprehensive engine to drive-cycle modelling framework for the fuel economy assessment of advanced engine and combustion technologies,” *International Journal of Engine Research*, vol. 13, no. 3, pp. 287–304, 2012.

[6] J. Hvezda, “Multi-Zone Models of Combustion and Heat Transfer Processes in SI Engines,” *SAE 2011-37-0024*, 2011.

[7] A. Iqbal, A. Selamet, R. Reese, and R. Vick, “Ignition Delay Correlation for Predicting Autoignition of a Toluene Reference Fuel Blend in Spark Ignition Engines,” *SAE 2011-01-0338*, 2011.

[8] B. Lawler, M. Hoffman, Z. Filipi, O. Guralp, and P. Najt, “Development of a Postprocessing Methodology for Studying Thermal Stratification in an HCCI Engine,” *Journal of Engineering for Gas Turbines and Power*, vol. 134, no. 10, p. 102801, 2012.

[9] S. Y. Ho and T.-W. Kuo, “A Hydrocarbon Autoignition Model for Knocking Combustion in SI Engines,” *SAE 971672*, 1997.

[10] T. Noda, K. Hasegawa, M. Kubo, and T. Itoh, “Development of a Transient Knock Prediction Technique by Using a Zero-Dimensional Knock Simulation with Chemical Kinetics,” *SAE 2004-01-0618*, 2004.

[11] S. B. Fiveland and D. N. Assanis, “DEVELOPMENT AND VALIDATION OF A QUASI-DIMENSIONAL MODEL FOR HCCI ENGINE PERFORMANCE AND EMISSIONS STUDIES UNDER TURBOCHARGED CONDITIONS,” *SAE 2002-01-1757*, 2002.

[12] N. P. Komninos, D. T. Hountalas, and D. A. Kouremenos, “Development of a New Multi-Zone Model for the Description of Physical Processes in HCCI Engines,” *SAE 2004-01-0562*, 2004.

[13] H. Curran, “A comprehensive modeling study of iso-octane oxidation,” *Combustion and Flame*, vol. 129, no. 3, pp. 253–280, 2002.

[14] Y. F. Tham, F. Bisetti, and J.-Y. Chen, “Development of a Highly Reduced Mechanism for Iso-Octane HCCI Combustion With Targeted Search Algorithm,” *Journal of Engineering for Gas Turbines and Power*, vol. 130, no. 4, pp.

042804–042807, 2008.

[15] T. Tsurushima, “A new skeletal PRF kinetic model for HCCI combustion,” *Proceedings of the Combustion Institute*, vol. 32, no. 2, pp. 2835–2841, 2009.

[16] M. P. Halstead, L. J. Kirsch, and C. P. Quinn, “The Autoignition of Hydrocarbon Fuels at High Temperatures and Pressures - Fitting a Mathematical Model,” *Combustion and Flame*, vol. 30, pp. 45–60, 1977.

[17] A. Babajimopoulos, P. Challa V S S, G. A. Lavoie, and D. N. Assanis, “MODEL-BASED ASSESSMENT OF TWO VARIABLE CAM TIMING STRATEGIES FOR HCCI ENGINES: RECOMPRESSION VS. REBREATHING,” presented at the ASME Internal Combustion Engine Division 2009 Spring Technical Conference, ICES2009-76103, 2009.

[18] A. Babajimopoulos, D. N. Assanis, D. L. Flowers, S. M. Aceves, and R. P. Hessel, “A fully coupled computational fluid dynamics and multi-zone model with detailed chemical kinetics for the simulation of premixed charge compression ignition engines,” *International Journal of Engine Research*, vol. 6, no. 5, pp. 497–512, 2006.

[19] R. J. Middleton, J. B. Martz, G. A. Lavoie, A. Babajimopoulos, and D. N. Assanis, “A computational study and correlation of premixed isooctane air laminar reaction fronts diluted with EGR,” *Combustion and Flame*, vol. 159, no. 10, pp. 3146–3157, 2012.

[20] J. Kodavasal, “EFFECT OF CHARGE PREPARATION STRATEGY ON HCCI COMBUSTION,” Ph. D. Thesis, University of Michigan, 2013.

[21] L. M. Olesky, J. B. Martz, G. A. Lavoie, J. Vavra, D. N. Assanis, and A. Babajimopoulos, “The effects of spark timing, unburned gas temperature, and negative valve overlap on the rates of stoichiometric spark assisted compression ignition combustion,” *Applied Energy*, vol. 105, pp. 407–417, 2013.

[22] R. J. Middleton, “SACI Flame Propagation Effects on Temperature-Mass Distribution,” presented at the HPLB Group Meeting - University of Michigan, 2013.

[23] J. L. Devore, *Probability and Statistics for Engineering and the Sciences*, 7 ed. Thomson Brooks/Cole, 2008.

[24] D. L. Stivender, “Development of a Fuel-Based Mass Emission Measurement Procedure,” *SAE 710604*, 1971.

[25] K. Chang, “MODELING AND ANALYSIS OF AN HCCI ENGINE DURING THERMAL TRANSIENTS USING A THERMODYNAMIC CYCLE SIMULATION WITH A COUPLED WALL THERMAL NETWORK,” Ph. D. Thesis, University of Michigan, 2010.

[26] A. Cairns and H. Blaxill, “The Effects of Combined Internal and External Exhaust Gas Recirculation on Gasoline Controlled Auto-Ignition,” *SAE 2005-01-0133*, 2005.

[27] A. Kulzer, J.-P. Hathout, C. Sauer, R. Karrelmeyer, W. Fischer, and A. Christ, “Multi-Mode Combustion Strategies with CAI for a GDI Engine,” *SAE 2007-01-0214*, 2007.

[28] L. Manofsky, J. Vavra, D. Assanis, and A. Babajimopoulos, “Bridging the Gap between HCCI and SI: Spark-Assisted Compression Ignition,” *SAE 2011-01-*

1179, 2011.

[29] J. E. Dec and Y. Yang, "Boosted HCCI for High Power without Engine Knock and with Ultra-Low NOx Emissions - using Conventional Gasoline," *SAE 2010-01-1086*, 2010.